2023-12-19

Understanding the Origin, Evolution, and Dynamics of Transneptunian Binaries

Benjamin C N Proudfoot

Brigham Young University

Understanding the Origin, Evolution, and Dynamics of Transneptunian Binaries

Benjamin C. N. Proudfoot

A dissertation submitted to the faculty of
Brigham Young University
in partial fulfillment of the requirements for the degree of

Doctor of Philosophy

Darin Ragozzine, Chair
Dennis Della Corte
Eric Hintz
Denise Stephens
Mark Transtrum

Department of Physics and Astronomy

Brigham Young University

ABSTRACT

Understanding the Origin, Evolution, and Dynamics of Transneptunian Binaries

Benjamin C. N. Proudfoot
Department of Physics and Astronomy, BYU
Doctor of Philosophy

This dissertation discusses research that focuses on understanding transneptunian objects (TNOs) using a variety of techniques and approaches. In Chapter 1, I introduce the main concepts used throughout this dissertation and discuss the current understanding of the transneptunian region. In Chapter 2, I discuss my efforts to understand how Neptune's late stages of migration affect the Haumea family, the only known collisional family in the transneptunian region. Using advanced simulations of Neptune migration, I find that the Haumea family can plausibly form before the termination of giant planet migration and show that this extensively mixes the family. The simplest explanation for the formation of Haumea and its family is a slow disruption of a large, primordial binary system. In Chapter 3, I examine the detectability of non-Keplerian effects in the mutual orbits of transneptunian binaries. I find non-Keplerian effects are common, with 20% of TNBs best explained by a non-Keplerian orbit. I also demonstrate that one of the components of TNB (66652) Borasisi-Pabu is a contact binary. In Chapter 4, I examine the non-Keplerian orbits of Hi'iaka and Namaka, the satellites of Haumea, showing that they are strongly affected by both inter-satellite gravitational interactions and precession caused by Haumea's nonspherical gravitational field. Future observations of the Haumea system, combined with non-Keplerian fitting, will sensitively probe Haumea's interior. Lastly, in Chapter 5, I explore the mutual orbits of Cold Classical TNO binaries using non-Keplerian orbit fitting. Out of a sample of 18 binaries, 6 have significantly non-Keplerian orbits, allowing detailed characterization of their system architecture. I find that 3 of these systems are best explained as hierarchical systems, while the remaining 3 are consistent with precession due to the Sun's gravitational influence. The hierarchical systems I find strongly support the streaming instability theory of planetesimal formation.

Keywords: Transneptunian objects, Binary Objects, Orbit Fitting, Dwarf Planets, Planet Formation

ACKNOWLEDGMENTS

List of Figures

List of Tables

Contents

Chapter 1

Introduction

The processes governing planet formation and evolution are extremely difficult to ascertain. Humans have observed the end products of planet formation since before written history, yet understanding planet formation is still an ongoing work. Great effort has been recently been made to observe planets–and their ongoing formation process–outside of our solar system, but observations and study of objects within our solar system can still provide deep insight into planet formation. As planet formation is a messy process, leftover planet-building material still resides within our solar system. Studying these leftovers, commonly called planetesimals, is a highly effective way to understand planet formation.

In this sense, planet formation is intimately connected with the physical characteristics of the icy bodies orbiting beyond Neptune–commonly known as transneptunian objects (TNOs). These bodies, and their physical characteristics, are still poorly understood as a whole. While *New Horizons*, has studied two examples in detail, the composition, shape, surface, density, and spin pole direction of thousands of known TNOs remain a mystery. For lone TNOs, these characteristics are extremely difficult to measure as current telescopes do not have the resolution to adequately resolve them. As a result, TNO characterization most often focuses on the most information-rich TNOs–those that are part of a binary system. A transneptunian binary (TNB) is a system of two gravitationally

bound TNOs. Understanding their mutual orbit permits characterization of mass, density, shape, and spin–all important physical characteristics which aid in understanding its formation. Through the study of TNBs, much can be learned about the formation and evolution of TNOs themselves, and consequently, planet formation in general.

1.1 TNB Mutual Orbits

Of the thousands of known TNOs, over 100 are known to be binary in nature. The known binaries can be divided into two separate categories: planet-moon binaries and near-equal binaries. With no exception, the largest known TNBs (in overall mass, size, brightness, etc.) are made up of one large object around which a much smaller moon orbits. Some TNOs have multiple moons, although here we still refer to these as TNBs. These systems are analogous to a planet and a moon, although Eris, the largest such TNB is still smaller than the Earth's Moon. On the other hand, near-equal binaries tend to be small. Possible formation mechanisms for each different type of TNB are discussed in Chapter 1.3. In addition to different system morphologies, the mutual orbits (i.e. the binary components orbits around each other) of the two types of TNBs are also quite distinct. The planet-moon TNBs tend to be on tighter, more circular orbits, than the near-equal TNBs, which tend to be on wider, and more eccentric orbits.

Determining the mutual orbit of a TNB is an extremely crucial step in characterization of the system. It allows a precise measurement of orbital parameters (semi-major axis, eccentricity, and inclination) and the orbit period. Knowledge of the orbital period, paired with the semi-major axis, can leverage Kepler's laws to determine the system mass. The mass, along with estimates of the sizes of the system components, further provides a measurement of the system's overall density. This is the first step in the characterization of a TNB system. But how is a TNB's mutual orbit established?
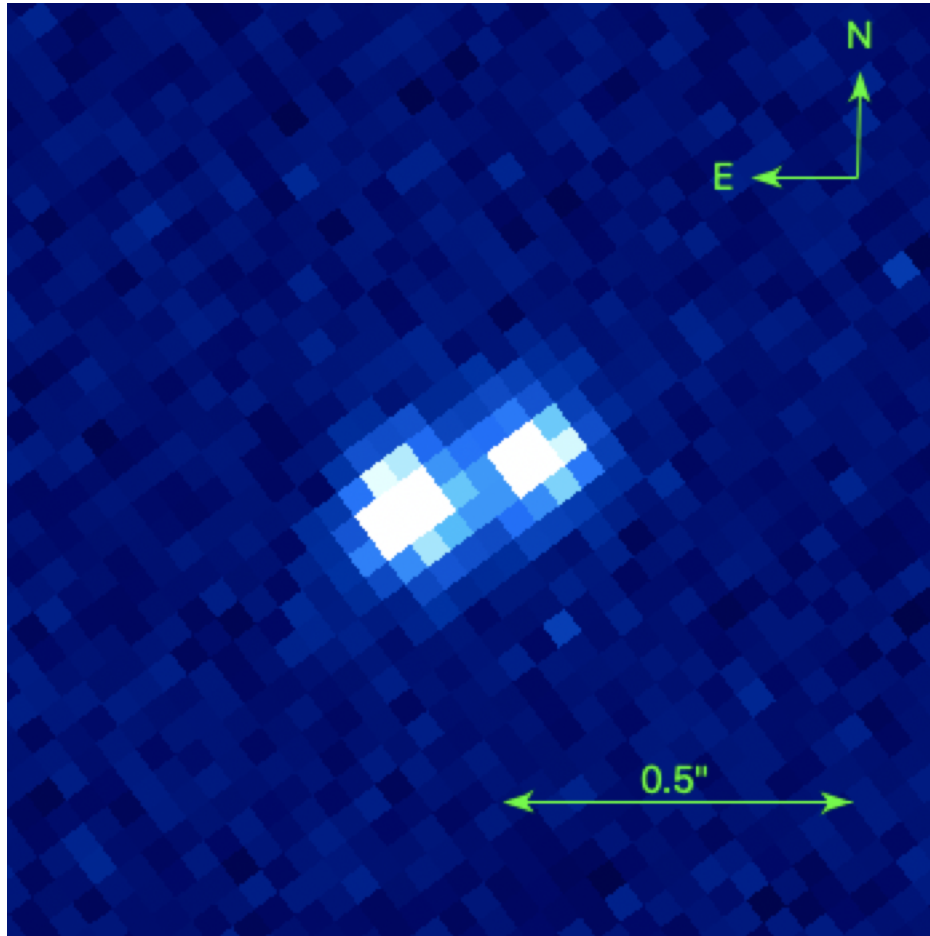
Figure 1.1 (148780) Altjira as seen by the Hubble Space Telescope on 2023-10-23. This image was acquired as part of my ongoing HST program (Program 17206).

Mutual orbit determination relies on high-resolution imaging of a TNB system across its entire orbital period. A typical observation of a TNB with the Hubble Space Telescope (HST) is shown in Figure 1.1. Images are precisely analyzed using point spread function (PSF) fitting techniques to extract the exact relative positions of each TNB component for use in orbit fitting. The relative positions of TNB components are usually referred to by the name 'relative astrometry,' or simply astrometry.

With the astrometry of the TNB components in hand, a simple Keplerian orbit model can be fit with a few simple inputs. The most important input is the position (i.e., distance and direction) of the TNB with respect to the Earth, often called the ephemeris. The ephemeris accounts for the motion of both the Earth and the TNB, which subtly change the angle at which the TNB is viewed. This allows a full 3-dimensional model of the TNB's motion to be created. Then, using a variety of model fitting techniques, the parameters of the orbit can be found, given the system's relative astrometry. A variety of smaller considerations need to be taken into account for the best possible accuracy. These include accounting for changes in light travel time between the observer and the TNB and correcting for aberrations in astrometry due to Earth's orbital motion. An example of a simple Keplerian orbit model fit to a series of relative astrometry measurements is shown in Figure 1.2. The figure shows the path of the orbit on the sky with relative astrometry overlaid.

Since the orbital period of a given TNB is not *a priori* known, careful scheduling of imaging is necessary to accomplish the task in as few observations as possible [1]. Typically for TNBs, a minimum of five high-resolution images (precision of $\lesssim$10 milliarcseconds) are required to fully determine a mutual orbit [1]. With random sampling in time, the number could be somewhat higher. Some orbit orientations introduce additional difficulties in orbit fitting, such as edge-on orbits where the two components are regularly close to each other on the sky. In this orientation, telescopes may not be able to resolve the individual components during every observation. Hence, these orbits require substantially more observations to determine the TNB's mutual orbit.

Another difficulty that arises in TNB mutual orbit fitting is an ambiguity in the orbit plane when observations are taken from too few aspect angles. The so-called 'mirror ambiguity' results in two acceptable orbit solutions (with similar period, semi-major axis, and eccentricities) that are mirror images of one another. Breaking the mirror ambiguity requires observations of the system at enough aspect angles to constrain the system geometry. Practically, this is achieved by acquiring observations well-separated in time.
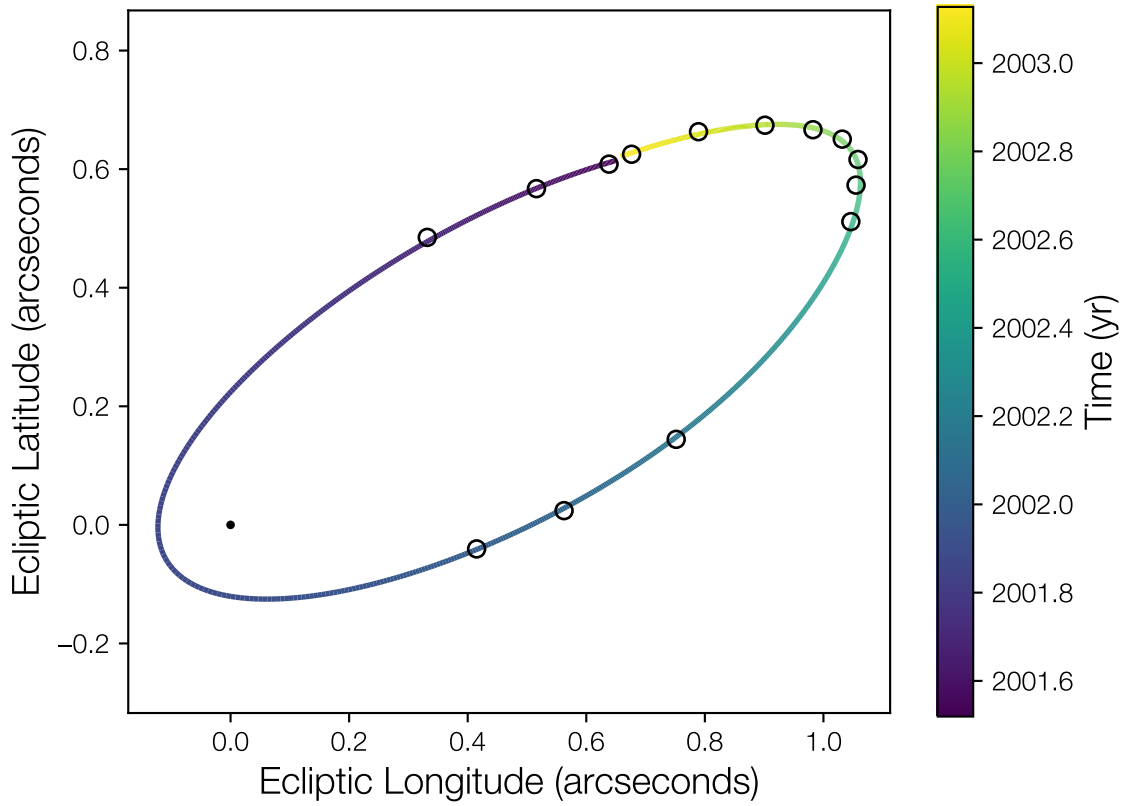
Figure 1.2 An orbit fit to relative astrometry acquired of TNB 1998 WW31. The solid line represents the orbit on the sky, over one mutual orbit period, where changing color indicates time. The circles represent the relative astrometry of the system taken between 2001-2003. Note the solid line does not reconnect with itself due to the changing viewing angle over time.

While the process outlined above uses a simple, well-justified model, it makes several assumptions. Firstly, it assumes the mutual orbit is not influenced by the gravitational pull of other sources (e.g. the Sun, passing TNOs, or additional system components). This is probably justifiable for most TNBs, but it is certainly not true for the widest TNBs [2]. Likewise, systems with multiplicity higher than 2 (like Haumea, Pluto, or Lempo) require additional consideration. Secondly, by using a Keplerian orbit, there is an implicit assumption that the components of the modeled TNB are spherical, or–more generally–that their shapes have no bearing on the mutual orbit. This may be important for many TNBs as most TNOs are known to be far from spheres (e.g., [3–5]). Relaxing these assumptions allow for the possibility of non-Keplerian orbital motion. Addressing these assumptions using a non-Keplerian orbit model is core to the work I present in this dissertation. Chapters 3-5 are fully dedicated to fitting TNB orbits with a more general orbital model which accounts for N-body dynamics and arbitrary shapes.

1.2 TNO Subpopulations

In addition to categorizing TNBs by their mutual orbits or physical properties, they can also be categorized by their heliocentric orbits. The transneptunian region can be broken down into roughly five subdivisions: cold classical Kuiper belt, the hot classical Kuiper belt, the Scattered Disk, Centaurs, and resonant populations. In Figure 1.3, we show these subpopulations in orbital element space.

The cold classical Kuiper belt (CCKB) is a population of TNOs on dynamically 'cold' orbits between 42 and 47 au. In this context, 'cold' refers to dynamical excitation where it implies orbits with low inclinations (with respect to the ecliptic plane). This population is thought to have been formed in situ and is relatively untouched since formation [6–8]. Compositional studies of the CCKB show that objects there are compositionally distinct from other TNO subpopulations [9–11].
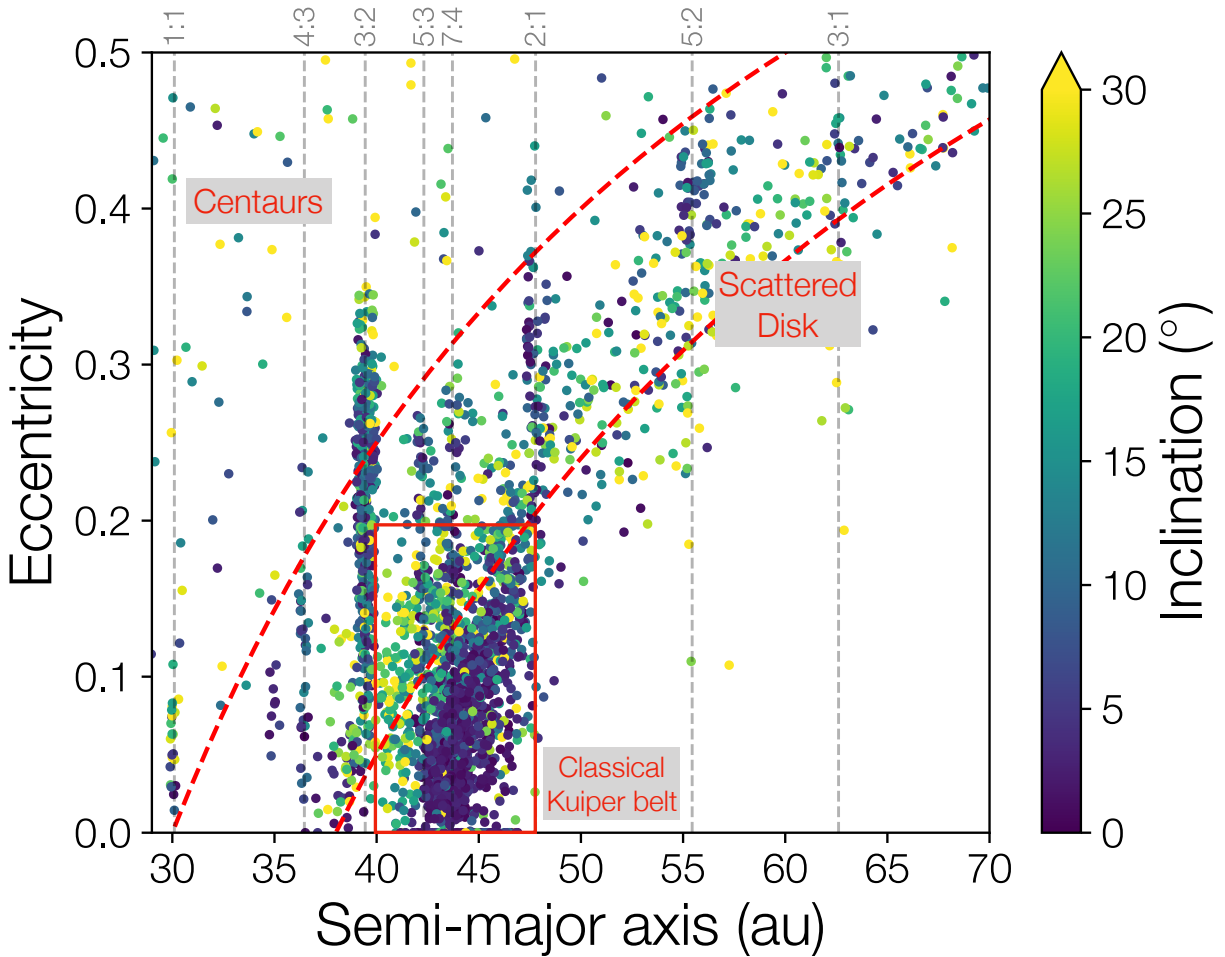
Figure 1.3 A schematic of the five different transneptunian populations. Gray vertical dashed lines show prominent orbital resonances, while the red dashed curves show lines of constant perihelion distances of 30 and 38 au. Between the red dashed lines is the scattered disk. The red rectangle roughly delineates the Classical Kuiper belt, which can be broken into the cold (low inclination) and hot (high inclination) components. Note that there is some overlap between subpopulations, especially the Hot Classical Kuiper belt and the Scattered Disk.

The CCKB is home to many binaries, with a binary fraction of $\sim30\%$ [12, 13]. All binaries in the CCKB are near-equal binaries [14], indicating that the processes that form planet-moon TNBs are not effective in the CCKB. This is likely due to the low overall density of TNOs in this population. The CCKB is the prime location to study planetesimals as they are virtually unaltered since their formation.

The hot classical Kuiper belt (HCKB) lies between 40 and 47 au and contains dynamically 'hot' objects (i.e., those with inclined orbits). Most studies agree that HCKB objects could not have been formed in situ, but instead were formed in a high density (relative to the CCKB) disk of gas, dust, and planestesimals interior to Neptune's current orbit [15, 16]. After the giant planets formed and began migrating, this disk was disrupted, scattering planetesimals to the HCKB [8, 17, 18]. This history is backed up by a variety of evidence including compositional studies, dynamical arguments, and the orbital structure of the hot classical region [9, 15, 19]. As the hot classicals were formed in a far denser environment–inside which collisional processes are effective–planet-moon TNBs are present in this population alongside near-equal TNBs [14]. The presence of both types of TNBs is likely due to either incomplete collisional processing, lack of collisional processing in different source populations, or contamination by the CCKB. The binary fraction in the HCKB is appreciably lower than the CCKB [12], presumably due to the violent scattering process that produced their current heliocentric orbits [20]. Although there is a low binary fraction, almost all of the largest TNOs found in this population are known to have small moons [21–25], hinting at common underlying planet formation processes.

The Scattered (or Scattering) Disk (SD) is a population of dynamically excited TNOs with perihelion distances between 30 and 38 au, enabling dynamical interactions between SD objects and Neptune. The SD is the largest subpopulation by mass and is home to many large TNOs (and TNBs). The origin of the SD is generally thought to be similar to the HCKB, with objects forming in the now-dispersed primordial disk [8, 26, 27]. In that sense, the SD can be thought of

as a high-eccentricity and high-semi-major axis tail of the classical Kuiper belt, extending out to well over 100 au. As with the HCKB, both planet-moon and near-equal TNBs are present in the SD. Due to the similarities between the SD and HCKB, they are often collectively referred to as the excited TNOs.

Centaurs are a population of objects with perihelia < 30 au, inside Neptune's orbit. Although many Centaurs actually orbit completely within Neptune's orbit, they are often regarded as a transneptunian subpopulation. Centaurs orbital dynamics are completed dominated by their interactions with the giant planets, and are thus quite unstable [28]. With dynamical lifetimes of only a few million years, the continued existence of Centaurs requires a source population from which Centaurs are created. It is generally believed that the SD is this source population, where slow dynamical erosion of the SD produces a population of Centaurs in a sort of quasi-equilibrium [8]. Binary centaurs are uncommon, with only three known [1, 14, 29]. The low binary fraction is due to frequent interactions with the giant planets which efficiently disrupts binaries [8].

Lastly, the resonant TNOs comprise all TNOs that reside in mean motion resonances (MMRs) with Neptune. MMRs, or simply just resonances, occur when the orbital periods of two orbiting bodies are a simple integer ratio of each other. MMRs often provide a stable location in which to orbit. For example, Pluto is in the 3:2 MMR with Neptune, with Neptune orbiting three times for every two Pluto orbits. This enables Pluto to remain stable, even though its orbit crosses Neptune's. Although not every MMR necessarily provides stability (see Figure 1.3), many Neptune MMRs are heavily populated with TNOs [30, 31], most prominently the 3:2 and 2:1 MMRs. The existence of TNOs trapped in MMRs is closely tied to the formation of the entire TNO population, and is especially dependent on the migration of Neptune during the early phases of the solar system (see Section 1.4 for further details). The population of Neptune's MMRs is also likely to be drawn from the primordial disk [30], and, like the HCKB and SD, is home to both types of TNBs, and most notably, Pluto.

1.3 TNO Formation Theory

Current study of TNO formation is centered on a formation model commonly called the Streaming Instability (SI) model. The SI model posits that gas drag felt by 'pebbles' in the protoplanetary disk cause clumping. Once enough mass clumps together, planetesimals can directly from by gravitational collapse [32–34], in a process very similar to star formation. This allows small TNOs to be formed directly from the small particles in the protoplanetary disk, bypassing various long-unsolved problems regarding traditional planetesimal forming processes. The size of planetesimals created by the SI can vary from small km-scale planetesimals up to ∼100 km planetesimals [35, 36].

While the SI model is theoretically useful, predictions from it also produce a compelling match to the TNO population. The SI model reproduces the size distribution of small TNOs without requiring any collisional evolution [37, 38], which other planetesimal formation models have failed to do. Another source of strong support for the SI model comes from the TNB population. When looking at the primordial, unaltered CCKB, the large fraction of binaries can be easily explained by the SI model, which is extremely efficient at creating near-equal binary systems [33, 34, 39]. Accounting for collisions and other disruptive events, some authors posit that almost all TNOs are born as binary systems via the SI [8, 40]. Additional evidence is drawn from the similar colors of individual TNB components [41], which cannot be explained by any other binary formation models. One of the strongest pieces of evidence for the SI model comes from analysis of TNB mutual orbits. The SI model predicts that TNB orbits will be predominantly prograde (i.e., the binary orbits in the same sense as its heliocentric orbit) [42], while other formation models significantly favor retrograde orbits [43–45]. Recent works analyzing TNB mutual orbits show that prograde orbits are overrepresented by 4:1, strongly favoring the SI model [42, 46].

A collapsing cloud of particles, triggered by the SI, is typically a low-velocity environment, which can lead to the production of close or contact binaries across a variety of size ranges [34, 39], especially when other dynamical effects are accounted for (e.g., gas drag, tidal interactions, Kozai

cycles, etc.) [47]. Surveys of TNO light curves have revealed that close/contact binaries are extremely common [48–52], lending further credibility to the SI model. In addition, images returned from the *New Horizons* flyby of Arrokoth, a member of the CCKB, show a pristine contact binary whose formation is consistent with the SI model [47, 53]. Likewise, the significantly flattened shapes of its two lobes could be a consequence of formation during gravitational collapse. Recent high-resolution simulations have also shown that unusual hierarchical triple systems (i.e., a tight binary system orbited by a more distant third component) are unique outcomes of gravitational collapse triggered by the SI [34]. In Chapters 3 and 5, I revisit some of these findings and find that the shapes/morphologies of TNBs also strongly point towards formation in the SI paradigm.

While TNO/TNB formation by the SI model is crucial for understanding the smaller TNOs/TNBs, to produce larger TNOs, additional processes are required [8, 35, 36]. Large TNOs ($\gtrsim$100 km) presumably form similar to small TNOs, after which the process of collisional coagulation proceeds [8, 54, 55]. Collisional coagulation is the process by which pairwise collisions create continually larger planetesimals. Once large enough (300-400 km), planetesimals can then begin to efficiently accrete loose, individual pebbles from the protoplanetary disk in a process known as pebble accretion [56]. Pebble accretion is the final stage of formation for TNOs, which have a maximum radius of ∼1000 km.

The formation of planet-moon TNBs is naturally explained as part of the collisional coagulation process. As in the case for the Earth-Moon system [57], it is widely believed that TNO moons form in the aftermath of large collisions [21, 58–60]. Since moons are extremely common around the largest TNOs (8 of largest 10 have moons), moon-forming collisions must have been common [21–25, 61–65]. Despite the consensus on their necessity, efforts to model these planetary-scale collisions have been few and far between. The required smoothed particle hydrodynamics (SPH) simulations are extremely computationally expensive. In addition, the parameter space to be explored is vast. Collisions strongly depend on impact velocity, impact parameter, target and impactor size,

composition, temperature, equation of state, initial rotation, and many more parameters. As such, only a few TNOs have been modeled in any detail [66–69]. Recent effort has moved towards general simulations from which broad implications can be drawn [60]. For example, a recent study has shown that many TNO moons could actually be remnants of the impactors themselves [60]. Unfortunately, many mysteries remain in explaining planet-moon TNBs. In the future, more SPH modeling of TNO formation is required to fully understand the production of planet-moon TNBs across the range of TNOs.

Another strong indicator of the importance of collisions in TNO formation is the existence of the Haumea family [70–72]. Haumea is the third largest TNO [4], has two impact-generated moons [21, 73], and is the largest remnant of the Haumea collisional family. A collisional family is a group of objects clustered in orbital element space that are likely to have originated in a collision. The Haumea family is tightly clustered, and each family member shows an extremely unique water-ice feature in its near-infrared reflectance spectrum. Haumea, its moons, and its family probably formed in a giant collision near the end of Neptune's migration [74]. Understanding its family and moons are studied in detail in Chapters 2 and 4.

1.4   Neptune Migration

Evidence strongly points towards the fact that the solar system's planets did not form where they currently reside [26, 27, 75–78]. While details and timings are vigorously debated, broad consensus has formed around the idea of planet migration. That is, after formation, planets migrate to their current locations, driven by gravitational interactions with other planets [26], disks of planetesimals [79], or the gas present in the protoplanetary disk [80]. Most notably for the study of TNOs, Neptune is believed to have migrated after its formation, driven outwards by the primordial

disk of leftover planetesimals [27]. This episode of migration is the defining process that sculpted the transneptunian region.

As Neptune migrated into the primordial disk, it scattered the planetesimals contained within it, which went on to form the excited TNO populations (SD and HCKB) [17]. In addition to scattering, Neptune was also able to trap TNOs into its MMRs as it slowly moved outwards [75, 81]. Determining the overall distance migrated and the time it took has been the focus of many studies over the past decade (for a review, see [8, 27]). Although specifics are still uncertain, it has become clear that the migration must have been long-range and taken place slowly ($\sim$10s of Myr) [19]. Studies have also revealed that the migration was grainy (i.e., characterized by many discrete jumps), indicating that the planetesimals scattered were Pluto-sized. The primordial disk that was scattered was likely composed of $\sim$1000s of Pluto-sized objects, with a total mass of 15-20 $M_{\oplus}$ [82]. Compared to the current mass contained within the entire transneptunian region, this implies a survival rate of $\sim 10^{-3}$, meaning that the TNOs we see today are 0.1% of the original primordial disk. Simulations of the migration process have been key to understanding the primordial solar system, giving insight into compositional gradients in the primordial disk [83], the population of binaries prior to scattering [20], and even the existence of planets that were ejected early in the solar system [84, 85].

For this dissertation, Neptune migration is discussed, in the context of the Haumea family, in Chapter 2.

1.5   Dissertation Summary

This dissertation is primarily composed of four separate chapters, each detailing a single project. The first three body chapters (Chapters 2-4) are made of fully completed articles in various stages of publication. As such, the chapters are in journal specific format and style. The final chapter

(Chapter 5) details work which will eventually be published pending the observations from an ongoing Hubble Space Telescope program. As such, the chapter is written in the normal format of a dissertation chapter.

Chapter 2 focuses on how the Haumea family could have been formed, when placed in the context of Neptune migration. Understanding the Haumea family is an ideal way to probe how collisions work in the outer solar system. I find that the Haumea family can best be explained as a collision between the two components of a destabilized TNB. This would be most likely to happen in the aftermath of the proto-Haumea's scattering by Neptune as it migrates outwards. Neptune migration subsequently mixes the family, only slightly eroding it, and produces the strongly dynamically sculpted family we see today. This work emphasizes the importance of dynamical context when studying the creation of collisional families. It also motivates future work on understanding collisions, as they pertain to large TNBs.

Chapter 3 describes a study on the possible detectability of non-Keplerian orbital motion in TNB mutual orbits. Understanding if non-Keplerian motion is prevalent in TNB both validates (or challenges) the assumptions of past work, and it opens a new path towards learning more about the shapes of TNB components. I find that a significant fraction of TNBs have detectable non-Keplerian motion ($\sim$20%), however, I show that, even when non-Keplerian motion is detectable, the assumptions made in past work are justifiable. This further solidifies TNB analysis as a method for understanding planetesimal formation. The survey completed in this work lays the groundwork for a series of future studies that can reveal the shapes of TNB components. Just as the shape of Arrokoth provided evidence for the SI model of planetesimal formation [47], future studies predicated on this work will continue to aid our understanding of planet formation processes.

Chapter 4 revisits the Haumea system and is dedicated to understanding the orbits of Haumea's moons. Its goal is to measure Haumea's nonspherical gravitational field using the moons as 'probes'. This measurement is able to remotely examine Haumea's interior, possibly constraining

the size/density of Haumea's core. Planetary core formation (or differentiation) is a crucial aspect of planet formation, which is completely unconstrained for TNOs. Differentiation is intimately linked with a variety of formation processes (e.g., collisions, inclusion of radioactive isotopes, chemical alteration of minerals, etc.). Unfortunately, despite new data and a suitably complex model, I show that current data is not enough to accomplish the stated goal. Although disappointing, the analysis is still useful for exploring the dynamics of the Haumea system. Given more data, future analysis using the same methods will be able to fully characterize Haumea's gravitational field and place strong constraints on Haumea's formation history.

Lastly, Chapter 5 contains an in-depth, non-Keplerian analysis of CCKB binary (CCKBB) mutual orbits in an effort to provide evidence for (or against) the SI model of planetesimal formation. I find that 6 CCKBBs show compelling evidence of non-Keplerian motion. Of these, three are consistent with hierarchical systems. As the SI model strongly favors the production of hierarchical systems, this discovery lends credibility to the SI model. In addition to characterizing several systems, I also find that upper limits can be placed on the non-Keplerian nature of a large fraction of other CCKBB components. I lastly describe an ongoing HST program aimed at characterizing CCKBBs further, which should produce more evidence of CCKBB formation via the SI.

Chapter 2

The Formation of Haumea and its Family via Binary Merging

The content of this chapter has been published in Nature Communications. I reproduce the journal Version of Record here in accordance with the article's Creative Commons CC BY license and Springer Nature's author reuse standards. The full citation and link to the article are shown below.

Proudfoot, B., Ragozzine, D. The formation of Haumea and its family via binary merging. Nat Commun 13, 2262 (2022). https://doi.org/10.1038/s41467-022-29901-5

ARTICLE

OPEN

Check for updates
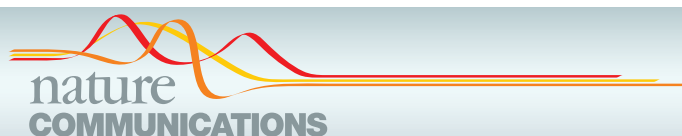
The formation of Haumea and its family via binary merging

Benjamin Proudfoot [1] & Darin Ragozzine [1]

Dozens of families of asteroids in the asteroid belt have similar orbits and compositions because they formed through a collision. However, the icy debris beyond the orbit of Neptune, called the Kuiper Belt, contains only one known family, the Haumea family. So far, no self-consistent explanation for the formation of the Haumea family can match all geophysical and orbital characteristics of the family without invoking extremely improbable events. Here, we show that the family is adequately explained as the product of a merging binary near the end of Neptune's orbital migration. The unique orbital signature of a merging binary, which was not found in extensive searches, is effectively erased during the final stages of migration, providing an explanation for all aspects of the Haumea family. By placing the formation of the Haumea family in the broader context of solar system formation, we demonstrate a proof-of-concept model for the formation of Haumea.

[1] Department of Physics and Astronomy, Brigham Young University, N283 ESC, Provo, UT 84602, USA. ✉email: benp175@gmail.com

ARTICLE

Studies of the asteroid belt reveal that asteroid families are most commonly the result of catastrophic collisions between two bodies. In catastrophic collisions, the target is gravitationally disrupted, ejecting collisional family members outwards at velocities large compared to the escape velocity of the asteroid, but small compared to their heliocentric orbital velocity. Despite collisional families being common among the asteroids, only one family is known in the Kuiper belt. The Haumea family, first discovered in 2007[1], was originally hypothesized to be the product of a catastrophic collision, much like the known asteroid families. However, a catastrophic collision like those that form asteroid families cannot be supported by the observations of Haumea for three reasons. First and foremost, the distribution (in semi-major axis, inclination, and eccentricity [*a-e-i*] space) of family member orbits is ~20 times too small[2,3]. Typical catastrophic collisions impart a change in velocity, $\Delta \mathbf{v}$, of a few times the escape velocity of the largest remnant, in the case of Haumea, a $\Delta \mathbf{v}$ of ~2000 m s^{-1} [3,4]. The family's current velocity distribution is ~100 m s^{-1} [3,5]. Indeed, for collisions large enough to have debris detectable by current surveys of the Kuiper belt, the spread in proper orbital elements should be comparable to the whole Kuiper belt[6]. Second, the size distribution of Haumea family members is very shallow, with most of the mass concentrated in the largest objects, inconsistent with any kind of catastrophic disruption event[3,7]. Third, these size distributions allow us to estimate that the original mass of the family is a few percent of the mass of Haumea[7], in contrast to tens of percent ejected in a typical catastrophic asteroid collision[4]. Various hypotheses for the formation of the Haumea family have been proposed to explain the small spread in orbital elements[8–11], but all hypotheses that rely on a catastrophic collision are inconsistent with the data[7]. Indeed, even the destruction of an object with the total mass of the known family members (not including Haumea) would already produce a spread in orbits well beyond what is currently seen.

One of the most promising non-catastrophic formation mechanisms is the graze-and-merge collision proposed by Leinhardt et al.[9]. In this mechanism, two large (~650 km) objects suffer a grazing collision at low velocity creating a rapidly spinning body which then sheds mass due to excess angular momentum, forming both the Haumea family and Haumea's two satellites. This mechanism readily creates a compact low-mass family, made primarily from the water ice mantle of already differentiated impactors. The creation of nearly pure water ice family members, consistent with their spectra[12,13] and albedos[14,15], is a strong geophysical constraint on family-formation hypotheses that is well-matched by graze-and-merge style impacts. In this scenario, as family members are ejected due to an excess of angular momentum, their ejection vectors will lie along a tight plane. The previous work[3] showed that this type of ejection does indeed have a detectably unique correlation in *a-e-i* space, but ruled out a planar ejection at the ~2.5-σ level. Additionally, a slow graze-and-merge collision between two independent large bodies in the excited part of the Kuiper Belt suffers from an extremely low probability[16].

The low probability of an independent collision can be circumvented, if Haumea was originally a binary, probably near-equal mass with each body with a radius of ~650 km, where the components eventually collide in a graze-and-merge style collision, as originally suggested by Marcus et al.[6] Kozai cycles, a dynamical effect that allows a binary to exchange angular momentum between the binary eccentricity and inclination, combined with tidal friction[17,18] (Kozai cycles with tidal friction (KCTF)) is a natural mechanism for explaining this collision although other mechanisms are possible[19], such as encounters with Neptune, geophysical evolution[20], and others.

While the probability of having a near-equal (mass ratio >~10%) binary with a total mass near that of Haumea is not well studied, we view it as plausible, based on formation models and comparisons to other large objects. Formation models[21] show that large ~equal-mass binaries are capable of forming from the gravitational collapse of pebble clouds, though the proto-Haumea binary would occupy the upper mass range of these models. Other models show that a near-equal mass binary could survive implantation into the dynamically excited population of the Kuiper belt[22]. Comparison with other objects provides another indication that large binaries are plausible. Triton, currently a moon of Neptune, is hypothesized to have been a large near-equal binary from the same parent population as the Kuiper belt[23]. The Pluto–Charon system is ~4 times larger than the proposed proto-Haumea binary, with a mass ratio that is amenable to a graze-and-merge type collision formation. It has recently been proposed that the Pluto–Charon system was formed in a similar manner, where the destabilization of a binary system allows for a far higher collision probability[19]. Despite the indications that a near-equal binary proto-Haumea is plausible, the occurrence of large, near-equal mass binaries should be explored further.

With the probability of the graze-and-merge collision thus addressed, we turn to the question of why the observed Haumea family does not exhibit the expected *a-e-i* correlation from planar ejecta. The previous work[3] showed that this planar ejecta distribution would survive dynamical interactions for 4.5 GYr and is inconsistent with the observed family at the 2.5-σ level. However, these dynamical interactions assumed the planets were in their current orbits and did not place the Haumea family in the context of solar system formation which includes a long (~100 MYr) final stage of Neptune migration. Previous studies speculated that any Neptune migration would likely destroy the tight clustering of family members[3,11]. This led to the supposition that Haumea must have formed after Neptune's migration was completely over, even though age estimates can only say that the Haumea family is >~1 GYr old.

In this work, we show that this assumption is not supported by using migration simulations that show that the compact nature of the Haumea family can be maintained during the late stages of Neptune migration proposed by other investigations. Our simulations additionally reveal that during Neptune migration, the orbital distribution of family members is mixed so that an originally planar family can appear very similar to the family seen today. With this fact in mind, we propose that the proto-Haumea formed as a near-equal binary in the primordial trans-Neptunian belt. Following the standard formation model for the dynamically excited Kuiper Belt[24], the proto-Haumea was first scattered onto a dynamically unstable orbit, captured into one of Neptune's mean motion resonances (MMRs), and subsequently dropped out of resonance near its current orbit. The strong processes in this dynamical excitation and depletion event are too chaotic to expect that the Haumea family formed in the primordial trans-Neptunian belt and was then placed into its observed tight cluster. While we do not specifically propose the MMR from which Haumea was dropped out of, there are several low-order MMRs that could have placed Haumea in its current position (e.g., 3:1, 5:2, 9:4, etc.). The large change in Haumea's heliocentric inclination during this process could have naturally initiated Kozai cycles. KCTF leads to a merger of the proto-Haumea binary; this can take thousands to millions of years depending on the conditions[18,25]. The graze-and-merge collision puts too much angular momentum into the proto-Haumea, which sheds a small amount of mass in the form of icy bodies from its tips. This explains Haumea's near-critical rotation rate, two near-coplanar moons, the small mass of the family, its shallow size distribution, and the low ejection velocities required to form a compact family,

                                                ARTICLE
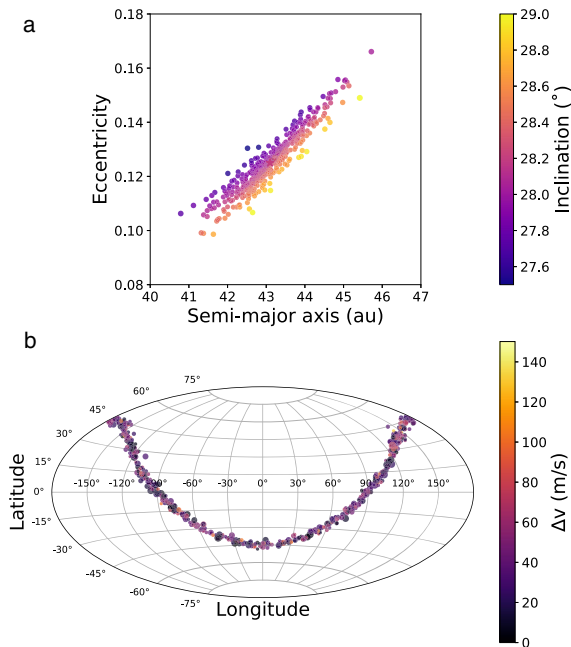
Fig. 1 A synthetic planar family. A realization of a graze-and-merge (planar) Haumea family. In panel **a**, the family is shown in *a-e-i* space. The family shape and distribution are typical for a graze-and-merge collision, with the planar distribution of family members visible as a distinct correlation between semi-major axis, eccentricity, and inclination. In panel **b**, the ejection direction of each family member is shown in ecliptic latitude and longitude. Here the size of each family member corresponds to the size of the point. This demonstrates that the family members are ejected in a planar manner, with a typical planar dispersion of ~2°, consistent with the properties of a graze-and-merge family. Source data for this figure are provided as a Source data file.

as have been shown in other studies[3,7,9]. The final part of Neptune migration, especially a jump of eccentricity like that already proposed[26,27], then mixes the objects into the presently observed orbital configuration.

Results

In the framework of our proposed model, the family originally contains a planar ejection with strong correlations in the *a-e-i* distribution of family members (see Fig. 1). Whether by KCTF or another means, destabilization of this proto-binary is most likely to happen soon after Haumea reaches the hot classical belt. During this time, Neptune is still completing its final stages of migration, which has not been accounted for in previous models. Our results show that as long as Neptune gets a modest (~0.05–0.1) eccentricity kick after the formation of the Haumea family, the planar distribution is mixed sufficiently to be similar to the presently-observed Haumea family. Modern migration models developed independently to explain other features of the Kuiper belt have such eccentricity kicks and these same models mix the Haumea family enough to produce the uncorrelated *a-e-i* distribution that is observed while maintaining its compact size. The minimal influence of the tail-end of Neptune migration on the compact nature of the Haumea family allows far more flexibility in explaining the family forming collision. The timeframe for this proposed Haumea family formation is potentially quite long based on current models of the formation of the trans-

Neptunian belt, which we adopt without modification in our proposed model.

Numerical integrations. Using the n-body integrator REBOUND[28], we have performed a suite of integrations recreating some models of Neptune migration found in the literature. Crucially, many of these models[26,29,30] show Neptune having an instability where the orbital elements can abruptly change in short amounts of time. These abrupt changes, often called jumps, can be modeled via instantaneous changes in the orbital elements of Neptune. In our integrations, we test whether jumps in semi-major axis and eccentricity can enhance mixing.

In each of these integrations, a prototypical planar family was integrated along with the outer planets while Neptune migrated outwards. The initial state of the family is shown in Fig. 1. Upon qualitative analysis of our integrations, it is clear that mixing of the family does indeed occur without excessive erosion. Figure 1 shows the initial state of the family, immediately after creation and when compared to Fig. 2, it is clear that the diffusion of family members is extensive.

Mixing mechanisms. While it is clear that our integrations demonstrate the feasibility of mixing due to Neptune migration, it is not immediately clear why the family members are mixed so efficiently. To find the specific mixing mechanisms, we performed some additional integrations to determine the exact mixing mechanisms (see "Methods" subsection "Numerical integrations").

The most intuitive mechanism for mixing before the jump in orbital elements is the transport of the semi-major axes of family members within mean-motion resonances (MMRs). Objects that are captured in MMRs during Neptune's migration are pushed to higher semi-major axes. At the same time, these captured family members typically diffuse to higher eccentricity and lower inclination, as has been seen in many previous analyses. When our final integrations are compared with the exploratory integrations, it is clear that resonant capture, transport, and subsequent removal from MMRs are not responsible for the bulk of the mixing.

The majority of mixing in our simulations occurs after Neptune's jump, which causes a period of enhanced mixing. While not immediately clear whether the jump in semi-major axis or eccentricity is responsible, our exploratory integrations definitively showed that the jump in eccentricity is the dominant factor. Dynamically, the increased eccentricity of Neptune has strong effects on both the strength and size of resonances. Higher-order resonances of the form $p + q$:p, several of which are located near the Haumea family, are composed of q subresonances with strengths proportional to $e_N{}^j e^k$ where $j + k = q$. Prior to Neptune's jump, its eccentricity is small and only the $k = q$ subresonance is active for family members near MMRs. Increasing Neptune's eccentricity activates the other subresonances, enhancing chaotic diffusion, leading to the period of mixing after a jump in Neptune's eccentricity.

Combined with the numerical integrations discussed here, our exploratory integrations showed that smooth migration at low eccentricity is probably not sufficient to mix a planar family. Despite this, we expect that many types of Neptune migration models could be capable of mixing a planar family, including ones where Neptune doesn't experience any jumps. Some of our preliminary integrations had Neptune cross a MMR with another planet, temporarily increasing its eccentricity, and subsequently efficiently mixing a planar family. Alternatively, a hard dynamical instability[30] may have a tail end where Neptune's eccentricity is sufficiently elevated to mix a family that forms while Neptune's eccentricity is still non-zero. Despite the wide variety of models,

ARTICLE   NATURE COMMUNICATIONS | https://doi.org/10.1038/s41467-022-29901-5
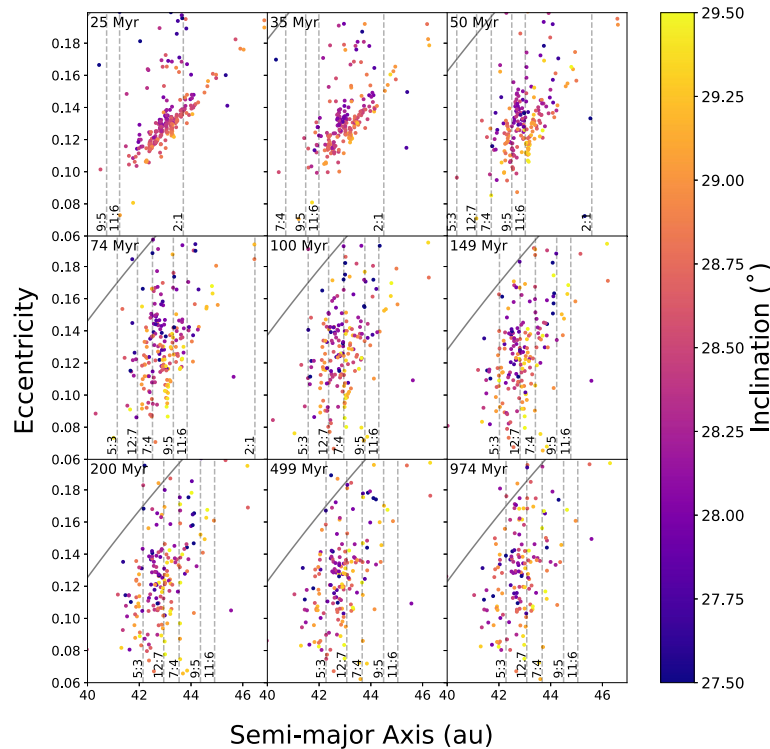
Fig. 2 Mixing of family members during migration. The averaged orbital elements throughout our integration. The orbital elements are found using a 50 Myr centered moving average of the instantaneous orbital elements of each object; this corresponds roughly to proper elements for non-resonant objects, though technically proper elements are not well-defined for migrating planets. Each panel is labeled with the time in the top left, with Neptune's jump occurring at 35 Myr. Note that the color bar deviates slightly from Fig. 1. In each frame, dashed, gray lines show the instantaneous locations of some of Neptune's mean-motion resonances (MMRs). The diagonal, solid black line is an estimate of where scattering with Neptune becomes strong enough to remove objects (7/6 a_N, corresponding to 35 au with $a_N = 30$ au). For a comparison to the family without migration, see Fig. 1. In the first panel, objects which have been captured into the 2:1 MMR are clearly migrating to higher eccentricities and lower inclinations (darker colors). In the second panel, at the time of the jump, the objects which were previously inside the 2:1 MMR have now been dropped out of resonance. Additional resonances passing through the family create chaotic diffusion in eccentricity over the next several panels, removing some of the *a-e-i* correlation and changing the tilted elliptical shapee5. Throughout this process, objects near resonances sometimes have their eccentricity excited, moving them into the unstable region where scattering becomes dominant. By the end of the integration, the original *a-e-i* correlation present in the planar family has been substantially obscured. Source data for this figure are provided as a Source data file.

many have periods of increased e_N which is thought to be an essential component of successfully reproducing features in the Kuiper belt[31]. Thus we believe that the results presented here could be reproduced with different migration scenarios, though we hope that future observations of Haumea family members will be able to place specific constraints on outer solar system formation models.

Quantitative assessment of the mixing. In addition to qualitative assessment, the mixing efficiency was also evaluated using the state-of-the-art Bayesian fitting routine outlined in Proudfoot and Ragozzine[3]. This fitting routine takes an observed family and determines posterior distributions for the properties (location, extent, angular dispersion, etc.) of a model family designed to match a variety of formation hypotheses, without any dynamical evolution. While these fits produce posterior distributions for over a dozen parameters, we focus on the angular dispersion parameter κ as a measurement of the planar-ness of the family. When $\kappa > 250$, the family has an angular dispersion <5°, which we call planar. We find that only ~3.5% of the resulting posterior distribution was consistent with a planar ejection, while the vast majority of the posterior was consistent with an isotropic (non-

planar) ejection. The rejection of a planar ejection at a ~2-σ level and the distinct shape of the posterior distribution are both extremely similar to results found in previous work based on the present-day observed family[3]. In Fig. 3, we compare these distributions. In Fig. 3, all the posterior distributions show a large peak at $\kappa \sim 10$. This has been previously explained as a result of overfitting, but may indicate that the model is trying to reproduce the boxy shape of the family produced by Neptune migration.

Erosion and expansion of the family. We measured the extent of the erosion and expansion of the family after being subjected to Neptune's migration. We found that 35–40% of family members are removed by Neptune's effects. Given the current estimates for the mass of the family (~3% of Haumea's mass[7]), we estimate that the mass of the Haumea family was initially ~5% of Haumea's mass. This is in closer agreement with smoothed particle hydrodynamic models which estimated a family mass of ~7% of Haumea's mass, given a graze-and-merge formation[9]. We do note, however, that the real-world strengths of each MMR passage are likely underestimated, and the number provided here is likely a lower bound on the mass removed.

ARTICLE
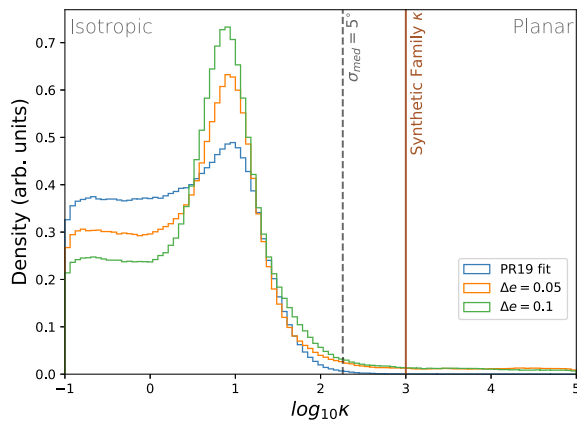
Fig. 3 Comparing our integrations to the true family. A comparison between the posterior probability distribution of κ—the planar concentration parameter—of our two integrations (in orange and green) and the κ distribution from PR19 found for the true family (in blue). Marked with a gray dashed line is the value of κ above which a synthetic family could be explained by a graze-and-merge collision ($\sigma \lesssim 5°$). We also mark in brown the value of κ which the planar family was created with. Only ~3.5% of the posterior distribution of our integrations is consistent with a graze-and-merge formation, similar to the 1% found for the actually observed Haumea family. All three posteriors display a large peak near $\kappa = 10$, which is attributable to overfitting. This demonstrates that Neptune migration can mix a graze-and-merge family into an *a-e-i* distribution similar to the observations, though we emphasize that it is not equivalent to fitting the proposed model to the observational data. Source data for this figure are provided as a Source data file.

Despite the removal of much of the family, the family does not expand a great deal. We find that the median $\Delta\mathbf{v}$ of family members is approximately doubled, but most family members retain a $\Delta\mathbf{v} < 150\ \mathrm{m\,s}^{-1}$, as is observed in the current family (see "Methods" subsection "$\Delta\mathbf{v}$ comparisons"). This is partly due to the Haumea family's proximity to orbits that are long-term unstable due to Neptune interactions.

Discussion
A variety of observational constraints suggest a graze-and-merge collision origin for the Haumea family: very small ejection velocities, Haumea's unusually rapid rotation, and the extreme water ice spectra of family members. Previous works' primary objection to the graze-and-merge collision was its ~2.5-σ inconsistency with the observed *a-e-i* distribution of family members[3] (and all other hypotheses were also rejected). By adding the expected mixing due to Neptune migration, we have shown that the expected shape of the family is consistent with the observations, turning this weakness into a strength. As a result, the graze-and-merge formation hypothesis, augmented with a collision of a proto-binary, satisfactorily matches all the observational constraints without invoking improbable events, unlike previously proposed hypotheses. In addition, our integrations clearly show that the Haumea family, after formation near its current location, can survive some forms of Neptune migration. This opens up the possibility that family formation mechanisms besides our proposed mechanism could conceivably match the known constraints on the Haumea family. In the future, the loosened constraints on the timing of the family formation should be incorporated into proposed mechanisms.

Family models without Neptune migration already suffered from the small number of known Haumea family members. Attempting to match post-migration models to the observed family would have been computationally challenging and underconstrained. However, as the Vera C. Rubin Observatory's Legacy Survey of Space and Time (LSST) is expected to discover and characterize ~80 new Haumea family members within the first ~2 years of the survey, future analyses could potentially identify properties of the original ejection of family members. For example, future work could identify a subset of family members relatively unaffected by Neptune migration that retain the original planar ejection characteristics.

At present, our results do not provide strong evidence for one migration scheme over another. In testing, we found that several different schemes worked well to mix the family, including a jumping Neptune with moderate eccentricity jumps, a four-planet model with a period of excited eccentricities due to resonances between the outer planets, and increased eccentricity with Neptune at its current location. Our integrations are not all appropriate for the actual solar system but are varied enough to show that mixing is not an unusual outcome. With more known family members and detailed modeling, the shape and size of the Haumea family may provide valuable constraints on models of Neptune migration.

Future work should also explore the details of various components of this hypothesis such as the frequency of proto-binaries large enough to explain Haumea; geophysical evolution of the interiors of proto-Haumea binary components and Haumea itself; formation of Haumea's moons from ejected debris; expected family ejection directions generated by binary collision (possibly caused by KCTF); relative chronology of Haumea's formation within the phases of Neptune migration; new hydrodynamics simulations of relevant graze-and-merge collisions; and comparisons to other mantle-stripping collisions. For example, a differentiated proto-Haumea should have had a crust of other volatiles, which crust appears to be missing from present family members. Can hydrodynamical models explain what happened to this crust? Was it volatilized and thus absent never formed into solid family members? Are these crust pieces much darker and thus simply harder to find in present surveys?

Despite our simple integrations, which neglected to model some of the complexities involved in the phase of giant planet migration, our integrations show, as a proof-of-concept, that compact families can persist throughout the final migration of Neptune. Further works should explore the survivability/mixing efficiency when more realistic conditions are added. Some of these could include simultaneous migration of the other planets (Jupiter, Saturn, and Uranus), effects of an inclination jump during the dynamical instability, differing migration timescales, differing eccentricity damping timescales, and others.

Another important effect that was not taken into account was the collisional evolution of the family after formation, both from family member–family member and family member–interloper collisions. However, given the shallow size distribution of the family[3,7], there is no evidence for significant collisional grinding after the creation and mixing of the family. This may be due to the lack of major collisions (which are quite improbable) or the low observability of sub-families. Even if evidence for collisional grinding was present, we believe that it would likely only enhance the effective mixing. Each collision would create more (sub-) family members with a spread in *a-e-i* space, enhancing the mixing of particles when taken as a whole, although it may lead to an even more mass-depleted family. One interesting avenue of research would be to look for sub-families (or pairs) among the members of the Haumea family to find evidence of any putative collisional evolution.

ARTICLE

While the majority of the confirmed family lies within ~150 m s^{-1}, there are two spectrally confirmed family members which lie further from the family, 1999 OY$_3$ and 2003 SQ$_{317}$ in addition to Haumea itself. The previous work[5] showed that these objects could diffuse in nearby MMRs, thereby reducing their **Δv** to be well within the family. However, more accurate orbit determinations, alongside new dynamical integrations, show that only Haumea is presently affected by MMRs: 1999 OY$_3$ is 0.6% wide of the 7:4 and 2003 SQ$_{317}$ is 1.2% wide of the 5:3. While unexpected in previous hypotheses, these two objects can be easily explained in the framework of our integrations. In both of our integrations, at the time of the dynamical instability, many family members begin diffusing chaotically in eccentricity. This chaotic diffusion lasts for a short time while Neptune's eccentricity is still excited. Once the period of diffusion ends, the eccentricity distribution of the family has broadened significantly, leaving a fuzzy edge to the family at high eccentricities, especially near present-day MMRs. The bulk of the synthetic family members remains between about $e = 0.1$–0.145, while the edges of the e-distribution extend to $e = 0.08$ and 0.18. This naturally explains the distribution of confirmed family members, which has a similar morphology. Identifying larger numbers of family members should reveal this fuzzy edge which may help to confirm/constrain the formation mechanism we have proposed.

In the broader context of family finding in the Kuiper belt, our results may hold a clue as to why other large Kuiper belt families have yet to be identified. In our integrations, we find that 35–40% of family members are removed from the family; most of these removed family members are eventually ejected from the solar system, helping to keep the compositional signature of Haumea family members confined to one region in *a-e-i* space. This confinement is due to the Haumea family's (otherwise unrelated) proximity to the perihelion stability limit (q ~35 astronomical units [au]), below which Kuiper belt objects (KBOs) quickly become unstable. If the Haumea family was formed at lower eccentricity, the effects of Neptune's migration (and jump) would cause the family to expand greatly in eccentricity, with far fewer family members being ejected from the solar system. While the circumstances of the Haumea family's formation obviously contribute to its detectability (large, bright family members with extremely unique surfaces), its location near the perihelion stability limit also likely plays a role in its early identification. Other (currently hypothetical) KBO families formed at this time may have been significantly diluted by Neptune's migration, rendering them undetectable.

In summary, we have identified a formation mechanism that can match all known aspects of the Haumea family. We propose that Haumea and the family were formed in the aftermath of a binary collision. This family, due to the conditions of the graze-and-merge collision, was ejected at low velocity (**Δv** ~ 150 m s^{-1}) in a planar ejection pattern. This ejection pattern, which is not found in the observed family members, was subsequently erased by Neptune's outward migration. Our integrations outlined here show that the mixing of a family from Neptune migration is a common and expected outcome in the final stages of planetary migration, despite previously held beliefs that Neptune migration would destroy the family. Even though we found a significant mixing effect, the family is not excessively eroded or expanded. We expect that these results and conclusions will significantly shape any future study of the Haumea family, and may even help to place constraints on Neptune's final stages of migration.

Methods

Numerical integrations. In our numerical integrations, the motions of the outer planets are tracked, along with 250 test particles representing a simulated graze-and-merge family. The Neptune migration model we use follows Nesvorny[26]. This model has Neptune migrating outwards and having a discontinuous jump at ~28.0 au. It can be easily parameterized to create any size jumps in Neptune's orbital parameters a_N and e_N. This allows for easy comparison to previous works, where testing in a very similar manner was done.

This jump, or more accurately a mild instability, is thought to be required to create the so-called kernel in the cold classical population[26]. The jump in these models is the consequence of a planet–planet scattering event after Neptune has ejected another ice giant planet out of the solar system, which has been shown to reliably create a final solar system architecture similar to ours today[29]. The existence of such a jump has been supported across a variety of works[27,31–33].

To set up these integrations, Jupiter, Saturn, and Uranus are placed on orbits with semi-major axes and inclinations equal to their current semi-major axes and inclinations. We place Neptune interior to its current orbit ($a_{N,0} = 26.0$ au) with zero inclination. All the outer planets are started with zero eccentricity. In addition to the outer planets, we place a prototypical graze-and-merge type family into the integrations as test particles.

Our numerical integrations rely on REBOUND[28], using the WHFAST symplectic integration scheme[34]. In it, we insert additional forces[35] to migrate Neptune's semi-major axis and damp its eccentricity on a single e-folding timescale, $\tau = 50$ Myr. The timescale used here is similar to timescales shown to match the properties of the outer solar system[26,27]. Neptune was migrated outwards until a_N ~ 28.0 au. We then instantaneously change Neptune's orbit such that $a_N = 28.5$ au and $e_N = 0.05$ or 0.1. This brackets the range of Δe that was found to be suitable for producing the Kuiper Belt kernel. After this change, the integration was allowed to continue until the total duration was 1 Gyr. In each case, multiple runs were considered, with each run adjusting the migration amplitude so that Neptune's final semi-major axis was within 1% of its current semi-major axis. This was specifically done to best reproduce the locations of Neptune's MMRs with respect to the family. The most promising integrations were extended in a pure n-body model by 4.5 GYr to show how the family would appear today. These long-term integrations showed very little additional evolution except for some resonant diffusion, consistent with previous analyses[36,37].

One shortcoming of our integrations was the non-realistic outer planet eccentricities. Jupiter, Saturn, and Uranus were placed on circular orbits to reduce the chances of massive dynamical instabilities among the outer planets. When tested against integrations with realistic eccentricities, the integrations were almost identical. As Neptune is subject to eccentricity damping throughout the integrations, the coupling between the eccentricities of Jupiter/ Saturn/Uranus and Neptune was broken. This allows for the survival of the family through Neptune's migration, even during the strong resonance sweeping the family is subjected to. Furthermore, only Neptune's eccentricity is important for Kuiper Belt dynamics. We remind the reader that these integrations are a proof of concept to show that the Haumea family could have survived Neptune's migration.

In addition to these integrations with a jumping Neptune, we also completed several exploratory integrations to determine the dominant mechanism for family mixing observed in the other integrations. These were not designed to match existing proposed Neptune migration schemes, unlike our nominal model. We had three classes of integrations to test this.

First, we completed many integrations where we have Neptune migration but no jump in eccentricity. Initial conditions of Neptune were the same as above, with the inclusion of a jump of 0.5 au when Neptune reached ~28.0 au. This determines whether a jump in the semi-major axis only is responsible for the mixing observed in our jumping Neptune model.

Secondly, we performed several integrations with a smoothly migrating Neptune with no jumps in semi-major axis or eccentricity. Allowing us to determine if smooth migration was key to the mixing.

Lastly, we completed integrations with eccentricity jumps without Neptune migration. In these integrations, Neptune has its current semi-major axis but was started with $e = 0.1, 0.05, 0.025$. This (somewhat) separates the effect of heightened eccentricity in the immediate aftermath of Neptune's jump from both the migration of Neptune and the jump in Neptune's semi-major axis. Eccentricity damping was implemented to match Neptune's current eccentricity of near zero.

Using these additional integrations, we found that the majority of mixing was caused by increased eccentricity immediately after Neptune's jump. While the semi-major axis jump did enhance the mixing when compared to smooth migration, it was not as clear as the eccentricity-driven mixing.

Synthetic families. In each integration, a simulated graze-and-merge family was inserted. To facilitate comparison between integrations, the same family was used in all the integrations. This family was chosen as a representative and likely example of a graze-and-merge collision that would be relatively difficult to mix. Using a family generation method, as outlined in Proudfoot and Ragozzine[3] (hereafter PR19), we created a family consisting of 250 simulated family members ejected with a planar concentration parameter corresponding to a vertical dispersion from a plane of ~2° and with collision center orbital elements (43.1 au, 0.125, 28.2°). The method described in PR19 takes the collision center orbital elements, along with a number–size–velocity distribution for ejected family members and creates a simulated collisional family. The other parameters used to specify the number–size–velocity distribution of simulated family members are $\alpha = 0.2$, $\beta = 0.1$, $S = 0.8$, $k = 1.5$, and $\lambda = 1.7$; see PR19 for full details.

ARTICLE
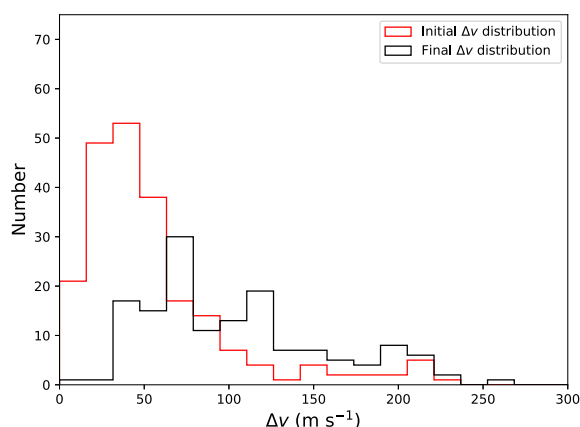
Fig. 4 Dispersion of family members during Neptune migration.
Displayed are histograms of the final $\Delta\mathbf{v}$ distribution (in black) compared to
the initial $\Delta\mathbf{v}$ distribution (in red) for our integration. As the $\Delta\mathbf{v}$ distribution
was found based on the 50 Myr averaged orbital elements, the initial
distribution already deviates slightly from the original distribution. During
the period of chaotic diffusion in the first few hundred Myr of our
integrations, family members tend to increase their $\Delta\mathbf{v}$, resulting in the
distribution shown where the median $\Delta\mathbf{v}$ is about twice the initial median
$\Delta\mathbf{v}$. Source data for this figure are provided as a Source data file.

Although all of the integrations we show in this work contain the planar prototype
family, many of the exploratory integrations, as well as preliminary runs of our a, e
jump integrations were completed with other realizations of a graze-and-merge
family. Throughout our testing process, while using other graze-and-merge families,
some families were easier to mix than others, but we conclude that a wide variety of
graze-and-merge families are susceptible to mixing through Neptune migration. The
chosen family represents a fairly typical graze-and-merge family, with the planar
ejection direction chosen to create an initially strong *a-e-i* correlation.

PR19-style testing. To determine whether Neptune migration erased the *a-e-i*
correlations of a graze-and-merge family, we fit each family using the methods of
PR19. That method uses a Bayesian parameter inference framework to infer orbital
elements of the collision center, the number-size-velocity distribution of the ejec-
tion, and the shape of the ejection field. This is done by creating synthetic families,
characterizing them with multivariate normal distributions, and comparing them
to a random set of 22 family members chosen from our integrations. The synthetic
families are parameterized by 13 parameters (3 parameters describing the planar
shape of the family, 5 parameters for the orbital elements of the collision center,
and 5 parameters describing the number-size-velocity distribution of family
members following Lykawka et al.[38]. The key parameter that is important to our
analysis is the angular dispersion parameter, κ, which characterizes the isotropy/
planar-ness of the family. Practically everything about these fits was identical to the
method in PR19. As our model is composed entirely of known family members, we
do not include the interloper fraction used in PR19. We use the same priors, a 10^5
step burn-in, and 10^5 step sampling which showed excellent convergence. For a
more in-depth treatment of these methods, see PR19.

$\Delta\mathbf{v}$ comparisons. We compare the $\Delta\mathbf{v}$ distributions of the family at the earliest
point in the integration with the $\Delta\mathbf{v}$ distribution at the end of the integration. To do
this, we do not a priori choose the collision orbital elements, as there is significant
uncertainty to the true collision orbital elements of the Haumea family. Instead, we
choose the collision orbital elements by minimizing the sum of the $\Delta\mathbf{v}$ of each
family member, similar to the previous works[5]. This comparison is shown in Fig. 4,
for the integration. The comparison is extremely similar to our other preliminary
integrations. In both integrations, the $\Delta\mathbf{v}$ distribution is somewhat broadened
throughout the integration, roughly doubling the median $\Delta\mathbf{v}$ of the family, but
keeping most within $\Delta\mathbf{v} < 150$ m s^{-1} as is observed.

Data availability
All data used and generated in this work have been permanently stored and backed up on the
authors' local drives and backups. This includes Simulation Archive files containing all details
of our simulations and chain files produced in our PR19-style analysis. While these data are
not stored publicly due to their large sizes, it is available to anyone, without condition, upon
request from the corresponding author. Source data are provided with this paper.

Code availability
REBOUND (and its integrator WHFAST) is publicly available code made available at
https://github.com/hannorein/rebound. All other codes, including plotting codes,
integration codes, and PR19 testing codes, were custom developed for this work. It is
available, without conditions, upon request from the corresponding author.

References
1. Brown, M. E., Barkume, K. M., Ragozzine, D. & Schaller, E. L. A collisional
    family of icy objects in the Kuiper belt. *Nature* **446**, 294–296 (2007).
2. Meschiari, S. & Laughlin, G. P. Systemic: a testbed for characterizing the
    detection of extrasolar planets. II. Numerical approaches to the transit timing
    inverse problem. *Astrophys. J.* **718**, 543–550 (2010).
3. Proudfoot, B. C. & Ragozzine, D. Modeling the formation of the family of the
    dwarf planet Haumea. *Astron. J.* **157**, 230 (2019).
4. Leinhardt, Z. M. & Stewart, S. T. Collisions between gravity-dominated bodies.
    I. Outcome regimes and scaling laws. *Astrophys. J.* **745**, 79 (2012).
5. Ragozzine, D. & Brown, M. E. Candidate members and age estimate of the
    family of Kuiper belt object 2003 EL61. *Astron. J.* **134**, 2160–2167 (2007).
6. Marcus, R. A., Ragozzine, D., Murray-Clay, R. A. & Holman, M. J. Identifying
    collisional families in the Kuiper belt. *apj* **733**, 40 (2011).
7. Pike, R. E. et al. A dearth of small members in the Haumea family revealed by
    OSSOS. *Nat. Astron* **4**, 89–96 (2020).
8. Schlichting, H. E. & Sari, R. The creation of Haumea's collisional family.
    Astrophys. J. **700**, 1242–1246 (2009).
9. Leinhardt, Z. M., Marcus, R. A. & Stewart, S. T. The formation of the collisional
    family around the dwarf planet Haumea. *Astrophys. J.* **714**, 1789–1799 (2010).
10. Ortiz, J. L. et al. Rotational fission of trans-Neptunian objects: the case of
    Haumea. *Mon. Not. R. Astron. Soc.* **419**, 2315–2324 (2012).
11. Campo Bagatin, A., Benavídez, P. G., Ortiz, J. & Gil-Hutton, R. On the genesis
    of the Haumea system. *Mon. Not. R. Astron. Soc.* **461**, 2060–2067 (2016).
12. Brown, M. E., Barkume, K. M., Ragozzine, D. & Schaller, E. L. Discovery of an
    icy collisional family in the Kuiper belt. *Nature* **446**, 294–296 (2007).
13. Schaller, E. L. & Brown, M. E. Detection of additional members of the 2003
    EL61 collisional family via near-infrared spectroscopy. *Astrophys. J. Lett.* **684**,
    L107–L109 (2008).
14. Elliot, J. L. et al. Size and albedo of Kuiper belt object 55636 from a stellar
    occultation. *Nature* **465**, 897–900 (2010).
15. Vilenius, E. et al. "TNOs are Cool": a survey of the trans-Neptunian region-
    XIV. Size/albedo characterization of the Haumea family observed with
    Herschel and Spitzer. *Astron. Astrophys.* **618**, A136 (2018).
16. Levison, H. F., Morbidelli, A., Vokrouhlický, D. & Bottke, W. F. On a
    scattered-disk origin for the 2003 EL$_{61}$ collisional family — an example of
    the importance of collisions on the dynamics of small bodies. *Astron. J.* **136**,
    1079–1088 (2008).
17. Perets, H. B. & Naoz, S. Kozai cycles, tidal friction, and the dynamical
    evolution of binary minor planets. *Astrophys. J. Lett.* **699**, L17 (2009).
18. Porter, S. B. & Grundy, W. M. KCTF evolution of trans-neptunian binaries:
    connecting formation to observation. *Icarus* **220**, 947–957 (2012).
19. Rozner, M., Grishin, E. & Perets, H. B. The wide-binary origin of the Pluto-
    Charon system. *Mon. Not. R. Astron. Soc.* **497**, 5264–5270 (2020).
20. Noviello, J., Desch, S. & Neveu, M. Haumea's formation and evolution from a
    graze-and-merge impact. In *Lunar and Planetary Science Conference* 2894
    (LPI, 2020).
21. Robinson, J. E., Fraser, W. C., Fitzsimmons, A. & Lacerda, P. Investigating
    gravitational collapse of a pebble cloud to form transneptunian binaries.
    Astron. Astrophys. **643**, A55 (2020).
22. Nesvorný, D. & Vokrouhlický, D. Binary survival in the outer solar system.
    Icarus **331**, 49–61 (2019).
23. Agnor, C. B. & Hamilton, D. P. Neptune's capture of its moon Triton in a
    binary-planet gravitational encounter. *Nature* **441**, 192–194 (2006).
24. Morbidelli, A. & Nesvorný, D. Kuiper belt: formation and evolution. *Trans-
    Neptunian Sol. Syst.* 25–59 (2020).
25. Brown, M., Ragozzine, D., Stansberry, J. & Fraser, W. The size, density, and
    formation of the Orcus-Vanth system in the Kuiper belt. *Astron. J.* **139**, 2700
    (2010).
26. Nesvorný, D. Jumping Neptune can explain the Kuiper belt kernel. *Astron. J.*
    150, 68 (2015).
27. Nesvorny, D. et al. OSSOS XX: the meaning of Kuiper belt colors. *Astron. J.*
    160, 46 (2020).
28. Rein, H. & Liu, S.-F. REBOUND: an open-source multi-purpose N-body code
    for collisional dynamics. *Astron. Astrophys.* **537**, A128 (2012).

ARTICLE   NATURE COMMUNICATIONS | https://doi.org/10.1038/s41467-022-29901-5

29. Nesvorný, D. & Morbidelli, A. Statistical study of the early solar system's instability with four, five, and six giant planets. *Astron. J.* **144**, 117 (2012).
30. Gomes, R., Nesvorný, D., Morbidelli, A., Deienno, R. & Nogueira, E. Checking the compatibility of the cold Kuiper belt with a planetary instability migration model. *Icarus* **306**, 319–327 (2018).
31. Nesvorný, D. Eccentric early migration of Neptune. *Astrophys. J. Lett.* **908**, L47 (2021).
32. de Sousa, R. R., Gomes, R., Morbidelli, A. & Neto, E. V. Dynamical effects on the classical Kuiper belt during the excited-Neptune model. *Icarus* **334**, 89–98 (2019).
33. Lawler, S. et al. OSSOS. XIII. Fossilized resonant dropouts tentatively confirm Neptune's migration was grainy and slow. *Astron. J.* **157**, 253 (2019).
34. Rein, H. & Tamayo, D. WHFAST: a fast and unbiased implementation of a symplectic Wisdom–Holman integrator for long-term gravitational simulations. *Mon. Not. R. Astron. Soc.* **452**, 376–388 (2015).
35. Hahn, J. M. & Malhotra, R. Neptune's migration into a stirred-up Kuiper belt: a detailed comparison of simulations to observations. *Astron. J.* **130**, 2392–2414 (2005).
36. Rabinowitz, D. L., Schaefer, B. E. & Tourtellotte, S. W. Photometric properties of the 2003 El61 collisional family. A recent origin? *Bull. Am. Astron. Soc.* **39**, 491 (2007).
37. Volk, K. & Malhotra, R. The effect of orbital evolution on the Haumea (2003 EL$_{61}$) collisional family. *Icarus* **221**, 106–115 (2012).
38. Lykawka, P. S., Horner, J., Mukai, T. & Nakamura, A. M. The dynamical evolution of dwarf planet (136108) Haumea's collisional family: general properties and implications for the trans-Neptunian belt. *Mon. Not. R. Astron. Soc.* **421**, 1331–1350 (2012).

Acknowledgements

Author contributions
B.P. performed all integrations, analysis, and coding required for this work. D.R. advised in all activities and helped with writing, editing, and interpreting results.

Competing interests
The authors declare no competing interests.

Additional information
Supplementary information The online version contains supplementary material available at https://doi.org/10.1038/s41467-022-29901-5.

Correspondence and requests for materials should be addressed to Benjamin Proudfoot.

Peer review information *Nature Communications* thanks the anonymous reviewers for their contribution to the peer review of this work. Peer reviewer reports are available.

Reprints and permission information is available at http://www.nature.com/reprints

Publisher's note Springer Nature remains neutral with regard to jurisdictional claims in published maps and institutional affiliations.

Chapter 3

Beyond Point Masses II: Non-Keplerian Shape Effects are Detectable in TNO Binaries

The content of this chapter has been submitted to The Astronomical Journal. It is currently undergoing peer review with one round of revisions already completed. The version below is a preprint version in journal specific style.

The work presented in this Chapter is the culmination of D. Ragozzine's Physics 227 (Solar System Astronomy) class project. Students helped by assessing fit quality, ensuring convergence of the Markov chains, and compiling results. Each student spent approximately 10-15 hours over the course of the semester contributing to the project, earning them co-authorship. As such, the submitted paper has over 60 student co-authors.

Beyond Point Masses: Non-Keplerian Shape Effects are Detectable in TNO Binaries

BENJAMIN C.N. PROUDFOOT,[1] DARIN A. RAGOZZINE,[1] MEAGAN L. THATCHER,[1] WILL GRUNDY,[2] DALLIN J. SPENCER,[1]
TAHINA M. ALAILIMA,[1] SAWYER ALLEN,[1] PENELOPE C. BOWDEN,[1] SUSANNE BYRD,[1] CONNER D. CAMACHO,[1]
GIBSON H. CAMPBELL,[1] EDISON P. CARLISLE,[1] JACOB A. CHRISTENSEN,[1] NOAH K. CHRISTENSEN,[1] KAELYN CLEMENT,[1]
BENJAMIN J. DERIEG,[1] MARA K. DILLE,[1] CRISTIAN DORRETT,[1] ABIGAIL L. ELLEFSON,[1] TAYLOR S. FLEMING,[1]
N. J. FREEMAN,[1] ETHAN J. GIBSON,[1] WILLIAM G. GIFOROS,[1] JACOB A. GUERRETTE,[1] OLIVIA HADDOCK,[1]
S. ASHTON HAMMOND,[1] ZACHARY A. HAMPSON,[1] JOSHUA D. HANCOCK,[1] MADELINE S. HARMER,[1] JOSEPH R. HENDERSON,[1]
CHANDLER R. JENSEN,[1] DAVID JENSEN,[1] RYLEIGH E. JENSEN,[1] JOSHUA S. JONES,[1] CAMERON C. KUBAL,[1]
JACOB N. LUNT,[1] STEPHANIE MARTINS,[1] MCKENNA MATHESON,[1] DAHLIA MAXWELL,[1] TIMOTHY D. MORRELL,[1]
MCKENNA M. MYCKOWIAK,[1] MAIA A. NELSEN,[1] SPENCER T. NEU,[1] GIOVANNA G. NUCCITELLI,[1] KAYSON M. REARDON,[1]
AUSTIN S. REID,[1] KENNETH G. RICHARDS,[1] MEGAN R. W. ROBERTSON,[1] TANNER D. RYDALCH,[1] CONNER B. SCORESBY,[1]
RYAN L. SCOTT,[1] ZACORY D. SHAKESPEAR,[1] ELLIOT A.SILVEIRA,[1] GRACE C. STEED,[1] CHRISTIANA Z. SUGGS,[1]
GARRETT D. SUGGS,[1] DEREK M. TOBIAS,[1] MATTHEW L. TOOLE,[1] MCKAYLA L. TOWNSEND,[1] KADE L. VICKERS,[1]
COLLIN R. WAGNER,[1] MADELINE S. WRIGHT,[1] AND EMMA M. A. ZAPPALA[1]

[1]*Brigham Young University Department of Physics & Astronomy, N283 ESC, Brigham Young University, Provo, UT 84602, USA*
[2]*Lowell Observatory, Flagstaff, AZ, USA*

ABSTRACT

About 40 transneptunian binaries (TNBs) have fully determined orbits with about 10 others being solved except for breaking the mirror ambiguity. Despite decades of study almost all TNBs have only ever been analyzed with a model that assumes perfect Keplerian motion (e.g., two point masses). In reality, all TNB systems are non-Keplerian due to non-spherical shapes, possible presence of undetected system components, and/or solar perturbations. In this work, we focus on identifying candidates for detectable non-Keplerian motion based on sample of 45 well-characterized binaries. We use `MultiMoon`, a non-Keplerian Bayesian inference tool, to analyze published relative astrometry allowing for non-spherical shapes of each TNB system's primary. We first reproduce the results of previous Keplerian fitting efforts with `MultiMoon`, which serves as a comparison for the non-Keplerian fits and confirms that these fits are not biased by the assumption of a Keplerian orbit. We unambiguously detect non-Keplerian motion in 8 TNB systems across a range of primary radii, mutual orbit separations, and system masses. As a demonstration of the usefulness of our results, we perform detailed fits for (66652) Borasisi-Pabu, revealing a $J_2 \approx 0.44$, implying Borasisi (and/or Pabu) is a contact binary or an unresolved compact binary. This work begins the next generation of TNB analyses that go beyond the point mass assumption to provide unique and valuable information on the physical properties of TNBs with implications for their formation and evolution.

Keywords: planetary systems

1. INTRODUCTION

Since the discovery and characterization of the mutual binary orbit of the transneptunian object (TNO) 1998 WW31 (Veillet et al. 2002), transneptunian binaries (TNBs) have been recognized as sensitive tracers of the history of the solar system. Acting as a detailed

Corresponding author: Benjamin Proudfoot
benp175@gmail.com

laboratory that enables mass measurements, TNBs open the door for remote characterization of TNOs as a whole (e.g., Grundy et al. 2007; Grundy et al. 2009; Fraser & Brown 2010; Barr & Schwamb 2016). In addition, the mutual orbital properties of a binary system provide insight into the formation and history of that binary system, as those properties encode information about the binary's formation (e.g., Brown & Schaller 2007; Brown et al. 2010), past tidal evolution (e.g., Porter & Grundy 2012; Arakawa et al. 2021), collisional history (e.g., Ragozzine & Brown 2009; Parker & Kavelaars

2011), and encounters with other bodies (e.g., Campbell et al. 2022). The statistical ensemble of mutual orbit properties of TNBs also hold valuable clues about the conditions of the protoplanetary disk from which TNBs originally formed and have revealed groundbreaking insights into the dominant formation processes in that disk (e.g., Nesvorný et al. 2010; Grundy et al. 2019; Nesvorný et al. 2019).

While the numerous studies of TNBs have enabled unprecedented understanding of processes in the outer solar system, it has become clear that current state-of-the-art methods are lagging behind the growing observational baselines of TNBs. These methods, for the most part, rely on simple Keplerian orbital models, with only a few exceptions. In recent years, however, many authors have found that the observed relative astrometric positions of TNBs show statistically significant deviations from plain Keplerian orbits (Salacia-Actaea 3.7σ, Orcus-Vanth 2.2σ, Grundy et al. (2019); Eris-Dysnomia 6.3σ, Holler et al. (2021)). An analysis of the distribution of χ^2 values of all TNB fits also shows a statistically significant excess of poor fits. While these deviations could be the result of unidentified systematic errors in data collections/measurement, it is also likely that the deviations are the manifestation of inaccurate models including non-Keplerian gravitational effects acting in TNB systems.

Non-Keplerian gravitational effects are any gravitational effect that forces an orbit to deviate from a pure Keplerian orbit. Generally, non-Keplerian effects result in slow precession of an orbit's orientation angles. Precession of the direction of periapse is called apsidal precession, and precession of the orbit pole is called nodal precession. While there are many possible sources of non-Keplerian effects, the most relevant sources for TNBs are the non-spherical shapes of individual TNB components, systems with more than 2 components (whether known or unknown), and the external gravitational influence of the Sun (see Ragozzine et al. (2023) for more details).

In this paper, we will focus on detecting and measuring the strength of non-Keplerian effects attributable to shape or unknown components, leaving non-Keplerian effects from solar influences to future study. In Section 1.1, we discuss the causes and consequences of non-Keplerian shape effects. Next, in Section 1.2, we explain the general process of our non-Keplerian orbit fitting. In Section 2.2 and Section 2.3, we discuss our methods for both Keplerian and non-Keplerian orbital fitting applied herein. In Section 2.1, we detail our TNB sample and gather publicly available relative astrometric data. In Section 3, we discuss the results of our Keplerian

orbit fits and reproduce past fitting results. Next, in Section 4, we present the results of our search for non-Keplerian effects, discuss the implications of these results, and identify the most promising targets for future investigation. Then, in Section 5, we perform a full non-Keplerian analysis of TNB (66652) Borasisi-Pabu, one of the most promising cases of non-Keplerian motion in a TNB, as a proof-of-concept of full non-Keplerian fitting. Lastly, in Section 6, we discuss our conclusions.

1.1. *Non-Keplerian Shape Effects*

Keplerian orbital models implicitly assume that the individual components of a TNB system are point masses (or equivalently perfect spheres). However, it is well-documented that the shapes of TNOs can be significantly non-spherical (e.g., Sheppard & Jewitt 2004; Ortiz et al. 2017). Moving beyond point masses, non-spherical shapes must cause non-Keplerian deviations in TNB orbits, though the importance of these deviations relative to present or future observational data has not yet been previously examined in detail.

Gravitational potentials of non-spherical bodies can be modeled using a spherical harmonic expansion of the gravitational potential. Current data warrant exploring the gravitational potential only at second order; by construction, higher order corrections are less important and neglected in our analysis. Ragozzine et al. (2023) provide a detailed discussion of these and other effects and how they can be modeled which we summarize here.

The second-order gravitational potential, U, of a mass M at distance r, can be written:

$$U(r, \theta, \phi) = -\frac{GM}{r}\left[1 - J_2\left(\frac{R}{r}\right)^2\left(\frac{3}{2}\sin^2\theta - \frac{1}{2}\right)\right.$$
$$\left. + C_{22}\left(\frac{R}{r}\right)^2\cos^2\theta\sin 2\phi + \mathcal{O}\left(r^{-3}\right)\right] \quad (1)$$

where J_2 is the second-order zonal gravitational harmonic and C_{22} is the second-order sectoral gravitational harmonic coefficient, θ is the body-fixed latitude-like angle, ϕ is the body-fixed longitude-like angle (chosen to eliminate other terms), and R is a reference radius (Yoder 1995; Scheeres et al. 2000). J_2 is a measure of the oblateness of the potential and C_{22} is related to the prolateness, or the ellipticity of the equator. Generally, for extremely spherical bodies (like the Earth) $J_2 \lesssim 0.001$, extremely oblate bodies (like Haumea) $J_2 \sim 0.1$, and contact binaries have $J_2 \sim 0.3$.

For most TNBs, where the TNBs mutual orbit is much slower than the rotations of the individual components, C_{22} has little effect on the dynamics of the mutual orbit, as the contribution from C_{22} averages out. However,

near spin-orbit resonances, which may be present among some TNB systems, C_{22} may not fully average out and may play a significant role in the dynamics of the system (Proudfoot & Ragozzine 2021). We consider this to be a special case not relevant to most TNBs. Since we are exploring the entire ensemble of TNBs, we focus this analyses on J_2 alone. Implications for this choice are discussed further in Section 5.

The dynamics of a system with a J_2 can be described by slow apsidal and nodal precession. For a test particle orbiting around a body with a J_2, the apsidal and nodal secular rates can be written:

$$\dot{\omega} = -\frac{3nJ_2R^2}{2a^2(1-e^2)^2}\left(\frac{5}{2}\sin^2 i - 2\right) \qquad (2)$$

$$\dot{\Omega} = -\frac{3nJ_2R^2}{2a^2(1-e^2)^2}\cos i \qquad (3)$$

where n is the mean motion, a is the semi-major axis, e is the eccentricity, and i is the inclination of the orbit relative to the body's equator. As discussed in Ragozzine & Brown (2009), and is clear from Equations 2 and 3, the non-Keplerian motion induced by the gravitational harmonics require knowledge of both the strength of the gravitational harmonics *and* the direction of the spin axis (to determine the appropriate θ and ϕ values in Equation 1 or to determine the appropriate inclination in equations 2 and 3). Thus, detection of non-Keplerian effects allows constraints to be placed on both TNO shapes and spin poles (assumed to be identical to the quadrupolar gravitational harmonic pole appropriate for TNOs which are too large to sustain long-term non-principal axis rotation).

From Equations 1, 2, and 3, it can be seen that the measurable quantity is J_2R^2 (and $C_{22}R^2$) and not J_2 independently. This is extremely similar to the quantity GM, where the gravitational constant and mass are always paired together. The interpretation of J_2R^2 in terms of an object's shape requires first the choice of a shape model. For example, assuming a homogeneous oblate ellipsoid with semi-axes $a = b \geq c$ gives $\frac{a}{c} = \frac{b}{c} = \sqrt{5\frac{J_2R^2}{c^2}+1}$. Different shape models can match the observed J_2R^2 even given a specific mass (see, e.g., Marchis et al. 2005b; Ragozzine et al. 2023) and the shape model influences the choice of R and thus J_2. Unknown contact and compact binaries can also result in an apparent J_2R^2, as discussed below. Except for the largest TNOs, J_2R^2 is dominated by the overall shape of the object and not the interior density distribution.

However, the inability to determine a precise shape or interior composition with J_2R^2 should not detract from the fact that measuring a significant J_2R^2 has impor-

tant implications for the object. For example, different formation modes can result in different J_2R^2 values with catastrophic collisions reaccumulating into nearly spherical objects while high angular momentum formation processes tending to form more non-spherical shapes. Of course, the strength of J_2R^2 affects long-term spin-orbit-tidal dynamics and evolution of the TNBs themselves (e.g., Correia 2018). The measurement of J_2R^2 also provides mostly orthogonal constraints on shape properties, so that it improves the interpretation of light curves, occultations, and thermal measurements.

The rotation poles of TNOs have also proved to be difficult to constrain, although some success has been seen among the Centaurs (e.g., Tegler et al. 2005; Duffard et al. 2014). Until now, determination of shape has relied on both light curve and occultation studies. While light curves are powerful tools for understanding shape and spin, the shape and spin solutions produced are non-unique (Harris & Warner 2020). Additionally, light curve inversion requires observations of the target at a variety of aspects, which is implausible for most TNOs due to their centuries-long heliocentric orbital periods. On the other hand, occultations can directly observe the shape of a TNO in a projected plane (e.g., Elliot et al. 2010; Benedetti-Rossi et al. 2016; Ortiz et al. 2017), placing limits on the full 3-dimensional shape of a body when combined with a light curve. However, due to the random timing of the events and difficulty of observation, occultations cannot yet be used to systematically understand the shapes and spins of TNOs at a population level.

Detection and measurement of non-Keplerian effects thus opens the door to a deeper understanding of TNB systems. While Keplerian orbital fitting allows for determination of mass (and therefore density), non-Keplerian orbit fitting in theory allows for study of the three dimensional shape and spin orientation of the two system components. It is able to provide unique constraints on both the shapes of TNB components and their obliquities[1] (Ragozzine & Brown 2009; Vachier et al. 2012) which are sensitive tracers of formation and evolution (e.g., McKinnon et al. 2020).

1.1.1. *Unknown Components*

Another area where non-Keplerian analysis has significant potential for unique insight is in the detection of unknown components whether in "contact binaries" or simply closely separated objects ("compact binaries"). Many channels of evidence suggest that these are com-

---

[1] Throughout this paper, obliquity will refer to the inclination of the mutual orbit with respect to the primary body's equator.

mon in the TNO population, including light curve studies (Rabinowitz et al. 2019; Thirouin & Sheppard 2018, 2019; Showalter et al. 2021), occultations (Leiva et al. 2020), and imaging from within the TNO population as enabled by the *New Horizons* spacecraft (Weaver et al. 2022). Indeed, the only small TNO ever visited by a spacecraft, Arrokoth, was a contact binary (Stern et al. 2019; McKinnon et al. 2020). Discovering and characterizing contact or tight components in binaries provides unique insight into the angular momentum and mass budget of TNBs.

There is a huge range of parameter space where additional components would be too far away to be seen in light curves or occultations ($\gtrsim 3$ primary radii away) but too close to be resolved in direct imaging ($\lesssim 20$ primary radii away for most TNBs). Non-Keplerian effects, on the other hand, are highly enhanced in both contact and unresolved binaries.

Both non-spherical shapes and additional components primarily cause orbital precession. Indeed, to quadrupole order, the gravitational potential of a close-in, previously undetected satellite is effectively the same as unusually large gravitational harmonics. This means that exploration of non-Keplerian effects using a J_2 shape model is a good starting approximation for detecting additional components. Detecting anomalously large values for J_2 (e.g., $J_2 \gtrsim 1$ when assuming a triaxial shape model), may indicate that there are additional undetected system components.

Using the definitions of the gravitational harmonics from Yoder (1995), we find that the 'effective' J_2 and C_{22} of a close-in satellite would be

$$J_2 R^2 = \frac{1}{2} \frac{q}{(1+q)^2} a_s^2 \qquad (4)$$

$$C_{22} R^2 = \frac{1}{4} \frac{q}{(1+q)^2} a_s^2 \qquad (5)$$

where $q = m_s/m_p$, m_p and m_s are the masses of the masses of the primary and (unresolved) secondary, respectively, and a_s is the semi-major axis of the secondary's orbit. In this equation, we leave the combinations $J_2 R^2$ and $C_{22} R^2$ since these are the physically meaningful parameters (see Equation 1). It is possible to understand these contact/compact binaries as one end of the continuum of shape modeling that converts the measurement of $J_2 R^2$ into a physical configuration of mass.

These contact and compact binaries describe one (or both) of the components of an existing TNB, converting binaries into hierarchical triples (or quadruples). These systems, only one of which was previously known (Lempo; Benecchi et al. 2010), are common outcomes of

gravitational collapse simulations (Nesvorný et al. 2010; Robinson et al. 2020; Nesvorný et al. 2021), although they may also be able to form through capture mechanisms (Brunini & López 2020). Regardless of their origin, discovering additional Lempo-like systems will aid in understanding the formation of TNBs.

1.1.2. *Expectations for Non-Keplerian Effects*

While non-Keplerian fitting does have a variety of drawbacks and degeneracies (see further discussion in Ragozzine et al. (2023)), it is another powerful tool for understanding TNOs at a deeper level. Detecting non-Keplerian effects may allow for a new suite of unique measurements leading to a significant improvement in understanding TNBs, but the fraction of systems with detectable effects (with current or potentially future data) has been unknown. Non-Keplerian effects of multiple moons has been robustly detected in the Haumea system (Ragozzine & Brown 2009), but no J_2 precession has ever been robustly detected in any TNB system, despite attempts (e.g., Ragozzine & Brown 2009; Gourgeot et al. 2016).

There is good reason, however, to expect that non-Keplerian shape effects are common and detectable. Firstly, aspherical shapes are common among TNOs, as shown by the results of occultation observations (e.g., Elliot et al. 2010; Benedetti-Rossi et al. 2016; Ortiz et al. 2017). These shapes, assuming that TNOs are not all differentiated, should produce detectable non-Keplerian effects over the current observational baselines. Secondly, detection of J_2 is common in both main-belt asteroids and near-Earth asteroids (e.g., Marchis et al. 2005a,b; Fang et al. 2011, 2012; Vachier et al. 2012; Beauvalet & Marchis 2014; Marchis et al. 2014). For example, Marchis et al. (2005b) unambiguously detected the J_2 of the asteroid (121) Hermione based on the orbit of its small companion, with observations spanning less than a single year. While TNBs generally have longer period orbits than asteroid binaries, several TNBs have relative astrometric measurements now reaching decade long timescales. The observational baselines and high quality data strongly suggest that non-Keplerian effects would be detectable in at least a few TNBs.

To test the detectability of non-Keplerian effects in TNBs, we created synthetic relative astrometry for all TNBs, assuming the primary and secondary were interacting triaxial bodies with realistic shapes. The synthetic astrometry had realistic uncertainties added and was made to simulate the quantity and quality of real TNB relative astrometry by using existing datasets as templates. We then fitted the astrometry with Keplerian orbits to find if a Keplerian model provided ade-

quate fits to the data. In many cases, we found that our synthetic astrometry was significantly inconsistent with a simple Keplerian model. We found the inconsistencies were strongest among TNBs with large primaries, although many near-equal sized binaries also exhibited inconsistencies. These results imply that non-Keplerian shape effects should be detectable and relatively common among TNBs.

If it is indeed true that non-Keplerian effects are common in TNBs, it also raises questions about the validity of past results based on Keplerian orbital analyses. In most scenarios, Keplerian fitting should yield a similar orbit to a non-Keplerian fit, especially in the parameters not describing the orbit's orientation (e.g., total system mass, semi-major axis, and eccentricity). Some results, however, depend on the orientation of the orbits (e.g., Grundy et al. 2019), which slowly precess over time in a non-Keplerian framework. The systematic error introduced by this model misspecification needs to be evaluated to determine whether past research needs to be reevaluated.

1.2. *Non-Keplerian Orbit Fitting*

For all of its benefits, orbit fitting of non-Keplerian orbits can be a difficult task. While the potential of triaxial body, given in Equation 1, is relatively simple and could be integrated without much trouble[2], the actual dynamics of TNBs can be much more complicated. Not only can both a TNB's primary and secondary both have aspherical shapes with arbitrary rotation poles, but the gravitational interactions between the bodies cause a torque on those bodies, forcing precession of those rotation poles. The torques, which we call "back torques," can make the dynamics of a TNB system much more complicated, especially when the binary is near-equal mass. Many past studies – both observational and theoretical – of non-Keplerian motion in asteroid binaries have neglected the effects of back torques. While this assumption is valid for very small secondaries (like many asteroid binaries), TNBs are often near-equal mass. The complexity involved in TNB spin-orbit dynamics requires the use of a coupled spin-orbit integrator, which can simultaneously integrate the translational and rotational equations of motion.

For this reason, we developed a new spin-orbit integrator, named SPINNY, which is able to self-consistently model coupled spin-orbit motion of an arbitrary number of gravitationally interacting triaxial ellipsoids, in-

cluding the effect of back torques on the spinning bodies. SPINNY makes up the core of MultiMoon, a package designed for non-Keplerian orbit fitting using state-of-the-art Bayesian techniques. Both SPINNY and MultiMoon are described in full detail in Ragozzine et al. (2023) and are publicly available at https://github.com/dragozzine/multimoon, though we discuss the main ideas here. MultiMoon's advanced statistical techniques and orbital model, combined with about a decade worth of relative astrometry for TNBs and extensive parallel computations, now make it possible to conduct a systematic survey to search for non-Keplerian shape effects in TNBs.

Exploration of possible non-Keplerian parameters is generally a difficult task, requiring at least an order of magnitude more computational power than a simple Keplerian analysis. As such, the most interesting targets need to be identified to focus future work. Here, we perform a broad search for the best targets for more detailed non-Keplerian analyses. We focus our efforts on identifying TNBs with the most detectable and statistically significant non-Keplerian effects.

2. METHODS

In this work, for all orbit fitting procedures, we use MultiMoon. MultiMoon is a Python-based Bayesian orbit fitting package specifically designed to complete Keplerian and non-Keplerian orbit fitting of TNBs and other small solar system binaries (Ragozzine et al. 2023). For Keplerian orbit fitting, it uses the SpiceyPy (Annex et al. 2020), a Python implementation of SPICE (Acton Jr 1996), to analytically solve the two-body problem. For non-Keplerian orbits, MultiMoon uses SPINNY which numerically integrates the coupled spin and orbit equations of motion for an arbitrary number of interacting triaxial ellipsoids. These processes produce the position of the secondary relative to the primary. These are projected into the plane of the sky using ephemerides of the TNB system (relative to the Earth) from JPL Horizons, as queried by astroquery (Ginsburg et al. 2019). These ephemerides are corrected for light-time variations and other astrometric aberrations due to Earth's orbital velocity. Light-travel time and conversion to ecliptic coordinates is done as part of the data preparation. For more details, see Ragozzine et al. (2023) or the MultiMoon code itself at https://github.com/dragozzine/multimoon. The analysis herein uses a version of MultiMoon equivalent to Version 1.0. Since our fitting was completed, MultiMoon has been updated to more accurately model the spin dynamics of small secondaries. We have confirmed that

---

[2] using Equations 2 and 3 to calculate time-dependent orbital parameters is actually not much more efficient than full calculations of interacting quadrupoles (Ragozzine et al. 2023)

this small change has no impact on any of the results presented in this work.

The Bayesian parameter inference at the heart of `MultiMoon` is performed by `emcee` (Foreman-Mackey et al. 2013, 2019), a Python-based Markov Chain Monte Carlo (MCMC) ensemble sampler. This allows us to robustly fit orbits in a Bayesian manner. `MultiMoon` uses the same weighted least squares orbit fitting likelihood function that is ubiquitous in TNB orbit fitting (e.g. Grundy et al. 2008, 2009; Ragozzine & Brown 2009; Kiss et al. 2019; Holler et al. 2021, etc.). `MultiMoon` differs from past orbit fitters, however, in that it does not use a downhill optimization technique, but instead uses ensemble MCMC techniques that are robust to local minima. This avoids problems that have occured when using problematic simple minimization techniques (Beauvalet & Marchis 2014). Data weights in our likelihood functions are equal to the inverse square of the measurement uncertainty.

Briefly, the outputs from `MultiMoon` are a posterior probability distribution of inferred parameters given the observational data and priors (which are generally flat and uninformative). Based on the output posteriors, `MultiMoon` produces a variety of different output plots, including both diagnostic plots (e.g., walker trace plots, likelihood plots, etc.) and publication-ready plots (e.g., corner plots, Foreman-Mackey et al. 2016). For more discussion, see Ragozzine et al., submitted.

2.1. *Data*

For all orbital fits completed in this paper, we use publicly available relative astrometric data and orbital fits catalogued in Will Grundy's online TNO database[3], providing the relative astrometry and orbital solutions of 45 TNBs with solved or mirror ambiguous orbits. The list of all the TNBs in our analysis is given in Table 1; note that the meaning of some columns is explained in more detail below. With both relative astrometry and orbital solutions in hand, both are converted into ecliptic coordinates and used in our analysis as described above. All inputs and outputs from our fits are available online[4].

Although the majority of our sample consists of the TNBs whose mutual orbits have been previously studied in the literature, we exclude two systems, (136199) Eris-Dysnomia and (469514) 2003 QA$_{91}$. The Eris-Dysnomia system, whose Keplerian orbit has been extensively studied in the past (Brown & Schaller 2007;

Holler et al. 2021), is known to be $> 6\sigma$ inconsistent with a single Keplerian orbit (Holler et al. 2021). Non-Keplerian orbit fitting (completed with `MultiMoon`) is discussed in Spencer et al., in prep. For 2003 QA$_{91}$, the publicly available relative astrometry (which are compiled in Grundy et al. 2019) are clearly inconsistent with the given orbit solution. We believe that a typographical error is present in the publicly available astrometry. For these reasons, we exclude these systems from our analysis.

Most of the relative astrometry we use is derived from precise images from HST, although significant contributions are made from a variety of other ground-based observatories. Typical error bars on the astrometry from HST are less than 10 milliarcseconds, although they can even be sub-milliarcsecond when observations were taken with HST's High Resolution Camera. We also use many observations from Keck using its adaptive optics system, which typically give measurements with similar precision to HST. For some of the wider TNBs, observations can be obtained with smaller ground-based telescopes like Gemini, Magellan, and the Canada France Hawaii telescope. Given the lower resolution of these telescopes, typical uncertainties can be 100s of milliarcseconds. To get a sense of the typical precision of the observations used for our orbit fitting, we list the median uncertainty of the astrometric measurements in Table 1.

2.2. *Keplerian Orbital Fits*

As a preliminary step to completing non-Keplerian fits, we first completed a round of Keplerian fits to validate our orbit fitting techniques and provide full Bayesian posteriors for the Keplerian orbits of TNBs. This allows us to analyze the quality of the Keplerian fits and provide a baseline for comparison when completing non-Keplerian fits.

Our Keplerian orbital model has seven parameters, including the usual six orbital elements (a, e, i, ω, Ω, and $\mathcal{M}$) and total system mass (M_{sys}). All angles are referenced to the J2000 ecliptic plane (unlike many publications of these TNB orbits which use angles in the equatorial reference frame). We also consider a model with constant photocenter-barycenter offsets which is discussed in Section A.

Our Keplerian fits were run with 100 walkers in the MCMC ensemble, with a 5000 step burn in, pruning of walkers significantly far away from the best parameter space (similar to Proudfoot & Ragozzine 2019; Hou et al. 2012), a 1000 step post-pruning burn in, and a 5000 step sample. We initialized walker positions for all parame-

Table 1. System Properties of TNBs

Object	Primary Rotation Period (h)	Reference	Radius (km)	Reference	Epoch (JD)	Uncertainty (arcsec)
(26308) 1998 SM$_{165}$	8.4	Spencer et al. (2006)	134	Stansberry et al. (2008)	2452700.0	0.001
(42355) Typhon-Echidna	9.67	Duffard et al. (2009)	81	Santos-Sanz et al. (2012)	2454000.0	0.003
(50000) Quaoar-Weywot	8.839	Fornasier et al. (2013)	535	Fornasier et al. (2013)	2454000.0	0.008
(55637) 2002 UX$_{25}$	14.382	Rousselot et al. (2005)	332.5	Fornasier et al. (2013)	2454000.0	0.002
(58534) Logos-Zoe	$\cdots$	$\cdots$	41	Grundy et al. (2011)	2452600.0	0.003
(60458) 2000 CM$_{114}$	$\cdots$	$\cdots$	83.5	assumed	2457000.0	0.004
(65489) Ceto-Phorcus	4.43	Dotto et al. (2008)	111.5	Santos-Sanz et al. (2012)	2453880.0	0.003
(66652) Borasisi-Pabu	6.4	Kern (2006)	63	Vilenius et al. (2014)	2451900.0	0.002
(79360) Sila-Nunam	300.2388	Thirouin et al. (2014)	124.5	Vilenius et al. (2014)	2454400.0	0.004
(80806) 2000 CM$_{105}$	$\cdots$	$\cdots$	80	assumed	2457000.0	0.004
(88611) Teharonhiawako-Sawiskera	9.505	Osip et al. (2003)	89	Vilenius et al. (2014)	2452000.0	0.015
(90482) Orcus-Vanth	13.188	Rabinowitz et al. (2006)	458.5	Brown & Butler (2018)	2454000.0	0.001
(119979) 2002 WC$_{19}$	$\cdots$	$\cdots$	169	Lellouch et al. (2013)	2457000.0	0.006
(120347) Salacia-Actaea	6.5	Thirouin et al. (2014)	427	Brown & Butler (2017)	2454300.0	0.005
(123509) 2000 WK$_{183}$	$\cdots$	$\cdots$	58	Grundy et al. (2011)	2454300.0	0.003
(134860) 2000 OJ$_{67}$	$\cdots$	$\cdots$	69	Grundy et al. (2009)	2457000.0	0.003
(148780) Altjira	$\cdots$	$\cdots$	123	Vilenius et al. (2014)	2454300.0	0.002
(160091) 2000 OL$_{67}$	$\cdots$	$\cdots$	37	assumed	2457000.0	0.011
(160256) 2002 PD$_{149}$	$\cdots$	$\cdots$	93	assumed	2457000.0	0.007
(174567) Varda-Ilmarë	5.91	Thirouin et al. (2014)	370	Vilenius et al. (2014)	2455300.0	0.005
(225088) Gonggong-Xiangliu	44.81	Pál et al. (2016)	767.5	Pál et al. (2016)	2457000.0	0.006
(229762) G!kún‖'hòmdímà-G!ò'é !hú	11.05	Thirouin et al. (2014)	295	Schindler et al. (2017)	2457000.0	0.004
(275809) 2001 QY$_{297}$	11.68	Thirouin et al. (2012)	84.5	Vilenius et al. (2014)	2454200.0	0.002
(341520) Mors-Somnus	9.28	Thirouin et al. (2014)	51	Sheppard et al. (2012)	2454300.0	0.030
(364171) 2006 JZ$_{81}$	$\cdots$	$\cdots$	61	Parker et al. (2011)	2453400.0	0.026
(385446) Manwë-Thorondor	11.88	Rabinowitz et al. (2019)	80	Grundy et al. (2014)	2454400.0	0.004
(469705) ǂKágára-!Hãunu	9.65	Benecchi & Sheppard (2013)	69	Vilenius et al. (2012)	2455600.0	0.005
(508788) 2000 CQ$_{114}$	$\cdots$	$\cdots$	66	assumed	2454100.0	0.003
(508869) 2002 VT$_{130}$	$\cdots$	$\cdots$	125.5	Mommert (2013)	2455900.0	0.002
(524366) 2001 XR$_{254}$	$\cdots$	$\cdots$	85.5	Vilenius et al. (2014)	2454300.0	0.002
(524531) 2002 XH$_{91}$	$\cdots$	$\cdots$	149	assumed	2457000.0	0.005
(525462) 2005 EO$_{304}$	$\cdots$	$\cdots$	152	Parker et al. (2011)	2453400.0	0.042
(612095) 1999 OJ$_4$	$\cdots$	$\cdots$	37.5	Grundy et al. (2009)	2454000.0	0.003
(612147) 2000 CF$_{105}$	$\cdots$	$\cdots$	32	Parker et al. (2011)	2454881.0	0.024
(612176) 2000 QL$_{251}$	$\cdots$	$\cdots$	74	Grundy et al. (2009)	2454200.0	0.003
(612239) 2001 QC$_{298}$	7.78	Thirouin et al. (2014)	117.5	Vilenius et al. (2014)	2452000.0	0.002
(612687) 2003 UN$_{284}$	$\cdots$	$\cdots$	62	Parker et al. (2011)	2452963.8	0.072
1998 WW$_{31}$	$\cdots$	$\cdots$	74	Veillet et al. (2002)	2452300.5	0.006
1999 RT$_{214}$	$\cdots$	$\cdots$	50	assumed	2457000.0	0.005
2001 QW$_{322}$	$\cdots$	$\cdots$	64	Parker et al. (2011)	2452000.0	0.076
2003 QY$_{90}$	3.4	Kern (2006)	40.5	Grundy et al. (2011)	2453500.0	0.006
2003 TJ$_{58}$	$\cdots$	$\cdots$	32.5	Grundy et al. (2009)	2454300.0	0.003
2004 PB$_{108}$	$\cdots$	$\cdots$	121.5	Grundy et al. (2011)	2454200.0	0.003
2006 BR$_{284}$	$\cdots$	$\cdots$	45	Parker et al. (2011)	2455000.0	0.031
2006 CH$_{69}$	$\cdots$	$\cdots$	50	Parker et al. (2011)	2455000.0	0.034

Note—The list of 45 Trans-Neptunian Binaries which we study with both Keplerian and non-Keplerian models. This includes all TNBs (except two unusual cases) that had known orbits or mirror-ambiguous orbits. Rotation periods and primary radii used in our non-Keplerian fits (and their references) are also listed. The epoch of the fit is also listed; this is the time at which the orbital element parameters are set in non-Keplerian fits (which have time-varying orbital elements). Uncertainty refers to the typical uncertainty in the relative astrometry used to produce orbit fits.

ters by drawing random, normally-distributed samples from the orbital solutions listed in the Grundy database, although we inflated uncertainties to allow for a broader search of parameter space. For systems with mirror ambiguous orbits, we ran two different fits to explore both orbital solutions.

We set uninformative priors for these fits, using uniform distributions for each parameter (see Ragozzine et al. for more details). Similar to other orbit fitting procedures, we compared our model to the relative astrometry using the χ^2 statistic (c.f. Grundy et al. 2019). After completion of the runs, we checked for convergence of the MCMC chains based on trace plots and the smoothness of the marginal and joint posterior distributions of each parameter. In a few cases where we could not clearly confirm the MCMC chains were converged, we reran the fits with more burn in and sampling steps, until we were confident the chains were converged.

2.3. *Non-Keplerian Orbital Fits*

Using `MultiMoon`'s non-Keplerian orbit fitter, we completed non-Keplerian fits to all 45 TNB systems. Although `MultiMoon` is capable of fitting the gravitational harmonics of all bodies in TNBs system, for this analysis, we only fit the J_2 gravitational harmonic of the system's primary with an assumed size and rotation rate. This greatly reduces the complexity of the model as only 3 parameters are added (J_2 and two spin pole direction angles) rather than 14 (ellipsoid polar axis length c, J_2, C_{22}, two spin pole direction angles, a spin longitude angle, and a rotation rate, all for both objects). Since non-Keplerian effects can break the usual mass degeneracy in Keplerian fits, we also allow both masses to float, adding one more parameter. In many TNB systems, the dominant source of non-Keplerian effects should come from the J_2 of the primary, but even if this is not the case, using a single J_2 is a good approximation to the modeling the system's "total" J_2, as measured by the orbital precession. It also provides a way to model non-Keplerian orbital precession whatever its source, as discussed above and in Ragozzine et al. (2023). While neglecting C_{22} can provide worse fits, this is only the case when a TNB is near a low-order spin orbit resonance. Given that most TNOs rotate in ~10s of hours and TNB orbit periods are $\gtrsim$10 days, low-order spin-orbit resonances among our sample will be extremely rare. The only known TNB in our sample which is at spin-orbit resonance is Sila-Nunam. We discuss the consequence of neglecting C_{22} for the Sila-Nunam system in Section 4. As our goal is identifying objects with the most statistically significant non-Keplerian effects, even if our assumptions do not hold, the improvement in or-

bital fit from the wrong model would still indicate the need for higher fidelity and more advanced fits.

Given these assumptions, our non-Keplerian orbital model has 11 free parameters, the six Keplerian orbital elements at a given epoch, the masses of the individual system components (M_1 and M_2), two angles describing the rotation pole of the primary at epoch (i_{sp} and Ω_{sp}, which are Euler angle representations of the spin pole), and $\ln\left(J_2 R^2\right)$. We opt to use the ln of $J_2 R^2$ to enable easier exploration over many orders of magnitude. Additionally, we use the combination $J_2 R^2$ instead of just J_2 so results can be interpreted with a variety of shape models.

In our MCMC ensembles, we used 100 walkers running for 26000 total steps, split between 15000 burn in steps, pruning of poorly performing walkers, 1000 post-pruning burn in steps, and 10000 sampling steps. We set integration tolerance value at 10^{-10} for all runs. This was chosen to balance integration quality/accuracy and computational expense. In all our testing, this tolerance level was found to be sufficient for our needs.

We initialized walker positions for mass and orbital elements identically to the Keplerian fits. In addition, we initialized walker positions for $\log\left(J_2 R^2\right)$ by drawing random samples from a normal distribution centered at $\log\left(10R\right)$, where R is the object's estimated radius, a rough approximation of typical J_2 values due to non-spherical shapes over a large size range. Lastly, we initialized walker positions for the spin pole direction to be generally aligned with the orbit, within ~10-30° of perfectly aligned. For other required `MultiMoon` inputs (approximate radius and rotation period), we used values previously published in the literature (see Section 2.1 for more details). For objects with no known rotation period, we used a default value of 10 hours (similar to those found in Thirouin et al. 2014). For the few TNBs that did not have estimated radii published in the literature, we assumed a value based on an assumed albedo and the system's absolute magnitude. Information on all TNBs considered in our analysis, along with the input for approximate radius and rotation period, is located in Table 1. Our testing indicates that changing these assumed values does not substantially affect the results of our fits. Like the Keplerian orbit fits, mirror ambiguous TNBs had two orbit fits run to explore both orbital solutions.

Our priors on each parameter were uniform with the goal of being uninformative, except in a few cases. Firstly, we enforced $a(1 - e) > q_{min}$, where q_{min} was chosen to be equal to a factor of a few times the primary radii. This helped to reduce the chances of unphysical close encounters that were occasionally explored

in extreme non-Keplerian integrations. We also force $M_2 < M_1$. This practice reduces the effects of degeneracies between mass and J_2.

Finally, $\ln\left(J_2 R^2\right) < 15$ was enforced to limit exploration in J_2 space. At large values of $J_2 R^2$, some TNB systems can become unstable, placing this constraint prevents exploration of these unstable models. While this may prevent exploration of relevant parameter space for some systems, we found that this prior appropriately balances stability and our goal of broad exploration. In a small number cases, the prior had to be further reduced after confirming that large values of J_2 caused unphysical models[5]. A uniform prior in $\ln\left(J_2 R^2\right)$ is not meant to signify our actual prior knowledge of the J_2 distribution of TNBs, but rather to encourage exploration of this new parameter. We adopt as meaningful only those fits where the likelihood (calculated based on χ^2 as with Keplerian modeling) of a non-Keplerian fit strongly prefers a particular value of J_2 and thus is relatively independent of the prior.

As our goal of this project was to identify systems with the most statistically significant non-Keplerian effects, we did not aim for full convergence of our MCMC chains. Rather, we focused on achieving the best non-Keplerian fit possible in a fixed number of model evaluations. While this results in unconverged fits – so that the full posterior probability distributions are not expected to be completely accurate – the unconverged chains can still be informative, especially in light of our goal of identifying targets for future investigations. In essence, our runs are set up to determine which TNBs have the most easily detectable non-Keplerian effects. We refer to these potentially unconverged fits as "exploratory" and consider them valuable at the full catalog level of this analysis.

These fits and their implications were studied individually in detail by various co-authors as part of Brigham Young University's Physics 227 ("Solar System Astronomy") Class Project.

2.4. *Non-Keplerian Orbital Fits for Borasisi-Pabu*

To show that unconverged fits described above are able to identify targets worthy for future investigation, we completed a full non-Keplerian orbit analysis of the Borasisi-Pabu system, one of the more promising targets identified in our exploratory fits, as a proof-of-concept. In this fit, we relaxed several of the assumptions made in the non-Keplerian exploratory fits, most notably our assumptions regarding the C_{22} of the primary. Our non-

---

[5] These unphysical models could sometimes cause `MultiMoon` to crash unexpectedly, this has since been fixed.

Keplerian orbital model has 13 parameters, six Keplerian orbital elements at epoch, the masses of both system components, the direction of the primary's rotation pole at epoch, the $J_2 R^2$ and $C_{22} R^2$ of the primary, and the longitude of the primary's prolate axis at epoch (ω_{sp}). For Borasisi's rotation period we used 6.4 hours (Kern 2006) and a radius of 63 km (Vilenius et al. 2014). After our analysis was completed, Kecskeméthy et al. (2023) found a different light curve period for the combined system, we discuss the minor implications of this in Section 5.

For this full orbit fit, we ran `MultiMoon` with 980 walkers for 23500 steps, split between 15000 burn in steps, 1000 post-pruning burn in steps, and 7500 sampling steps. Integration tolerance was set to 10^{-11} to produce the best quality of fits possible, with less regard for optimizing computational expense than the previous round of fits. Initial walker positions were drawn based on preliminary orbital fits and the results of our exploratory fits, but otherwise the fitting process was effectively identical to that above. We confirmed convergence of the MCMC chain by inspection of trace plots and marginal and joint posterior distributions of each parameter.

Our quadrupolar approximation cannot distinguish between models rotated by 180 degrees (e.g., it cannot distinguish the North pole from the South pole), resulting in a two-fold degeneracy. Since the degeneracy is fairly well-understood, we decide to fit only the prograde rotation solution, where the rotation axis is required to be inclined $< 90°$ relative to the binary's mutual orbit plane.

2.5. *Evaluating Fit Quality*

To ensure the quality of all of our fits (both Keplerian and non-Keplerian), we have thoroughly evaluated each fit using a variety of statistical techniques. Most simply, and easily output from `MultiMoon` is the calculation of reduced χ^2, which is equivalent to the best fit parameter set's χ^2 per degree of freedom. For almost all of our fits, reduced χ^2 was $\lesssim 1$, indicating good quality fits. For 8 of our Keplerian fits, however, we found statistically significant cases of elevated reduced χ^2. Several of these systems have been previously identified as inconsistent with Keplerian orbits (e.g. Grundy et al. 2019). These systems all had significant, or nearly significant, non-Keplerian effects detected (see Section 4).

Another way we can analyze the quality of our orbit fits is to calculate the root-mean-square (RMS) residual of the fit. For our fits, we find that most of our fits have RMS residuals $\lesssim 15$ milliarcseconds, indicating an excellent fit to the data. Compared with the typical un-

certainties in the astrometry we fit to (see Table 1), we find that our fits are very robust. A few systems have much larger RMS residuals, but this is caused by large uncertainties in the data. As discussed in Section 2.1, the ultra-wide TNBs tend to have many observations taken with relatively imprecise ground-based observatories, which can result in large RMS residuals. Combined RMS residuals (with each dimension added in quadrature) are reported in all tables below.

Like RMS residuals, we also looked at the weighted RMS residuals. These residuals are essentially in units of observational error bars (as shown in Table 1). We find that all of our fits have weighted RMS residuals < 1.4, with most being < 1. This confirms the quality of our fits.

We also closely examined the residual plots for each fit (see Figures 2 and 7 for examples). These plots show the normalized residuals (residual divided by measurement uncertainty) and were examined to ensure no systematic trends were visible in the residuals (e.g., uncentered residuals, significantly larger residuals in one dimension, correlations among subsets of the data taken with different facilities, etc.). We found no serious issues with any of our fits in individual fits, and also found no problems at the ensemble level. These normalized residuals are available for both our Keplerian and non-Keplerian fits publicly available on Zenodo.

Another sign of the quality of our fits is their close match to orbit fits published in the literature. In Section 3, we show that our orbit fits closely reproduce fits in the literature. This close agreement is strong evidence that our orbit fits are of high quality.

3. KEPLERIAN FITS

The results of our Keplerian fits are contained in Table A1. It contains information regarding the posterior distributions of the mass and orbital elements of each TNB (median values with 1σ confidence intervals). In addition to values from the marginal (single variable) posterior distributions (as seen in the table), the full posterior distribution can be displayed as a corner plot. As an example, we show the corner plot of the Keplerian posterior for (66652) Borasisi-Pabu in Figure 1 and a residual plot in Fgiure 2. The results for all 45 TNBs (including MCMC chains, diagnostic plots, statistical information, etc.) are publicly available at https://doi.org/10.5281/zenodo.7636946.

For all mirror ambiguous TNBs, two orbit solutions are shown in Table A1, with the exception of 2002 WK_{183} and 2000 OJ_{67}. For both of these objects, despite attempting two orbit fits for the separate solutions, the mirror ambiguous solutions are so close together that the posteriors of each solution significantly overlap. Separating the two distributions in a statistically rigorous way is difficult due to the blended nature of the posterior. Note that the *emcee* algorithm at the heart of MultiMoon is not optimized for rigorous exploration of multi-modal posterior distributions. As such, we report the statistics of the blended distribution and urge caution when using the orbit fits for these objects.

As a test of MultiMoon's performance in completing Keplerian fits, the posterior distributions of the ensemble of fits can be compared to the best fits from the Grundy database. We calculated the z-score of every Grundy best fit for every parameter and every object, using our posterior distribution as the reference distribution. The distributions of these scores for each parameter is shown in Figure 3 using kernel density estimates. The z-score distributions clearly show that the Grundy best fits are consistent with the MultiMoon posteriors. Technically, since we are analyzing the same data with the same model, the agreement should be much better than drawing parameters from a random distribution. While not a perfect match, the fact that the vast majority of parameters are within 1-σ means that any systematic errors are minimally important compared to the statistical errors. We note that a similar analysis of an ensemble of Keplerian TNB orbit fits also found consistency with the Grundy results (Emelyanov & Drozdov 2020), further supporting that these results are robust to the analysis method.

Likewise, when comparing the Grundy database parameter uncertainties (which are determined via Monte Carlo techniques) to the MultiMoon Keplerian posterior distributions, we find excellent agreement. For all parameters (except argument of periapsis ω and mean anomaly $\mathcal{M}$), the error bars are similarly sized for all the TNBs. For ω and $\mathcal{M}$, our model is differently parameterized, where the Grundy database uses longitude of periapse (ϖ) and longitude at epoch (ϵ). This slightly different parameterization obscures a like-to-like comparison.

For those interested in precise understanding of the uncertainties in Keplerian fit parameters, our reporting of full posteriors provides an improvement to the state-of-the-art which approximates parameters as having a mean value and uncertainty. Posterior samples are also particularly useful for scheduling of follow-up observations. Each sample in the chain provides a predicted position of the binary components at any given time. Taken together, the ensemble of samples (or a sufficiently large subset of the ensemble) then provides a probability distribution for the predicted positions of the binary components, as further discussed below.
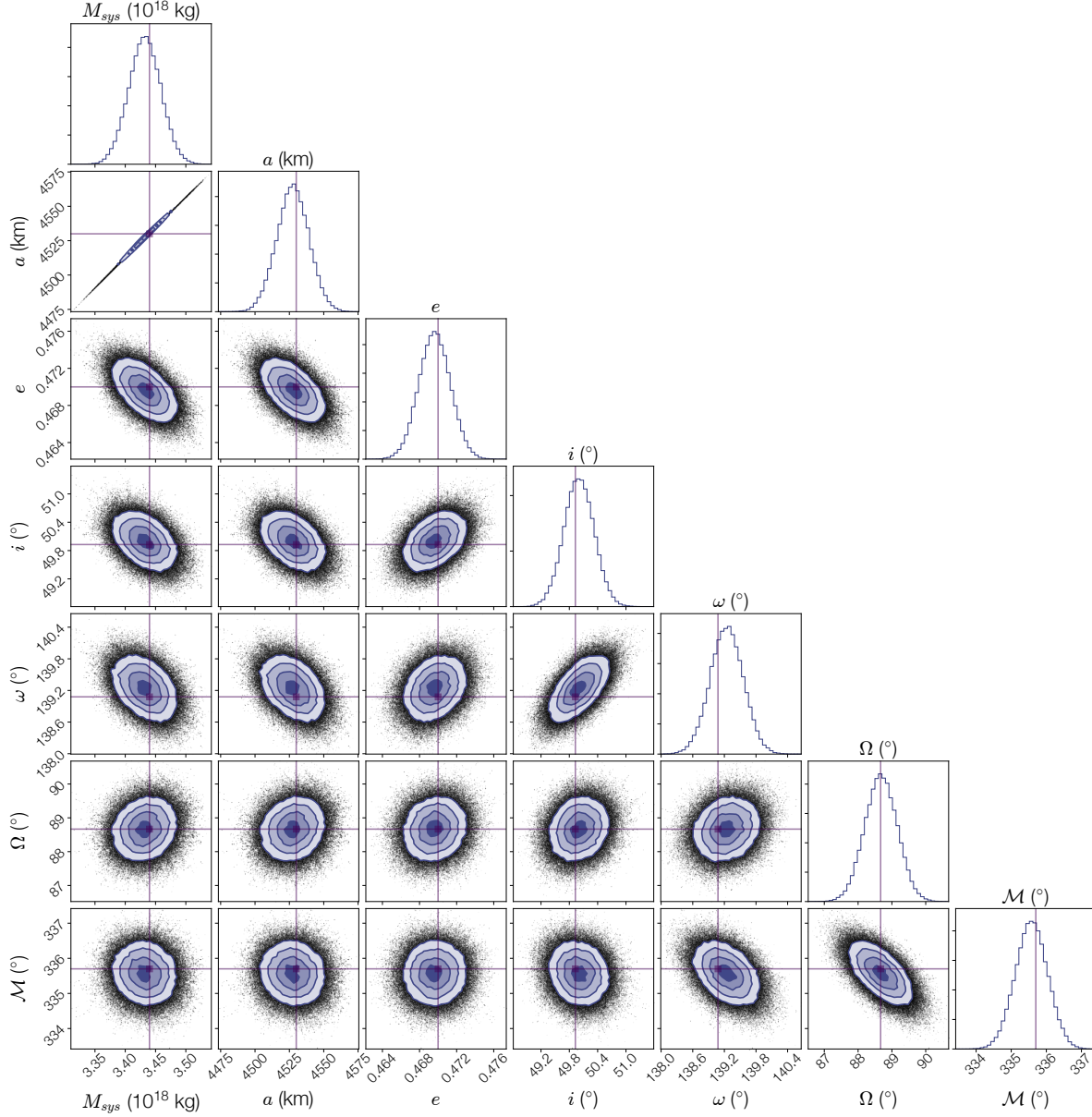
Figure 1. Corner plot for the Borasisi-Pabu Keplerian orbit fit. Along the tops of the columns are the marginal posterior distribution for each parameter; in the case of a Gaussian distribution, this can be used to determine the best-fit and uncertainty. The contour plots show the joint posterior distribution between every pair of parameters. For example, the system-mass semi-major axis degeneracy is seen in the top left which is a result of measurement of only the orbital period and Newton's Version of Kepler's Third Law. Contours show the 1, 2, and 3σ levels of each joint posterior distribution. The horizontal and vertical lines show the orbit solution publicly available in the Grundy database. Of particular interest is the strong agreement between the Grundy solution (horizontal and vertical lines) and the solution derived by `MultiMoon`. The best fit in the `MultiMoon` fit corresponded to a χ^2 of ~21. RMS residuals are 2 milliarcseconds in both longitude and latitude. All angles are relative to the J2000 ecliptic plane on JD 2451900.0 (2000 December 21 12:00 UT).
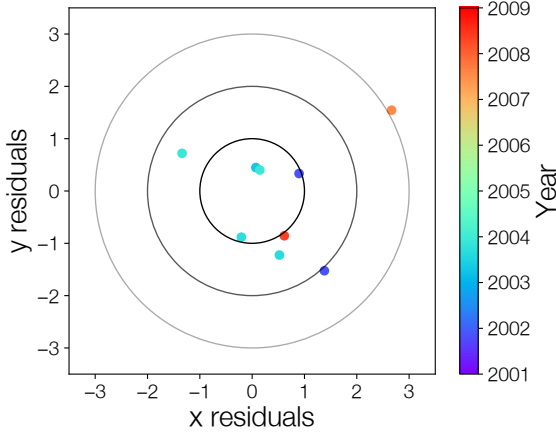
Figure 2. Residual plot for the Borasisi-Pabu Keplerian orbit fit. Plotted are the normalized residuals (residual divided by measurement uncertainty) in longitude (x) and latitude (y) with color corresponding to observation date. The three large circles correspond to 1, 2, and 3 σ error contours. The best fit in the `MultiMoon` fit corresponded to a χ^2 of $\sim$21. RMS residuals are 2 milliarcseconds in both longitude and latitude. The radius of a typical 1σ error contour is $\sim$2 milliarcseconds, although values ranged between 0.9 and 5 milliarcseconds.
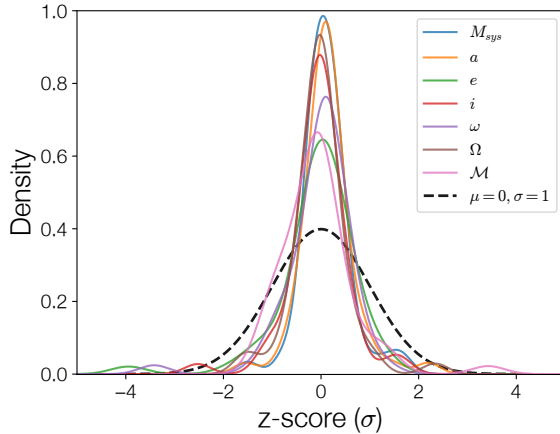
Figure 3. Kernel density estimates (KDEs) for the distributions of z-scores of Grundy best fits (when compared to the `MultiMoon` posteriors) for each fitted parameter. The dashed black line shows a normal distribution with a width of 1 as a comparison. It is clear that for all fitted parameters, the Grundy best fits are well within our posterior distributions, with the majority being $< 1\sigma$ away from our posteriors. `MultiMoon`'s Keplerian fitting algorithm produces essentially identical results to those previously published in the literature.

The results for the Keplerian model with constant photocenter-barycenter offsets are discussed in Section A. We find that the offsets presented are attributable to overfitting. We also find that they do not significantly affect the Keplerian results, except for possibly adjusting the eccentricity.

The agreement of our Keplerian outputs with previously published fits confirms that `MultiMoon` can effectively fit TNB orbits, despite the different parameterization and methods used. This validates `MultiMoon`'s fitting procedures and techniques, lending confidence in our non-Keplerian fits presented in Sections 4 and 5.

4. NON-KEPLERIAN FITS

Aligned with our goal of identifying candidates for future non-Keplerian analysis, we present the non-Keplerian best fit model for each TNB in Table A2. The best fits in the table do not have uncertainties attached to them because our MCMC chains are not converged. In an MCMC framework, uncertainties are drawn from the 16th and 84th percentiles of the output chains. Without convergence, the resulting 16th and 84th percentiles are extremely unreliable estimations of the true uncertainties. Despite this, we still believe that the best fits are still useful for showing that non-Keplerian effects are detectable. To evaluate the detectability of non-Keplerian effects, we can find the statistical significance of each non-Keplerian fit by calculating the likelihood ratio between the Keplerian and non-Keplerian fits. The likelihood ratio test can compare the goodness-of-fit of two nested physical models. In our case, the Keplerian model is a subset of a non-Keplerian model where $J_2 = 0$. Under the likelihood ratio test if the null hypothesis (no currently detectable non-Keplerian effects) is supported by the data, the likelihood ratio, $\frac{\mathcal{L}_K}{\mathcal{L}_{NK}} \approx 1$, where $\mathcal{L}_K$ and $\mathcal{L}_{NK}$ are the Keplerian and non-Keplerian likelihoods, respectively. If the null hypothesis can be rejected (non-Keplerian effects are currently detectable) $\frac{\mathcal{L}_K}{\mathcal{L}_{NK}} \ll 1$.

Traditionally, some threshold is chosen at which the improvement in fit is deemed significant and the null hypothesis is formally rejected. However, the fits presented here are exploratory in nature and may not have reached the global maximum likelihood, as evidenced by our results in Section 5. Further analysis would only strengthen the significance of non-Keplerian results, as these fits act as an lower limit on the improvement of the fit. We choose to give special attention to cases where $\frac{\mathcal{L}_K}{\mathcal{L}_{NK}} < 0.1$ which are bolded in Table A2. Inspection of the posterior distributions (though not necessarily converged) also show that in these systems, $J_2 R^2 = 0$ is excluded at high confidence. The improvement in the

likelihood is also significant compared to the number of additional parameters.

We do find that change in RMS residuals between our Keplerian and non-Keplerian fits are not strongly correlated with improvement in fit as measured by $\frac{\mathcal{L}_K}{\mathcal{L}_{NK}}$. Some exploration of possible reasons as to why this is the case showed that the result is due to heterogeneous uncertainties in the data. When instead using normalized/weighted residuals (as in Figure 2), we see the expected correlation between change in fit quality and change in weighted RMS residuals.

The 8 TNBs satisfying this threshold have non-Keplerian effects that are currently detectable. In this section, we will first discuss population-level trends identified in our fits, and then individually discuss the 8 TNBs we identify as prime targets for non-Keplerian analysis.

In addition to Table A2, we display the ensemble of non-Keplerian fits in Figure 4 where we plot the best fit J_2 value against the likelihood-ratio statistic. In this figure, we assume a triaxial shape model for easy comparison between our fits and to the literature. From this we can identify several broad trends among our best fits. TNBs with large primaries are more likely to have smaller best fit J_2 values than small primaries, in line with theoretical predictions and observations of small bodies across the solar system. Another striking trends is that larger objects are more likely to have significant non-Keplerian effects, with the three most significant detections (Salacia, Orcus, and Gonggong) being among the largest TNBs in our sample (which excludes Pluto, Eris, Haumea, and Makemake). This is likely because TNBs with large primaries tend to have shorter orbital periods (and thus stronger and faster non-Keplerian effects) in addition to having more high quality data.

Another interesting discovery is a group of objects with significant non-Keplerian detections at relatively high J_2 (Borasisi, Altjira, 1999 RT_{214}). The high J_2 indicated by our exploratory fits potentially hint that one of the system components may be a contact binary. While this is an unusual configuration, among asteroid binaries several primaries have been found with extreme values for J_2, perhaps most notably Kleopatra, with $J_2 = 0.765$ (Brož et al. 2021). Their prevalence in our findings, however, may be attributable to selection bias. Since these systems have large J_2 values, their non-Keplerian effects are far easier to detect, when compared to objects with similar data quality and quantity, and observational baseline. As such, these systems may not be as common as would be suggested by our findings.

Similar to a possible discovery of contact binaries, our results show three TNBs with unresolved binary-like J_2 values (2005 EO_{304}, Teharonhiawako ("QT297"), and 2006 BR_{284}), although none of the fits for these bodies cross our strict significance threshold. As discussed above, hierarchical triple systems may be sensitive tracers of planetesimal formation in the early solar system, making a discovery of additional hierarchical triple systems an important goal. In fact, Nesvorný et al. (2021) conclude that Lempo-like triple systems "should be found in the Kuiper Belt when observations reach the threshold sensitivity." More observations of these bodies, and subsequent orbit reanalysis, are required to find if these systems can be confirmed as having detectable non-Keplerian effects. Preliminary investigations suggest that these hierarchical triples are not resolvable with imaging.

Another possible explanation for the large J_2 values found here is that these TNBs are strongly affected by the Sun's gravitational influence, with this influence manifesting as a large measured J_2. All three of these TNBs are ultra-wide binaries, a class of TNBs with extremely large separation. Ultra-wides are most affected by the Solar tide due to their extremely long orbital periods. Future modeling efforts should aim to include the effects of the Solar tide to more fully model all gravitational dynamics at play.

Our ensemble of exploratory fits is also able to identify systematic errors which may stem from the use of Keplerian fits in a variety of past analyses. To do this, it is most useful to compare our non-Keplerian best fits with the full Keplerian posteriors discussed in Section 3. Using the same methods as the comparisons to the Grundy best fits, we compare our fits in Figure 4, using our Keplerian posteriors as the reference distribution. As can be seen, our non-Keplerian best fits are somewhat different to our Keplerian posteriors, especially for ω and Ω. This is expected for non-Keplerian analyses since the addition of J_2 shape effects allows for precession of these orbital angles. The absolute difference in these angles (at epoch), which can be several standard deviations from the Keplerian fit, are usually only a few degrees.

Notably, the masses, semi-major axes, and eccentricities found in our non-Keplerian best fits are consistent with the Keplerian posteriors. This shows that systematic errors in orbital orientations can occur when assuming Keplerian orbits, but that masses, semi-major axes, periods, eccentricities, and inclinations are not significantly affected. Thankfully, the large number of analyses that rely on Keplerian fits are unaffected by systematic errors from non-Keplerian fits.

4.1. *Identified Targets*
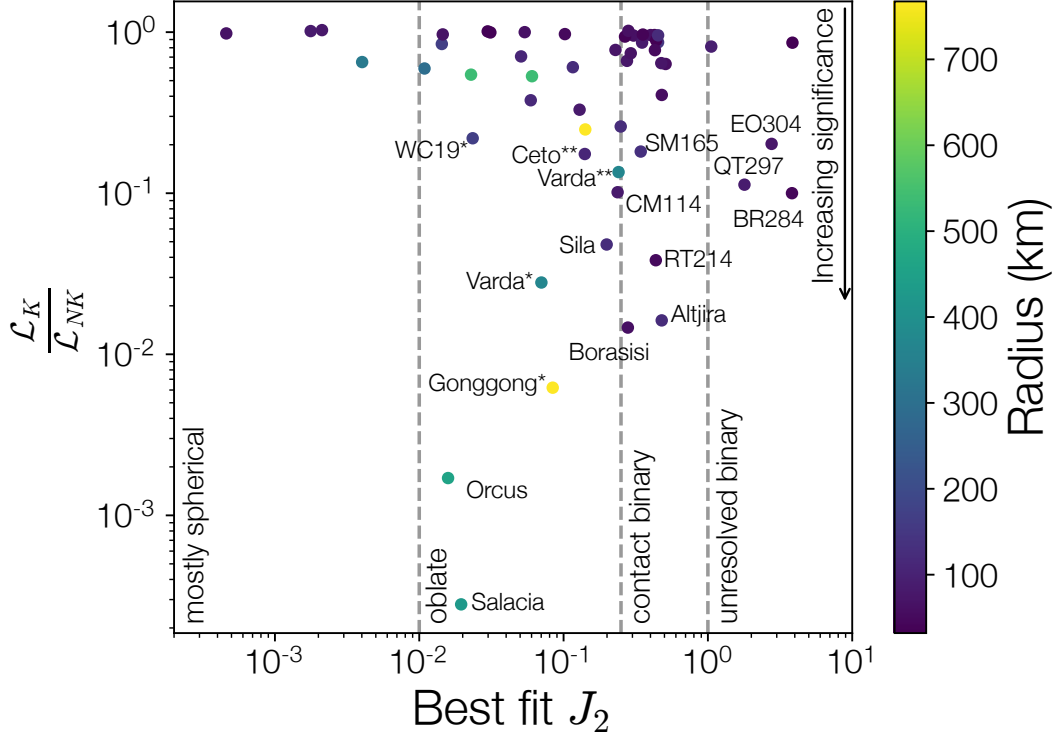
Figure 4. Improvements in fit quality by adopting a non-Keplerian model. The best fit J_2 presented here is found by assuming a triaxial shape and dividing our measured J_2R^2 by the resulting body's volumetric radius squared. The ratio $\frac{\mathcal{L}_K}{\mathcal{L}_{NK}}$ compares the Keplerian models presented in Section 3 to the best exploratory fit presented in this section. If the likelihood ratio is $\ll 1$, the null hypothesis (no detectable non-Keplerian effects) could be rejected, and non-Keplerian effects are indeed detected. In general, throughout this paper, we adopt a significance threshold of $\frac{\mathcal{L}_K}{\mathcal{L}_{NK}} < 0.1$ to indicate significant detections. We have labeled all of the significant detections of non-Keplerian effects, as well as several systems with almost significant detections. Asterisks in labels indicate either a prograde (*) or retrograde (**) orbital solution for mirror ambiguous TNBs. Color corresponds to the radius of the TNB's primary. We find that many TNBs have a significant detection of non-Keplerian effects, with many near significant detections as well. We also find a wide range of acceptable J_2 values, ranging from oblate spheroids to unresolved binaries. Future work and observations should focus on confirming the significant detections we find and getting more observational data to confirm nearly significant detections.

Here, we discuss in turn each of the eight TNBs identified as having detectable non-Keplerian effects.

4.1.1. *(120347) Salacia-Actaea*

Salacia-Actaea is one of the largest and most massive TNBs in our sample. Our fits used 14 individual observations over a 10 year time span. Detection of non-Keplerian effects is expected as previous analyses showed that observations were 3.7σ inconsistent with a Keplerian orbit (Grundy et al. 2019).

Our analysis had a best fit $J_2 = 0.0195$, which corresponds to a slightly oblate spheroid, but fits with similar likelihoods (although slightly worse) were different by a factor of a few. This large range of possible values for J_2 is expected for systems where only apsidal or nodal precession is detected. In this case, Salacia's J_2 is de-

generate with its obliquity with respect to the mutual orbit. Since Salacia-Actaea's mutual orbit is nearly circular ($e = 0.0062^{+0.0031}_{-0.0027}$, Table A1) the non-Keplerian effects present in the system are likely to be nodal precession, since apsidal precession is difficult to detect at low e. Detection of nodal precession implies that Salacia's rotation pole is misaligned with the binary's mutual orbit, but the degree of misalignment is not possible to determine without further analysis.

Future observations of the Salacia-Actaea system may be able to detect apsidal precession, allowing for a more full determination of the system's properties. Additionally, constraints provided by Salacia's low amplitude light curve (Thirouin et al. 2014) and future occultations may aid in this effort.
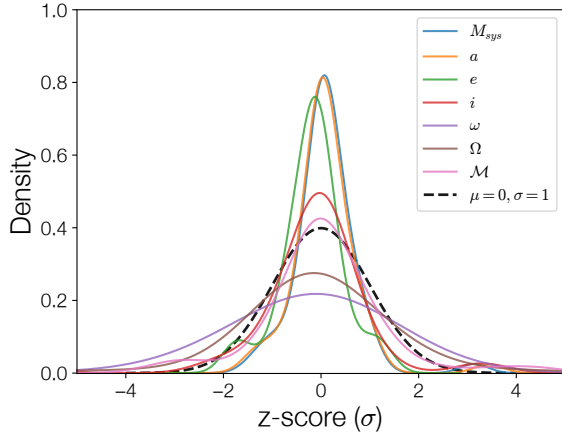
Figure 5. Kernel density estimates in the style of Figure 3. In this figure, we compare the non-Keplerian best fits found in our exploratory fits to the Keplerian posteriors presented in Section 3. We find that significant deviations are present in the argument of periapsis (ω) and longitude of ascending node (Ω) when assuming a non-Keplerian model. This is expected since this model allows for precession of these two angles. The distributions are still centered at zero presumably because we are comparing the non-Keplerian angles at an epoch typically near the middle of the observations and because many systems show insignificant non-Keplerian effects. Notably, however, the system mass, semi-major axis, eccentricity, and inclination are still consistent with Keplerian fits, implying that systematic errors due to non-Keplerian effects are small in most previous analyses.

4.1.2. *(90482) Orcus-Vanth*

Orcus-Vanth is another large, high mass TNB. Our fits used 12 individual observations taken over an almost 10 years. Like Salacia-Actaea, past analyses showed Orcus-Vanth was 2.2σ inconsistent with a Keplerian orbit (Grundy et al. 2019), making detection of non-Keplerian effects unsurprising.

Our analysis had a best fit $J_2 = 0.016$, corresponding to a slightly oblate spheroid. Similar to Salacia-Actaea, due to Orcus-Vanth's nearly circular orbit only nodal precession was detected, introducing large uncertainties on our J_2 and obliquity measurements.

In the future, observations of Orcus-Vanth may help understand the system better, however, our preliminary results show that detection of apsidal precession may be an order of magnitude more difficult than for Salacia-Actaea. Understanding the shape of Orcus (or Vanth) will probably require additional multi-chord observations of stellar occultations, similar to the 2017 occultation of Vanth (Sickafoose et al. 2019).

4.1.3. *(225088) Gonggong-Xiangliu*

Gonggong-Xiangliu, the most massive binary in our sample, is the most surprising target with detection of non-Keplerian shape effects. Our fits only used 6 individual observations over about 8 years. The dearth of data, especially when compared to other TNBs, is due to the discovery of the moon in 2016 (Kiss et al. 2017), although subsequent reanalysis found the moon in 2009 and 2010 HST images. Our detection is only robust when considering the prograde orbit solution.

Our analysis had a best fit of $J_2 = 0.084$, corresponding to a fairly oblate spheroid. The high J_2 we find is quite unexpected, and may possibly contradict light curve measurements (Pál et al. 2016). In our analysis, we believe we have detected both apsidal and nodal precession, allowing us to place constraints on Gonggong's obliquity. Our best fit obliquity is $116.4°$, however, our fits cannot distinguish between north and south pole. By folding the obliquities of our best fit solutions (the best fit and those with similar likelihoods) we find obliquities between $55°$ and $65°$ are favored. The large obliquity is surprising, but the binary's mutual orbit is also quite eccentric ($e = 0.2852^{+0.0086}_{-0.0079}$), possibly implying a complicated history of unusual tidal pumping (Kiss et al. 2019; Arakawa et al. 2021). We note that Gonggong's density has significant uncertainty that can be resolved when the obliquity of the satellite is clearly detected (Kiss et al. 2019), making Gonggong-Xiangliu an extremely promising observational target.

Based on the small dataset, another possible explanation for this detection is overfitting by our model. With small amounts of data, model fitting can become more susceptible to overfitting. In general, 5 or more observations are required to fit a Keplerian orbit (Grundy et al. 2008), so it seems suspicious that we find such high confidence detections of non-Keplerian effects, especially with no previously detected deviation from a Keplerian orbits (like Salacia and Orcus). As such, we do not place much confidence in this detection and consider the detection potentially spurious.

To better understand Gonggong-Xiangliu's unexpected eccentricity and obliquity, resolve the mirror ambiguity, and/or understand issues with overfitting, additional observations need to be taken of this interesting system. The large difference in brightness between Gonggong and Xiangliu make these observations difficult without using the most advanced telescopes (e.g., HST, JWST, or possibly Keck).

4.1.4. *(66652) Borasisi-Pabu*

Borasisi-Pabu, a small near-equal size binary in the Cold Classical Kuiper belt, was fit using 9 observations taken over about 8 years. No previous indications of

poorly fitting Keplerian orbits have been reported in the literature, but our Keplerian analysis, which was consistent with past analyses, showed a Keplerian fit with a reduced χ^2 of 1.9, indicating a somewhat poor fit to the data.

We find a best fit $J_2 = 0.279$, consistent with an extremely elongated object, possibly similar to a contact binary. We also found an obliquity of $\sim 50°$ for Borasisi, after detecting both apsidal and nodal precession. For Borasisi, the detectability of apsidal precession was enhanced by the mutual orbit's large eccentricity ($e = 0.4696^{+0.0017}_{-0.0017}$).

We discuss Borasisi-Pabu in detail in Section 5 and present fully converged, high quality non-Keplerian fits.

4.1.5. *(148780) Altjira*

Altjira (and its unnamed secondary), a small equal-size binary just outside the Cold Classical belt, was fit with 8 observations taken over about 4 years. No past analysis indicated poor quality Keplerian fits, but our Keplerian analysis indicated a marginally bad fit (reduced χ^2 of 1.4).

Our analysis resulted in a best fit $J_2 = 0.479$, roughly consistent with a contact binary. The measured J_2 may also be caused by an unresolved system component, possibly making this a hierarchical triple system. We are able to constrain Altjira's obliquity to be between $\sim 30°$ and $60°$ by detecting both apsidal and nodal precession.

With $V = 23$ mag, little more is known about this system, with no known light curve or occultation measurements. Any additional constraints on this system will contribute to understanding the configuration of this system.

4.1.6. *(174567) Varda-Ilmarë*

Varda-Ilmarë is a somewhat high mass TNB; however, unlike the other high mass TNBs with detected non-Keplerian motion, the primary-to-secondary brightness ratio is far more equal, putting it in a class that is somewhat intermediate between the low-mass (with near-equal masses) and high-mass (large primary-to-secondary mass ratio) TNBs. Our analysis used 12 observations taken over about 4 years. Previous Keplerian analyses did not indicate a significant deviation from Keplerian motion, but our Keplerian analysis showed that Keplerian orbits were somewhat poor quality fits for both the prograde and retrograde orbital solutions at the $\sim 1\sigma$ level. Like with Gonggong-Xiangliu, our detection of non-Keplerian effects is significant for only the prograde orbital solution, although the retrograde solution almost reaches our significance threshold.

Our fits find a best fit $J_2 = 0.07$, consistent with a significantly flattened body. As with other large TNBs

with near-circular orbits, we have only robustly detected nodal precession, leaving a degeneracy between J_2 and obliquity..

Varda-Ilmarë is somewhat unique in having a mirror ambiguous orbit given the large quantity of high-quality data. This is primarily caused by the system's orbit which is viewed nearly face-on. Understanding Varda's role as a possible transitional system, may enable better understanding of the internal structure and composition of TNOs.

4.1.7. *1999 RT$_{214}$*

1999 RT$_{214}$, a small near-equal size TNB in the Cold Classical belt, was fit using 6 observations taken over about 10 years. Past analysis did not show a significant deviation from a Keplerian orbit, but our Keplerian analysis indicated an extremely poor fit (reduced χ^2 of 3.2), although with so few data points, such a result is possible $\sim 1\%$ of the time. With this amount of data, a detection of non-Keplerian motion is surprising, but the long observational baseline allows a fairly robust detection.

Our best fit analysis for this system gave $J_2 = 0.436$, corresponding to a contact binary-like shape. Another possible explanation is that a system component is an unresolved binary, possibly implying that 1999 RT$_{214}$ is a hierarchical triple. A wide range of permissible obliquities are allowed by our exploratory fits, with a range of $\sim 30-55°$ being most likely. Our fits imply that both nodal and apsidal precession are visible.

Additional observations are needed to confirm our detection and to further characterize this system. These will have to be completed by HST, JWST, or large ground-based observatories since $V = 24$ mag for the system. Combined with new observations, high quality non-Keplerian fits may be able to enable a better understanding of this system.

4.1.8. *(79360) Sila-Nunam*

Sila-Nunam, the largest near-equal mass binary in the Cold Classical belt, was fit using 20 individual observations taken over 11 years. Uniquely, six of those observations are mutual events, where one system component passes in front of the other, from our view on Earth, producing a measurable drop in light. No previous modeling, including our Keplerian fits, hinted that non-Keplerian effects were detectable in this system, although previous measurements of Sila-Nunam's combined light curve showed that one, or both, components were flattened by $\sim 12\%$ (Rabinowitz et al. 2014).

Our fits find a best fit $J_2 = 0.199$, consistent with a considerably flattened body. In this case, since both components are possibly flattened, it is possible that

both bodies contribute significantly to the overall system's J_2. Roughly speaking, a system where both bodies have a $J_2 \sim 0.1$ would match our results. Our exploratory fits cannot confidently determine whether nodal or apsidal precession (or both) are detected with high confidence, especially since the geometry of the system introduces several degeneracies in the model parameters. For example, ω and $\mathcal{M}$ had solutions that were good fits $180°$ away from our best fit. These issues resulted in quality issues in our fits. Future non-Keplerian fits may be helped by introducing priors or reparameterizations which reduce the effects of degeneracy.

In a tidally evolved system where the primary and secondary are locked in a spin-orbit resonance, like Sila-Nunam is thought to be, C_{22} can play a prominant role in the system's dynamics (Proudfoot & Ragozzine 2021). This tidally evolved state is at odds, however, with the small, but potentially non-zero, eccentricity measured in a variety of analyses (Grundy et al. 2012; Benecchi et al. 2014), including both our Keplerian and non-Keplerian fits ($e = 0.0158^{+0.0167}_{-0.0098}$). This may be the result of relatively recent excitation which has yet to be damped out, or may be caused by unusual tidal dynamics.

Another explanation for the improvement in fit is overfitting. Sila-Nunam is unique in its use of mutual event data. Using mutual event data to aid in orbit fitting is unusual, but has been used in previous studies of this system without issue (Benecchi et al. 2014). We do, however, acknowledge that this data may introduce unforeseen systematic errors into our analysis, which may somehow result in better fits with a non-Keplerian model. Additionally, we found that a Keplerian model was a reasonably adequate fit to the data (reduced $\chi^2 \approx 1$), calling into question the need for a more complicated model.

The Sila-Nunam system is a prime target for future non-Keplerian analysis, especially with more complicated models that include the effects of C_{22}. This future analysis should also rigorously test if any systematic effects are introduced by the use of mutual event data and test whether overfitting may effect any resulting non-Keplerian fits. Given the mutual events and large set of photometric data, Sila-Nunam an ideal target for a thorough orbital analysis.

4.2. *Non-Keplerian Fitting of Other TNBs*

While the goal of this work is to identify the targets with the most detectable non-Keplerian shape effects, and considerable work needs to be done to complete converged, high quality fits for these systems, other TNBs should not be ignored. Although the current data is not able to robustly detect non-Keplerian shape effects

in systems not meeting our significance threshold, full non-Keplerian fits can still be used to place upper limits on the presence of those effects. These upper limits may, in some cases, provide valuable constraints on the shapes of TNB components.

To illustrate this, we consider our non-Keplerian fits to the 2002 UX$_{25}$ system. While our analysis only shows a slight improvement with the addition of a J_2 and rotation pole, our fits show a rough upper limit on J_2 of ~ 0.05. While this rough estimate of an upper limit cannot be fully verified without converged non-Keplerian fits, it requires that 2002 UX$_{25}$ must have a remarkably spherical shape. When combined with its unusually small density (0.82 ± 0.11 g cm^{-3}, Brown 2013), 2002 UX25 proves to be an unusual object and is possibly a touchstone for TNO formation (e.g. Bierson & Nimmo 2019). The low density suggests a significant porosity (potentially both macroporosity and microporosity) which seems unusual given its large size (>300 km radius), though central pressures are still relatively small as discussed by Grundy et al. (2019). Additional formation modeling is needed to explain the presence of a small (collisionally-formed?) eccentric satellite around a large nearly-spherical rubble-pile.

4.3. *Future Observations*

Based on our results, we believe that future observations should focus on those TNBs with detectable non-Keplerian effects (those described in the last section) and, possibly more importantly, TNBs that are near our significance threshold. These TNBs show the most promise for future detections of non-Keplerian effects and provide the most efficient route for constraining the shapes of the largest number of objects. As observational baselines are extended, non-Keplerian effects become more detectable and uncertainties on the fits shrink. Observations can also be targeted at certain times when the uncertainty of the predicted position is largest, providing the most constraining observations (see Section 5 for more details).

In addition to high resolution imaging to resolve binary components, other types of observations, like light curves or occultations still provide important, orthogonal channels of information on the shapes and spins of TNBs. The constraints given by these observations are able to be meaningfully used as additional data sources in future more complicated models of TNB orbits. For example, the axial precession of a TNB primary due to back torques from the secondary, may be detectable in certain scenarios, which may enable a direct measurement of the primary-secondary mass ratio. Likewise, precession of the axes of TNO moons may provide in-

formation about the shapes and rotation poles of those moons (as suggested by Hastings et al. 2016).

5. BORASISI-PABU

As a proof-of-concept we have performed detailed non-Keplerian fits to the orbit of Borasisi-Pabu, accounting for non-Keplerian effects due to both J_2 and C_{22}. The marginal posterior distributions for each parameter are displayed in Table 2 and joint posterior distributions are shown as a corner plot in Figure 6. We also show a residual plot in Figure 7.

Using the framework introduced in Section 4, we can assess the statistical significance of our non-Keplerian fit, when compared to the Keplerian fit from Section 3 (see also Table A1 and Figure 1). As before, the Keplerian model we use is a subset of our non-Keplerian model (where J_2 and C_{22} are 0). Using a likelihood-ratio test, we find that $\frac{\mathcal{L}_K}{\mathcal{L}_{NK}} = 8.34 \times 10^{-3}$, giving confidence that the non-Keplerian model is statistically significant. This likelihood ratio statistic is somewhat smaller than that found in our exploratory fits (compare with Table A2). Both Table 2 and Figure 6 show that a Keplerian orbit ($J_2, C_{22} = 0$) for the mutual orbit of Borasisi-Pabu is strongly excluded with a significance $> 3\sigma$, again strongly confirming that a non-Keplerian model is preferred.

To test how robust these results are to our input values (rotation period of Borasisi, c-axes of Borasisi and Pabu, integration tolerance), we also performed many additional non-Keplerian fits with these values substantially changed. These tests produced posteriors that are nearly identical to the one presented here, except when integration tolerance was set to a too high level. These tests showed that the choices we made for input values did not affect the fit presented here, and validate the inputs used in our exploratory fits.

In addition to validating input parameters, we also ran a series of recovery tests on `MultiMoon`. These tests used `MultiMoon` to fit synthetically generated data (with artificially added uncertainties) using the best fit solution in Table 2, allowing us to determine if `MultiMoon` could recover the input parameters. These tests returned similar fits to the one presented in this section, showing similar uncertainties and degeneracies, justifying the use of `MultiMoon` given our current data and mitigating the risk of overfitting for this system.

For most parameters, there is agreement with both our Keplerian solution and the Grundy best fit, at the $\sim 1\sigma$ level, except for Ω, which shows a strong disagreement with Keplerian fits. This is an expected result

of non-Keplerian fitting as the orbital model now allows for precession of the node. Our posterior shows $J_2 = 0.4446^{+0.1192}_{-0.0928}$ implying an extremely non-spherical shape of Borasisi. The spin pole direction is nearly perpendicular to the ecliptic.

Our fits show no preference for a certain value of C_{22}, as can be seen in Table 2 and the posterior distribution in Figure 6. The posterior for C_{22} is purely a reflection of the prior limiting $C_{22} \leq \frac{1}{2}J_2R^2$. Since C_{22} is not detected, the corresponding spin longitude parameter, ω_{sp}, is unconstrained, with a uniform distribution between 0-360°. This is expected since the mutual orbit is much longer than Borasisi's rotation period (~ 46 days and ~ 20 hours, respectively). In future analyses, exclusion of C_{22} may be appropriate, when the orbit to spin period ratio is large. This may reduce the computational expense of the fitting process.

In addition to constraining Borasisi's J_2, and by proxy, its shape, we can also place constraints on Borasisi's obliquity w.r.t. the mutual binary orbit. Our analysis shows an obliquity of $\varepsilon_{sp,orb} = 45.04^{+6.65}_{-4.66}$. This fit is only the prograde obliquity solution, where Borasisi's rotation pole and the binary's mutual orbit lie in the same hemisphere. Another obliquity solution (with $\varepsilon_{retrograde} = 180° - \varepsilon_{prograde}$) exists and provides a similar fit to the data. Distinguishing between these solutions may be possible with additional relative astrometry, depending on how the system's angular momentum is partitioned. In a future work, we will explore why two solutions exist and when they are distinguishable.

Although we do present the individual mass posteriors in Table 2, these are highly degenerate in the current fits and should not be used individually. Prospects for breaking the mass degeneracy will be examined in a future work.

The match between this full non-Keplerian fit and our exploratory fits supports our conclusion that the exploratory fits have identified promising targets for future non-Keplerian analysis and additional observations.

5.1. *Discussion on the inferred J_2 of Borasisi*

Based on the large value of Borasisi's J_2 from our analysis, several interpretations of the results are possible. First, and most simply, Borasisi is extremely flattened, and probably elongated, with a shape most likely resembling a contact binary. Contact binaries are common among the TNOs (Thirouin & Sheppard 2018, 2019; Showalter et al. 2021) and can be part of TNB systems (Rabinowitz et al. 2019). With current constraints on the J_2, it is difficult to say more about Borasisi's shape, but with narrowed uncertainties, detailed shape modeling may be able to distinguish between snowman (like
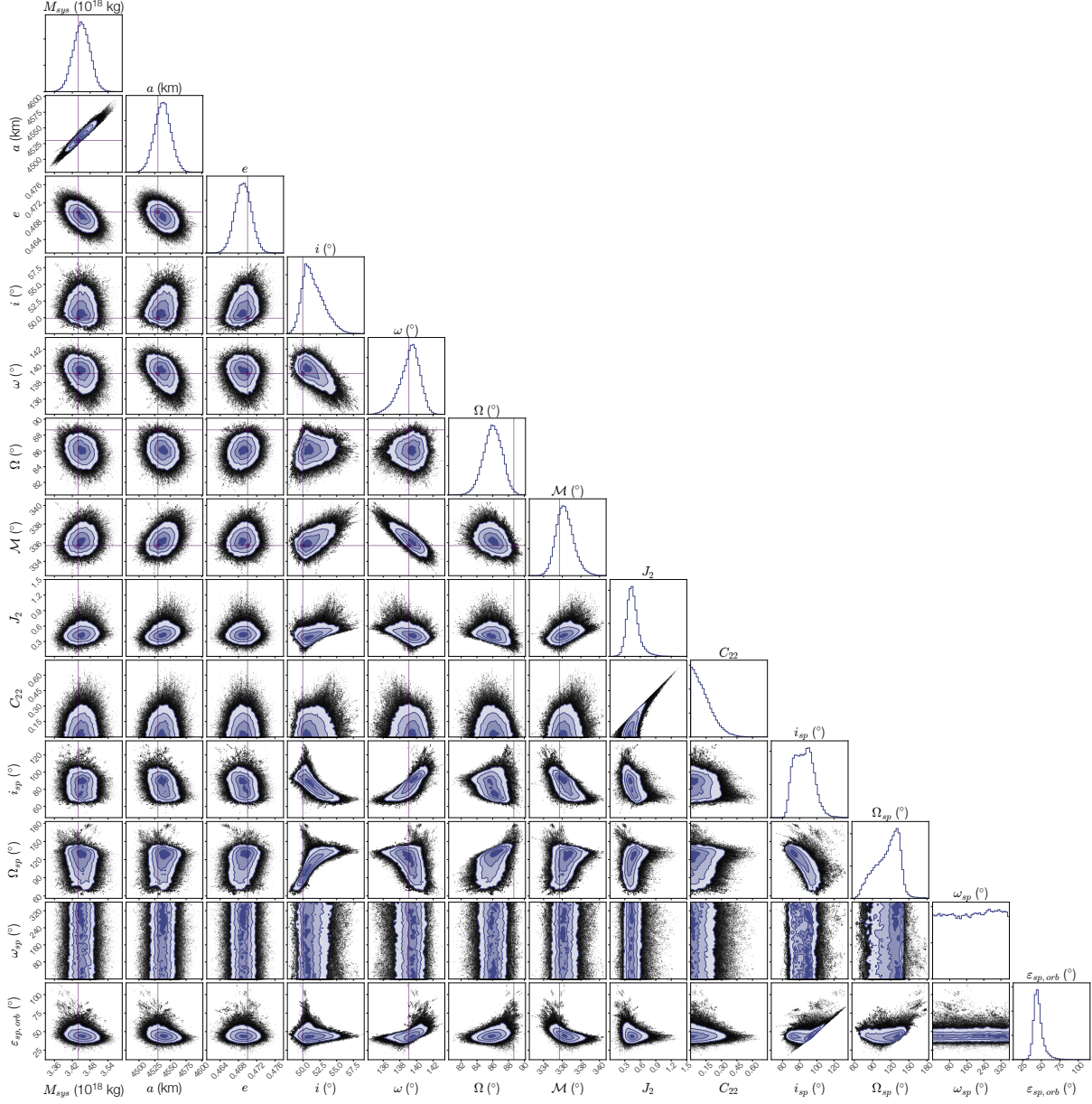
Figure 6. Corner plot for the Borasisi-Pabu non-Keplerian orbit fit in the style of Figure 1. Horizontal and vertical lines correspond to the best fit solution in the Grundy database. The best fit in the `MultiMoon` non-Keplerian fit corresponded to a χ^2 of ~ 11.5 (compared to 21 for the Keplerian fit). Instead of individually plotting the primary and secondary masses, which are completely degenerate, the system mass (M_{sys}) is plotted to better show parameter correlations. Additionally, to allow for comparison with the literature, we show J_2 and C_{22} rather than $J_2 R^2$ and $C_{22} R^2$, where we take the shape to be a triaxial ellipsoid with R as the volumetric radius. Of particular interest is the marginal distribution for J_2 that clearly shows a high value of J_2 is preferred, with $J_2 = 0$ (equivalent to Keplerian motion) being excluded with a significance $> 3\sigma$.

Table 2. Non-Keplerian Orbit Solution for (66652) Borasisi-Pabu

Parameter		Posterior Distribution	Best Fit
Fitted parameters			
Primary mass (10^{18} kg)	M_1	$2.293^{+0.667}_{-0.416}$	2.704
Secondary mass (10^{18} kg)	M_2	$1.159^{+0.416}_{-0.668}$	0.747
Semi-major axis (km)	a	4538^{+13}_{-13}	4535
Eccentricity	e	$0.4690^{+0.0018}_{-0.0018}$	0.4694
Inclination (°)	i	$51.285^{+1.920}_{-1.278}$	50.356
Argument of periapse (°)	ω	$139.31^{+1.03}_{-1.32}$	139.57
Longitude of the ascending node (°)	Ω	$86.02^{+1.17}_{-1.20}$	85.90
Mean anomaly at epoch (°)	$\mathcal{M}$	$336.24^{+0.98}_{-0.85}$	336.00
Primary zonal gravitational harmonic	J_2	$0.4446^{+0.1192}_{-0.0928}$	0.3560
Primary sectoral gravitational harmonic	C_{22}	$0.1033^{+0.1149}_{-0.0735}$	0.096
Primary rotation axis obliquity (°)	i_{sp}	$84.85^{+11.30}_{-11.71}$	91.87
Primary rotation axis precession (°)	Ω_{sp}	$117.60^{+15.84}_{-25.85}$	98.75
Primary rotation axis longitude (°)	ω_{sp}	$184.40^{+120.10}_{-126.35}$	73.24
Derived parameters			
System mass (10^{18} kg)	M_{sys}	$3.451^{+0.029}_{-0.029}$	3.451
Primary obliquity w.r.t. mutual orbit (°)	$\varepsilon_{sp,orb}$	$45.04^{+6.65}_{-4.66}$	43.15
Orbit pole longitude (°)	λ_{orb}	$356.02^{+1.17}_{-1.20}$	355.90
Orbit pole latitude (°)	β_{orb}	$38.72^{+1.28}_{-1.92}$	39.64
Primary rotation pole longitude (°)	λ_{rot}	$27.60^{+15.84}_{-25.85}$	8.75
Primary rotation pole latitude (°)	β_{rot}	$5.15^{+11.71}_{-11.30}$	−1.87

Note—All fitted angles are relative to the J2000 ecliptic plane on JD 2451900.0 (2000 December 21 12:00 UT). Assumed c-axes for primary and secondary are 63 km and 54 km, respectively (Vilenius et al. 2014). We use a rotation period of 6.4 hours (Kern 2006). Our fit presented here is only to the prograde obliquity solution, another solution with obliquity of $\sim 135°$ also exists. Our fitted parameters $J_2 R^2$ and $C_{22} R^2$ are presented here as J_2 and C_{22} to make comparison with the literature easier; in this transformation we take R to be volumetric radius. As mentioned in the text, we are not able to break the primary-secondary mass degeneracy, so we urge caution in using our fits for the masses. The best fit in the `MultiMoon` non-Keplerian fit corresponded to a χ^2 of ~ 11.5 (compared to 21 for the Keplerian fit). We find that using our best fit Keplerian case, for this fit we find $\frac{\mathcal{L}_K}{\mathcal{L}_{NK}} = 8.34 \times 10^{-3}$. RMS residuals are 2 milliarcseconds in both longitude and latitude.
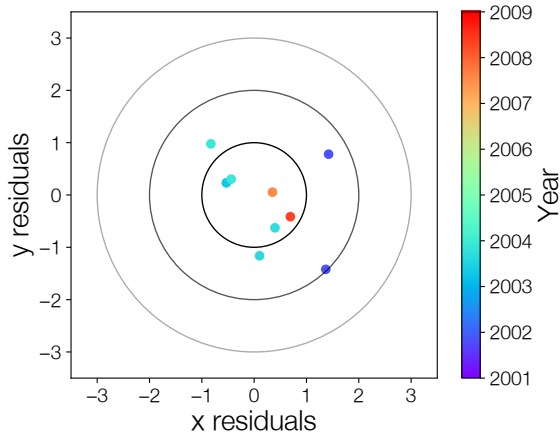
Figure 7. Residual plot for the Borasisi-Pabu non-Keplerian orbit fit in the style of Figure 2. The best fit in the `MultiMoon` non-Keplerian fit corresponded to a χ^2 of ~11.5. RMS residuals are 2 milliarcseconds in both longitude and latitude. Error contours here are the same size as in Figure 2.

Arrokoth) or peanut contact binaries (like Kleopatra) (as in Marchis et al. 2005b).

Our measurement of Borasisi's obliquity (~ 45°) is somewhat surprising, as most asteroid binaries have orbits fairly well-aligned with the rotation pole of the primary. TNBs, however, are formed differently and exhibit properties not seen in asteroid binaries. The closest comparison to Borasisi-Pabu is Manwë-Thorondor; Manwë is possibly a contact binary inclined to its mutual orbit by 27° (Rabinowitz et al. 2019). Both are Cold Classicals. Combined with a similar mutual orbit eccentricity, total system mass, and separation, the Manwë-Thorondor system is strikingly similar to the Borasisi-Pabu system. Indeed, if we calculate Manwë's J_2 (based on the shape model from Rabinowitz et al. (2019)), we find a value very similar to Borasisi's. These objects may be part of a larger population of contact (or compact) binaries with oblique satellites.

The study of this population of objects should focus on explaining how these objects formed and evolved over the history of the solar system. One possible hypothesis is that these systems formed with relatively circular and coplanar orbits. Then, due to their somewhat loose separations, close encounters with other TNOs (or TNBs) may have excited their mutual orbits (similar to Campbell et al. 2022). Tidal dissipation is unlikely to be effective at damping eccentricity and inclination in these systems due to the system's large separation and J_2 (Porter & Grundy 2012), so any past excitation would remain visible in their orbits today. Alternatively, these

systems may have formed with eccentric and inclined orbits. More advanced simulations of TNB formation, especially of gravitational collapse of pebble clouds, need to be completed before distinguishing between these (or other) possibilities.

One shortcoming of our model, that may affect our interpretation, is the assumption that Pabu's shape does not contribute to the system dynamics. This is likely an oversimplification given Pabu's large relative size. However, assuming that Borasisi and Pabu have the same obliquities (w.r.t. the mutual orbit) and shapes, we can calculate the required J_2 for each body to match our median J_2R^2, assuming the volumetric radius ratio of Borasisi and Pabu is ~0.8 (Vilenius et al. 2014). We find that each body would have $J_2 \sim 0.3$, still a shape that is consistent with a contact binary (see Figure 9 of Marchis et al. 2005b). In the case where the obliquities are not aligned, J_2 for each object would have to be even higher. This still implies that at least one system component must be a contact or compact binary. In the future, if more data becomes available for the Borasisi-Pabu system, a more complicated model of the system's dynamics including quadrupole gravity for Pabu may be warranted.

A second possible interpretation of the large J_2 value found in our analysis is that the Borasisi-Pabu system hosts another unresolved component. The possible properties of this unresolved component, assuming all three components are spheres, can be explored using Equation 4. In Figure 8, we plot the possible configurations (in terms of mass ratio and separation) of the unresolved component based on our median J_2R^2 and its 1, 2, and 3σ uncertainties. It clearly shows that a wide range of allowed system configurations exist. While some are potentially resolvable with HST's Wide Field Camera 3 (WFC3), it is unlikely that resolvable satellites (with separations of $\gtrsim$2000 km) would be dynamically stable for long times with Pabu (periapse of 2400 km). However, unresolvable near-equal-mass inner binaries with separations of a few hundred kilometers are quite possible. We also draw comparisons with other known tight binaries 2011 JY_{31}, 2014 WC_{510}, and Lempo-Hiisi, the inner binary in the Lempo triple system. These three comparisons have a range of masses, with Lempo being much more massive than Borasisi-Pabu and 2011 JY_{31} being much less massive, but they illustrate that an unresolved system component is a plausible explanation for the detected non-Keplerian effects.

Under the unresolved binary interpretation, the obliquity measured in our analysis is a proxy for the inclination of the unresolved object's orbit w.r.t. the orbit of
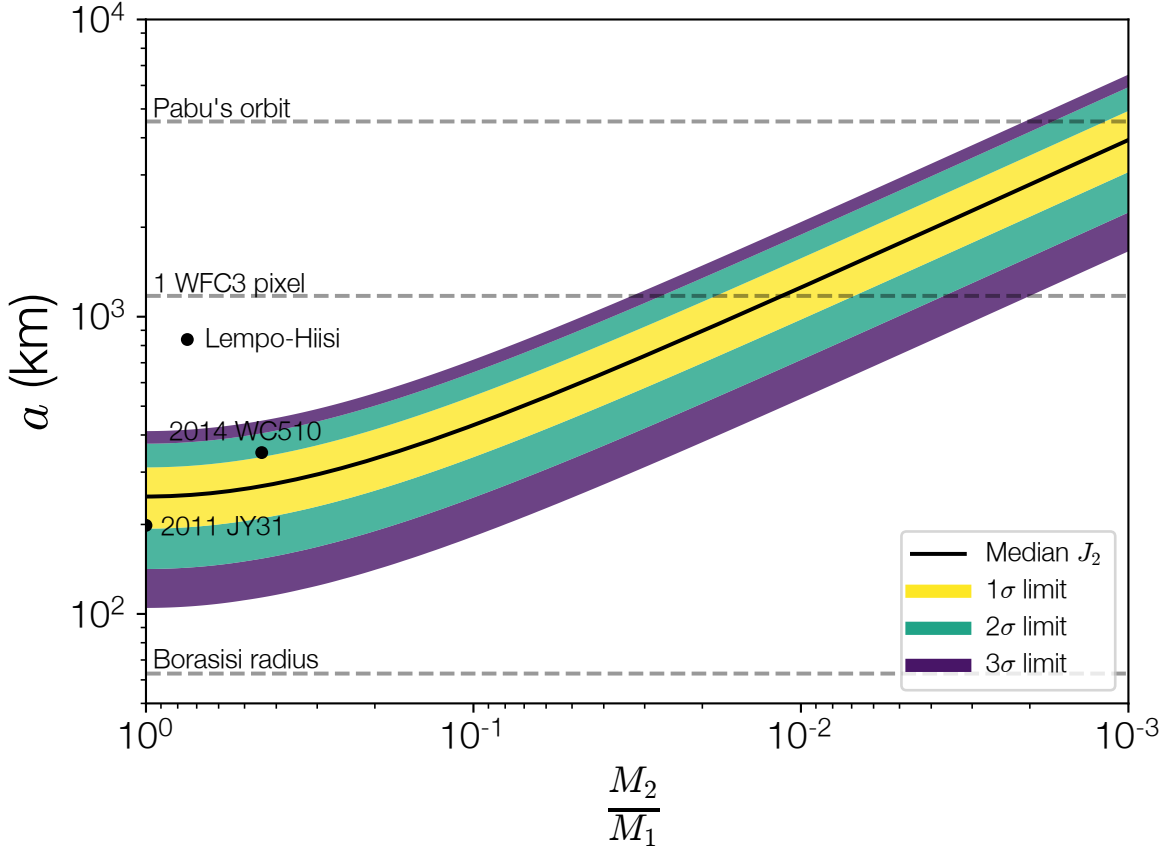
Figure 8. Constraints on the mass-ratio and separation of a putative unresolved binary in the Borasisi system. The thick black line shows the mass ratio and separation given by the median value of the inferred J_2 implied by equation 4. Colored contours indicate the 1, 2, and 3σ ranges from the J_2 posterior. Gray dashed lines show several separations for reference. Here, we adopt a radius of 63 km for Borasisi, but this could be smaller, especially at mass ratios close to 1. The separation equivalent to a single Wide Field Camera 3 (WFC3) pixel on HST is calculated based on Borasisi-Pabu's typical distance from Earth and the instrument's 0.04" px^{-1} pixel scale. The separation of Pabu's orbit is shown in Table 2. The black points show other close binaries known in our solar system. Data for Lempo-Hiisi is from Ragozzine et al. (2023), 2014 WC510 is from Leiva et al. (2020) and assumes equal densities and albedos, and for 2011 JY31 is from Weaver et al. (2022) and assumes equal masses. The J_2 found in our analysis is consistent with an unresolved binary interpretation, as the separation of the binary would be less than a single HST pixel across a wide range of mass ratios.

Pabu. An inclination of $\sim 45°$ is above the critical inclination where the Kozai-Lidov mechanism can be active ($i_{crit} \approx 39.2°$), but if the central components are significantly aspherical, Kozai-Lidov cycling can be avoided. The short- and long-term dynamics of triple systems are extremely interesting and complex, but we leave a full investigation of them to future work.

Assessing the relative probability of each of our interpretations (contact binary and unresolved component) is impossible at the 2-quadrupole level. However, additional 3-body analysis with `MultiMoon` may allow us to infer the orbit of an undetected system component

since it would induce somewhat different non-Keplerian motion. Additionally, other observations of light curves, thermal emission, or occultations may enable us to distinguish between these two interpretations.

Alternatively, our results could be caused by systematic errors stemming from the data acquisition, reduction, or fitting processes. When comparing Figures 2 and 7, it seems that the improvement in orbit fit is due to enhancing the fit for the last few data points. This is expected from a true non-Keplerian orbit, as non-Keplerian deviations grow linearly in time, but could also indicate unknown systematics. As we are using

only 9 independent observations, distinguishing between these possibilities is difficult. We do point out however, that our non-Keplerian model is able to match the observations taken extremely well, which would be unlikely to occur given randomly distributed systematics. Additionally, our model outputs are physically realistic and similar to other known binary systems containing a contact binary (e.g., Manwë). Understanding if systematic errors can masquerade as non-Keplerian effects for the Borasisi-Pabu system will require additional observations of the system.

After completing all the analysis discussed in this Section, a new study of TNO light curve found a different light curve period for Borasisi of 19.868 ± 0.032 hours with an amplitude of $\Delta m = 0.216 \pm 0.057$ (Kecskeméthy et al. 2023). However, our testing showed that our results were robust to different primary rotation periods, so we do not include this new rotation period in our analysis. The fairly high amplitude light curve, however, is generally compatible with our results.

5.2. *Potential For Future Observations*

Future observations are key to confirming the results we present here, and will enable us to significantly narrow the uncertainties associated with our modeling. Any additional observations will strengthen the detection of non-Keplerian effects, and may enable us to break the degeneracies associated with our modeling. To illustrate the ability of future observations to improve our orbital models, in Figure 9 we have plotted the "information gain" as a result of additional observations at any given time during the first quarter of 2023, along with the separation of the binary. We define information gain as the size of the cloud of projected positions of the secondary, in units of typical HST observations. This can be written:

$$I.G.(t) = \sqrt{\left(\frac{\sigma_{x,pred}(t)}{\sigma_{x,typ}}\right)^2 + \left(\frac{\sigma_{y,pred}(t)}{\sigma_{y,typ}}\right)^2} \quad (6)$$

where $\sigma_{x,pred}$, $\sigma_{y,pred}$ are the standard deviations of the projected positions from a sample of posterior draws and $\sigma_{x,typ}$, $\sigma_{y,typ}$ are typical error measurements of Pabu's position, based on past HST observations of Borasisi-Pabu. To calculate this, we have taken 1000 random samples from our MCMC chain and used them to predict the position of Pabu at a given time. We then use the ensemble to calculate the information gain.

This is equivalent to calculating the average expected $\sqrt{\chi^2}$ of a new relative astrometric observation given the current posterior distribution (as listed in Table 2). For an observation with no additional constrain-

ing power, information gained is $\sqrt{2}$. Observations can be optimized to best shrink uncertainties by scheduling when information gain is at its maximum. In the case of Borasisi-Pabu, observations in 2023 can significantly shrink measurement uncertainties, which is unsurprising given that Borasisi-Pabu was last observed by HST in 2008. Targeting observations at times of high information gain allow for optimization of observing schedules. In addition, observing when Borasisi and Pabu have the greatest separation ensures high data quality, further motivating observations at certain times.

6. CONCLUSIONS

Using a new non-Keplerian Bayesian orbit fitter, `MultiMoon`, we have completed a set of Keplerian and non-Keplerian orbit fits to 45 TNBs. Our Keplerian orbit fits are in close agreement with those previously completed in the literature, validating `MultiMoon`'s orbit fitting procedures. Our exploratory non-Keplerian fits were run with the goal of identifying targets for full non-Keplerian analysis and possible observational campaigns. Almost 20% (8/45) of TNBs analyzed have detectable non-Keplerian effects altering their orbits, with many systems with nearly significant detections. The 8 systems we identify for future analysis and observation are Salacia-Actaea, Orcus-Vanth, Gonggong-Xiangliu, Borasisi-Pabu, Altjira, Varda-Ilmarë, 1999 RT$_{214}$, and Sila-Nunam.

Our analysis is consistent with previous expectations that large TNOs are nearly spherical. The large TNB systems with detectable non-Keplerian effects are all consistent with an oblate spheroidal shape. We find that small TNBs host extremely aspherical components. Of the small TNBs with detectable non-Keplerian effects, almost all are consistent with contact binary shapes, though we are biased to highly non-spherical objects. We also identify a possible population of widely separated hierarchical triples, although these detections individually do not quite reach our detection significance threshold. Our ensemble of exploratory non-Keplerian fits is consistent with their Keplerian counterparts for the TNB system's mass, semi-major axis, eccentricity, and inclination. This indicates that there are no systematics introduced by non-Keplerian effects that may invalidate past Keplerian orbital analyses of TNBs.

As an illustration of how our target list can be used to inform future non-Keplerian analyses, we have completed a full non-Keplerian fit to the mutual orbit of Borasisi-Pabu. Our analysis confirms the finding of our exploratory fits, finding that non-Keplerian motion is detectable in the system at the $> 3\sigma$ level. We find that, assuming a triaxial shape, Borasisi (and/or Pabu)
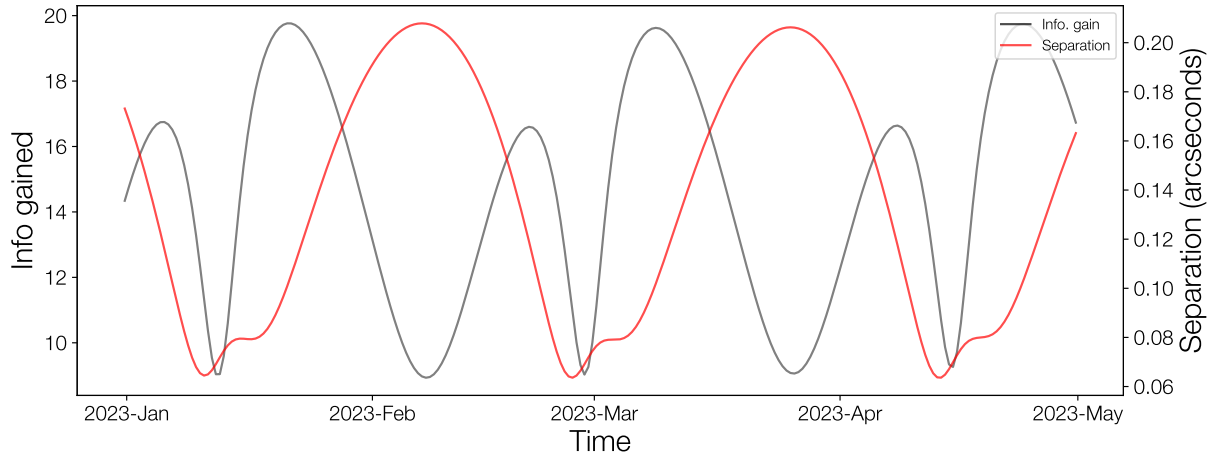
Figure 9. A plot showing the change in "information gained" by a single HST observation (in gray) and separation of Borasisi and Pabu (in red) in the first quarter of 2023. The information gained by single observations is a statistic which compares the uncertainty in the projected position of a system's secondary to the uncertainty of a typical observation (Equation 6). Information gained clearly shows large variations; observing at times of maximum information gained allows for maximum leverage over reducing uncertainties. Additionally, avoiding times of close separation can ensure high quality data.

is extremely flattened and elongated, and may be a contact binary. Another interpretation of our results is that Borasisi (and/or Pabu) may themselves be a compact binary, making the system a hierarchical triple system like Lempo.

Future observations of potentially non-Keplerian TNBs are of high priority since these effects are a unique probe into TNB shapes and sizes. Many of the systems we have identified as having currently detectable non-Keplerian effects have not been observed in more than a decade allowing significant orbital precession to accumulate. High resolution relative astrometry combined with non-Keplerian models can further confirm our results, narrow uncertainties, and break degeneracies.

APPENDIX

A. KEPLERIAN FITS WITH CONSTANT OFFSETS

In addition to regular Keplerian fits, we completed another set of Keplerian fits in which the model allows for a constant offset between a TNB primary's center of light (photocenter) and center of mass. When observing TNOs, photocenter offsets can be caused by three different mechanisms. Firstly, at non-zero phase angles, the photocenter and center of mass of an object will be slightly misaligned, even for a spherical object, due to the viewing geometry. This effect is enhanced when objects are aspherical or have drastic albedo features (e.g., Sputnik Planitia on Pluto). The misalignment, however, even for extremely aspherical shapes and extreme albedo variations will generally only amount to a small fraction of the object's overall angular diameter. The angular diameters of the TNB components in our dataset are $\lesssim 40$ milliarcseconds, therefore, constant misalignments between the photocenter and center of mass of an object will be $\lesssim 5$ milliarcseconds for the largest objects in our sample, and much smaller for the majority of objects. This is comparable to the observational uncertainty of a few milliarcseconds for most objects.

Secondly, previously undetected close-in satellites can also cause photocenter offsets, due to light contamination from the secondary. For single observations the offset could be sizeable, depending on the mass, density, and albedo of the

undetected satellite, but given a series of observations, the misalignment from a close-in satellite on a circular orbit will generally average out to zero. For an eccentric satellite however, the satellite will spend more time near apoapse, naturally causing an average photocenter-barycenter misalignment. Incomplete sampling of the putative undetected satellite's orbit and an eccentric orbit can both cause an average change in the primary's photocenter.

Third, objects with complex shapes and potentially heterogeneous interiors can have center-of-mass–center-of-figure offsets. Even neglecting the above effects, this would lead to a center-of-light offset.

A full model of potential center-of-light/center-of-mass/center-of-figure variations for non-spherical shapes under varying illumination and observation conditions would be highly complex. Most of this complexity would be well below the detectability threshold. However, to explore these effects we add two parameters to our Keplerian model that represent a simple constant offset to the modeled astrometry (in ecliptic longitude and latitude). These fits allow us to consider any potential astrometric offsets produced by aspherical objects (e.g., the center of reflected light from an object may be offset from the center of mass) or contamination from previously undetected components of the TNB system (e.g., small moons close to the primary that are unresolvable with current telescopes). These fits were run and analyzed identically to the normal Keplerian fits.

In our ensemble of Keplerian fits with constant offsets, results were varied. In most cases, the fits, when compared to the normal Keplerian fits, showed little to no improvement in quality. Despite this, a few objects had large improvements to the quality of the fits. However, the majority of these large improvements came at the cost of unrealistically large constant offsets (no significant improvements were obtained with offsets less than 5 mas). While this may indicate the presence of undetected components in the TNB system, many of the offsets were probably much too large to be caused by plausible undetected system components (offsets could be as large as ∼90 mas).

The improvement in fit is most likely due to overfitting. Our parametrization will always enable an improvement in fit by shifting the 2-dimensional residual cloud towards the origin. This is amplified by the small dataset used, with some TNBs only having 5 observations. This, combined with the physically unrealistic offsets found, convince us that the use of constant photocenter offsets is not warranted at this time.

Although we discard these fits, some insights can still be learned from examining their results (which are available upon request). In cases where there is improvement to the quality of the fit over the Keplerian (small or large improvements), the inclusion of constant offsets generally alters the fitted eccentricity of the TNB's orbit. In most cases, the fits with offsets show a small decrease in the fitted eccentricity, although increases can occur. When the Grundy best fits (without offsets) are compared to the posterior distributions from the constant offset fits (in a similar way to the data in Figure 3), the z-scores are similarly small for all parameters except eccentricity. This indicates that even if constant photocenter offsets are present in TNB relative astrometry, results based on the ensemble of TNB orbits (e.g., the mutual inclination distribution) are unaffected.

The non-detection of any believable constant photocenter offset, is not overly surprising. In reality, photocenter offsets (from any source) are time-varying. For offsets due to viewing geometry, most of the variation is caused by the Earth's orbit around the Sun, with the TNB's heliocentric orbit making a small contribution. Offsets from albedo variations and aspherical shapes will vary with the rotational period of the object in question. Future investigations of photocenter offsets should use a more physically realistic model, which accounts for the phase angle and rotation phase/rate of the modeled objects. These models may be able to constrain the shapes and albedo variations of TNB components once sufficiently high resolution data is available.

Table A1. Keplerian Orbital Fits

Object	RMS residual (arcsec)	M_{sys} (10^{18} kg)	a (km)	e	i (°)	ω (°)	Ω (°)	$\mathcal{M}$ (°)
(26308) 1998 SM$_{165}$	0.001	$6.880^{+0.015}_{-0.015}$	11372^{+8}_{-8}	$0.4733^{+0.0006}_{-0.0006}$	$66.303^{+0.061}_{-0.062}$	$49.32^{+0.11}_{-0.11}$	$52.35^{+0.07}_{-0.07}$	$165.51^{+0.09}_{-0.09}$
(42355) Typhon-Echidna	0.001	$0.946^{+0.053}_{-0.05}$	1625^{+30}_{-29}	$0.5259^{+0.0155}_{-0.0149}$	$49.563^{+1.935}_{-1.785}$	$129.51^{+2.09}_{-2.06}$	$230.55^{+3.41}_{-3.32}$	$19.08^{+1.76}_{-1.81}$
(50000) Quaoar-Weywot, *pro.*	0.004	$1210.333^{+20.811}_{-20.708}$	13315^{+76}_{-76}	$0.0217^{+0.0055}_{-0.0052}$	$14.636^{+0.501}_{-0.493}$	$298.49^{+9.14}_{-8.50}$	$353.16^{+1.43}_{-1.39}$	$236.77^{+8.34}_{-8.97}$
(50000) Quaoar-Weywot, *retro.*	0.004	$1215.502^{+22.613}_{-21.104}$	13335^{+82}_{-78}	$0.0217^{+0.0052}_{-0.0057}$	$150.011^{+0.521}_{-0.514}$	$298.45^{+9.08}_{-8.97}$	$346.44^{+0.78}_{-0.71}$	$241.51^{+8.70}_{-8.77}$
(55637) 2002 UX$_{25}$	0.009	$124.615^{+3.010}_{-2.717}$	4771^{+38}_{-35}	$0.1735^{+0.0237}_{-0.0243}$	$84.447^{+0.265}_{-0.278}$	$16.52^{+1.22}_{-1.41}$	$203.30^{+0.27}_{-0.27}$	$289.39^{+1.43}_{-1.33}$
(58534) Logos-Zoe	0.005	$0.452^{+0.009}_{-0.008}$	8180^{+55}_{-53}	$0.5424^{+0.0073}_{-0.0073}$	$72.893^{+0.558}_{-0.563}$	$201.47^{+0.53}_{-0.52}$	$17.06^{+0.39}_{-0.40}$	$35.35^{+0.87}_{-0.90}$
(60458) 2000 CM$_{114}$	0.003	$2.018^{+0.053}_{-0.054}$	2504^{+22}_{-23}	$0.0389^{+0.0150}_{-0.0140}$	$71.032^{+1.894}_{-1.763}$	215^{+20}_{-17}	$278.34^{+2.26}_{-2.40}$	71^{+280}_{-63}
(65489) Ceto-Phorcus, *pro.*	0.001	$5.423^{+0.338}_{-0.364}$	1842^{+38}_{-42}	$0.0095^{+0.0066}_{-0.0049}$	$76.238^{+3.135}_{-2.464}$	251^{+57}_{-151}	$112.78^{+3.53}_{-3.32}$	244^{+89}_{-185}
(65489) Ceto-Phorcus, *retro.*	0.002	$5.687^{+0.352}_{-0.339}$	1872^{+38}_{-38}	$0.0113^{+0.0080}_{-0.0057}$	$133.708^{+2.312}_{-2.513}$	281^{+36}_{-141}	$121.05^{+4.36}_{-4.27}$	301^{+35}_{-197}
(66652) Borasisi-Pabu	0.002	$3.432^{+0.026}_{-0.027}$	4528^{+12}_{-12}	$0.4696^{+0.0017}_{-0.0017}$	$50.004^{+0.318}_{-0.315}$	$139.24^{+0.31}_{-0.31}$	$88.68^{+0.48}_{-0.48}$	$335.58^{+0.46}_{-0.46}$
(79360) Sila-Nunam	0.003	$10.821^{+0.206}_{-0.199}$	2775^{+17}_{-17}	$0.0158^{+0.0167}_{-0.0098}$	$120.829^{+0.339}_{-0.342}$	173^{+14}_{-112}	$134.00^{+0.63}_{-0.63}$	50^{+149}_{-14}
(80806) 2000 CM$_{105}$	0.006	$0.823^{+0.079}_{-0.085}$	2348^{+72}_{-83}	$0.0228^{+0.0158}_{-0.0112}$	$61.613^{+3.037}_{-3.087}$	244^{+30}_{-85}	$201.71^{+3.21}_{-2.65}$	257^{+47}_{-151}
(88611) Teharonhiawako-Sawiskera	0.027	$2.437^{+0.027}_{-0.027}$	27645^{+103}_{-103}	$0.2484^{+0.0018}_{-0.0018}$	$127.637^{+0.332}_{-0.336}$	$301.84^{+0.49}_{-0.49}$	$36.43^{+0.46}_{-0.46}$	$276.05^{+0.44}_{-0.45}$
(90482) Orcus-Vanth	0.003	$632.995^{+3.468}_{-3.728}$	8991^{+16}_{-18}	$0.0012^{+0.0007}_{-0.0006}$	$90.276^{+0.344}_{-0.329}$	250^{+37}_{-37}	$50.94^{+0.37}_{-0.40}$	222^{+33}_{-44}
(119979) 2002 WC$_{19}$, *pro.*	0.010	$83.053^{+5.464}_{-5.465}$	4198^{+90}_{-94}	$0.2357^{+0.0372}_{-0.0401}$	$25.482^{+0.667}_{-0.625}$	$137.35^{+2.51}_{-2.76}$	$120.59^{+1.92}_{-1.89}$	$354.29^{+4.29}_{-352.84}$
(119979) 2002 WC$_{19}$, *retro.*	0.010	$70.926^{+3.714}_{-3.342}$	3983^{+68}_{-64}	$0.1955^{+0.0428}_{-0.0434}$	$160.106^{+0.763}_{-0.765}$	$154.51^{+3.29}_{-4.06}$	$232.19^{+2.20}_{-2.19}$	$350.46^{+3.64}_{-3.73}$
(120347) Salacia-Actaea	0.011	$488.855^{+10.003}_{-9.911}$	5710^{+39}_{-39}	$0.0062^{+0.0031}_{-0.0027}$	$17.905^{+0.515}_{-0.493}$	257^{+80}_{-239}	$109.97^{+1.75}_{-1.84}$	197^{+63}_{-38}
(123509) 2000 WK$_{183}$, *blended*	0.003	$1.100^{+0.037}_{-0.032}$	2367^{+26}_{-23}	$0.0132^{+0.0070}_{-0.0059}$	$93.8^{+7.4}_{-9.9}$	200^{+35}_{-56}	158^{+17}_{-8}	260^{+51}_{-38}
(134860) 2000 OJ$_{67}$, *blended*	0.002	$1.908^{+0.151}_{-0.118}$	2271^{+58}_{-48}	$0.0354^{+0.0346}_{-0.0188}$	$95.1^{+10.8}_{-11.3}$	147^{+89}_{-32}	232^{+19}_{-15}	59^{+207}_{-32}
(148780) Altjira	0.003	$3.931^{+0.058}_{-0.057}$	9886^{+50}_{-49}	$0.3433^{+0.0041}_{-0.0040}$	$25.195^{+0.204}_{-0.206}$	$192.89^{+0.67}_{-0.66}$	$274.59^{+0.36}_{-0.36}$	$122.76^{+0.76}_{-0.75}$
(160091) 2000 OL$_{67}$, *pro.*	0.047	$0.289^{+0.026}_{-0.023}$	7600^{+224}_{-210}	$0.2279^{+0.0211}_{-0.0211}$	$87.2^{+5.9}_{-5.4}$	$37.42^{+3.51}_{-3.14}$	$226.48^{+4.46}_{-3.75}$	$87.08^{+2.74}_{-3.13}$
(160091) 2000 OL$_{67}$, *retro.*	0.045	$0.315^{+0.033}_{-0.027}$	7816^{+262}_{-230}	$0.2226^{+0.0271}_{-0.0253}$	$88.0^{+10.8}_{-10.7}$	$39.78^{+3.69}_{-3.91}$	$290.35^{+3.69}_{-3.65}$	$85.71^{+3.50}_{-3.82}$
(160256) 2002 PD$_{149}$	0.011	$0.540^{+0.022}_{-0.020}$	26748^{+333}_{-320}	$0.5886^{+0.0091}_{-0.0089}$	$26.760^{+0.487}_{-0.476}$	$144.98^{+1.18}_{-1.19}$	$96.47^{+1.11}_{-1.11}$	$171.41^{+2.64}_{-2.63}$
(174567) Varda-Ilmarë, *pro.*	0.005	$265.150^{+5.379}_{-5.435}$	4801^{+33}_{-33}	$0.0240^{+0.0055}_{-0.0053}$	$68.323^{+1.975}_{-1.964}$	$329.3^{+12.6}_{-14.6}$	$315.95^{+1.81}_{-1.67}$	$137.9^{+14.3}_{-12.8}$
(174567) Varda-Ilmarë, *retro.*	0.005	$265.399^{+5.748}_{-5.256}$	4802^{+34}_{-32}	$0.0174^{+0.0048}_{-0.0049}$	$77.217^{+1.967}_{-2.064}$	298^{+19}_{-22}	$2.92^{+1.87}_{-1.60}$	154^{+22}_{-19}
(225088) Gonggong-Xiangliu, *pro.*	0.006	$1765.784^{+70.143}_{-71.451}$	24201^{+316}_{-331}	$0.2852^{+0.0086}_{-0.0079}$	$63.652^{+1.461}_{-1.404}$	$63.14^{+1.50}_{-1.63}$	$35.11^{+1.55}_{-1.59}$	$97.31^{+1.87}_{-1.85}$
(225088) Gonggong-Xiangliu, *retro.*	0.005	$1728.671^{+59.377}_{-52.122}$	24032^{+272}_{-244}	$0.2910^{+0.0085}_{-0.0079}$	$121.456^{+1.358}_{-1.308}$	$67.04^{+1.59}_{-1.55}$	$89.17^{+1.73}_{-1.83}$	$95.54^{+2.05}_{-2.03}$
(229762) Gǃkúnǁ'hòmdímà-Gǃò'é ǃhú	0.016	$136.625^{+3.682}_{-3.883}$	6044^{+54}_{-58}	$0.0234^{+0.0079}_{-0.0064}$	$55.444^{+0.735}_{-0.748}$	312^{+16}_{-24}	$127.99^{+1.15}_{-1.10}$	254^{+23}_{-15}
(275809) 2001 QY$_{297}$	0.0004	$4.109^{+0.038}_{-0.038}$	9964^{+31}_{-30}	$0.4174^{+0.0023}_{-0.0023}$	$161.001^{+0.107}_{-0.108}$	$316.84^{+0.49}_{-0.49}$	$15.47^{+0.74}_{-0.72}$	$181.45^{+0.43}_{-0.44}$
(341520) Mors-Somnus	0.023	$0.745^{+0.020}_{-0.020}$	20657^{+154}_{-153}	$0.1568^{+0.0023}_{-0.0023}$	$15.62^{+0.189}_{-0.188}$	$320.15^{+2.72}_{-2.81}$	$331.42^{+0.92}_{-0.95}$	$294.52^{+3.62}_{-3.54}$
(364171) 2006 JZ$_{81}$	0.047	$1.332^{+0.236}_{-0.198}$	33338^{+1755}_{-1653}	$0.8517^{+0.0100}_{-0.0112}$	$12.631^{+0.676}_{-0.574}$	$170.64^{+0.79}_{-0.78}$	$80.62^{+2.42}_{-2.22}$	$75.41^{+1.91}_{-2.16}$

Table A1 *continued*

Table A1 *(continued)*

Object	RMS residual (arcsec)	M_{sys} (10^{18} kg)	a (km)	e	i (°)	ω (°)	Ω (°)	$\mathcal{M}$ (°)
(385446) Manwë-Thorondor	0.011	$1.946^{+0.035}_{-0.034}$	6681^{+40}_{-39}	$0.5643^{+0.0067}_{-0.0065}$	$48.541^{+0.252}_{-0.245}$	$77.81^{+1.93}_{-1.96}$	$170.62^{+0.51}_{-0.51}$	$236.50^{+1.98}_{-1.95}$
(469705) ǂKá̦gára-Hãunu	0.010	$2.167^{+0.131}_{-0.119}$	7656^{+151}_{-142}	$0.6928^{+0.0137}_{-0.0135}$	$10.150^{+0.412}_{-0.412}$	$170.21^{+1.07}_{-0.98}$	$12.84^{+1.07}_{-1.02}$	$312.57^{+0.42}_{-0.39}$
(508788) 2000 CQ$_{114}$	0.001	$0.544^{+0.008}_{-0.008}$	6935^{+35}_{-34}	$0.096^{+0.0047}_{-0.0045}$	$44.145^{+0.461}_{-0.464}$	$333.60^{+3.75}_{-3.89}$	$132.92^{+0.70}_{-0.72}$	$309.21^{+4.54}_{-4.43}$
(508869) 2002 VT$_{130}$, *pro.*	0.002	$2.325^{+0.211}_{-0.196}$	3028^{+89}_{-87}	$0.0207^{+0.0089}_{-0.0082}$	$65.465^{+3.257}_{-2.755}$	48^{+299}_{-37}	$127.92^{+2.33}_{-2.31}$	294^{+28}_{-39}
(508869) 2002 VT$_{130}$, *retro.*	0.002	$2.255^{+0.153}_{-0.145}$	2998^{+66}_{-66}	$0.0219^{+0.0073}_{-0.0069}$	$111.021^{+2.707}_{-2.898}$	73^{+29}_{-31}	$191.87^{+2.18}_{-2.22}$	231^{+31}_{-28}
(524366) 2001 XR$_{254}$	0.002	$4.044^{+0.062}_{-0.060}$	9302^{+49}_{-48}	$0.5558^{+0.0046}_{-0.0045}$	$20.124^{+0.203}_{-0.202}$	$286.95^{+0.86}_{-0.86}$	$321.94^{+0.49}_{-0.48}$	$265.71^{+0.68}_{-0.67}$
(524531) 2002 XH$_{91}$	0.009	$6.469^{+0.415}_{-0.354}$	22405^{+463}_{-410}	$0.7125^{+0.0155}_{-0.0162}$	$33.865^{+1.407}_{-1.545}$	$196.61^{+1.82}_{-1.49}$	$239.11^{+2.14}_{-2.23}$	$203.92^{+2.43}_{-2.98}$
(525462) 2005 EO$_{304}$	0.054	$2.131^{+0.023}_{-0.023}$	69601^{+226}_{-223}	$0.2154^{+0.0012}_{-0.0012}$	$13.283^{+0.071}_{-0.071}$	$208.68^{+2.15}_{-2.11}$	$257.94^{+0.93}_{-0.94}$	$185.32^{+1.19}_{-1.20}$
(612095) 1999 OJ$_4$	0.010	$0.406^{+0.007}_{-0.007}$	3310^{+19}_{-19}	$0.3675^{+0.0039}_{-0.0038}$	$54.460^{+0.819}_{-0.820}$	$82.44^{+1.09}_{-1.09}$	$259.39^{+1.19}_{-1.22}$	$67.85^{+0.84}_{-0.83}$
(612147) 2000 CF$_{105}$	0.050	$0.187^{+0.003}_{-0.003}$	33387^{+119}_{-117}	$0.2978^{+0.0080}_{-0.0079}$	$167.585^{+0.177}_{-0.180}$	$296.97^{+1.27}_{-1.25}$	$224.86^{+0.85}_{-0.85}$	$262.36^{+0.81}_{-0.83}$
(612176) 2000 QL$_{251}$	0.003	$3.094^{+0.028}_{-0.028}$	4992^{+15}_{-15}	$0.4897^{+0.0040}_{-0.0040}$	$131.653^{+0.570}_{-0.568}$	$12.28^{+0.32}_{-0.32}$	$89.64^{+0.90}_{-0.90}$	$353.91^{+0.63}_{-0.62}$
(612239) 2001 QC$_{298}$	0.002	$11.853^{+0.154}_{-0.143}$	3810^{+15}_{-15}	$0.3342^{+0.0024}_{-0.0024}$	$54.994^{+0.384}_{-0.382}$	$209.65^{+0.27}_{-0.27}$	$95.18^{+0.51}_{-0.49}$	$353.13^{+0.43}_{-0.42}$
(612687) 2003 UN$_{284}$	0.076	$1.270^{+0.084}_{-0.076}$	53235^{+1068}_{-1006}	$0.375^{+0.0183}_{-0.0178}$	$25.671^{+0.304}_{-0.308}$	$168.52^{+1.22}_{-1.14}$	$93.48^{+1.17}_{-1.12}$	$291.05^{+2.45}_{-2.57}$
1998 WW$_{31}$	0.010	$2.663^{+0.016}_{-0.016}$	22631^{+46}_{-46}	$0.8187^{+0.0021}_{-0.0021}$	$48.055^{+0.396}_{-0.385}$	$221.74^{+0.38}_{-0.38}$	$117.79^{+0.60}_{-0.58}$	$42.35^{+0.35}_{-0.35}$
1999 RT$_{214}$	0.004	$0.192^{+0.010}_{-0.009}$	3386^{+56}_{-55}	$0.2904^{+0.0217}_{-0.0219}$	$24.112^{+1.309}_{-1.243}$	$77.65^{+2.97}_{-2.99}$	$74.21^{+2.65}_{-2.70}$	$329.08^{+2.87}_{-2.91}$
2001 QW$_{322}$	0.092	$2.032^{+0.023}_{-0.022}$	103657^{+317}_{-310}	$0.4592^{+0.0015}_{-0.0015}$	$150.789^{+0.172}_{-0.170}$	$251.31^{+0.25}_{-0.25}$	$241.52^{+0.29}_{-0.29}$	$164.68^{+0.26}_{-0.26}$
2003 QY$_{90}$	0.016	$0.516^{+0.017}_{-0.015}$	8544^{+90}_{-87}	$0.6602^{+0.0098}_{-0.0098}$	$54.581^{+0.463}_{-0.441}$	$146.53^{+0.89}_{-0.87}$	$131.58^{+0.48}_{-0.46}$	$26.00^{+2.16}_{-2.28}$
2003 TJ$_{58}$	0.002	$0.237^{+0.010}_{-0.009}$	3842^{+51}_{-48}	$0.5169^{+0.0081}_{-0.0079}$	$61.650^{+1.803}_{-1.762}$	$254.62^{+1.92}_{-2.01}$	$193.33^{+2.34}_{-2.42}$	$333.33^{+1.89}_{-1.85}$
2004 PB$_{108}$	0.001	$9.443^{+0.325}_{-0.312}$	10389^{+121}_{-119}	$0.4368^{+0.0065}_{-0.0065}$	$101.278^{+0.956}_{-0.929}$	$209.80^{+0.42}_{-0.41}$	$120.01^{+0.81}_{-0.84}$	$176.59^{+0.33}_{-0.33}$
2006 BR$_{284}$	0.040	$0.580^{+0.007}_{-0.007}$	25454^{+104}_{-104}	$0.2746^{+0.0018}_{-0.0018}$	$55.019^{+0.596}_{-0.584}$	$13.41^{+0.52}_{-0.51}$	$42.47^{+0.46}_{-0.46}$	$182.18^{+0.57}_{-0.57}$
2006 CH$_{69}$	0.046	$1.223^{+0.066}_{-0.067}$	31485^{+567}_{-591}	$0.9174^{+0.0022}_{-0.0023}$	$132.742^{+0.802}_{-0.789}$	$154.80^{+0.64}_{-0.69}$	$111.09^{+0.82}_{-0.87}$	$234.83^{+0.86}_{-0.80}$

NOTE—All fitted angles are relative to the J2000 ecliptic plane. Listed errors are 16 and 84 percentile levels.

Table A2. Non-Keplerian Orbital Fits

Object	$\frac{\mathcal{L}_K}{\mathcal{L}_{NK}}$	Residual (arcsec)	M_{sys} (10^{18} kg)	a (km)	e	i (°)	ω (°)	Ω (°)	$\mathcal{M}$ (°)	J_2	i_{sp} (°)	Ω_{sp} (°)
(26308) 1998 SM$_{165}$	0.18142	0.002	6.884	11374	0.4733	66.296	49.286	52.253	165.594	0.3425	104.833	67.125
(42355) Typhon-Echidna	0.33001	0.0004	1.105	1717	0.5178	43.748	124.229	235.400	24.487	0.1291	25.870	197.303
(50000) Quaoar-Weywot, *pro.*	0.53267	0.003	1211.280	13314	0.0209	13.880	299.937	354.925	233.712	0.0604	120.289	55.900
(50000) Quaoar-Weywot, *retro.*	0.54467	0.004	1214.346	13328	0.0249	150.171	298.836	345.454	240.463	0.0228	157.314	118.475
(55637) 2002 UX$_{25}$	0.65209	0.009	123.885	4761	0.1754	84.330	17.006	203.272	288.844	0.0040	91.551	224.767
(58534) Logos-Zoe	0.95946	0.005	0.450	8166	0.5396	72.750	201.645	17.141	35.030	0.4268	124.195	45.927
(60458) 2000 CM$_{114}$	0.10142	0.003	1.931	2468	0.0399	74.361	203.330	270.567	15.880	0.2368	128.480	20.058
(65489) Ceto-Phorcus, *pro.*	0.70688	0.001	5.323	1831	0.0012	77.513	107.102	111.404	147.204	0.0508	103.094	316.276
(65489) Ceto-Phorcus, *retro.*	0.17520	0.002	5.529	1852	0.0026	132.016	41.156	122.304	215.553	0.1403	160.518	337.142
(66652) Borasisi-Pabu	**0.01465**	**0.002**	**3.445**	**4531**	**0.4680**	**49.715**	**139.836**	**86.232**	**335.745**	**0.2789**	**95.761**	**79.983**
(79360) Sila-Nunam	**0.04804**	**0.003**	**10.951**	**2788**	**0.0168**	**120.243**	**150.972**	**134.927**	**68.092**	**0.1989**	**134.511**	**104.933**
(80806) 2000 CM$_{105}$	1.02954	0.006	0.834	2358	0.0139	61.749	243.138	201.089	288.276	0.0021	102.200	54.812
(88611) Teharonhiawako-Sawiskera	0.11301	0.027	2.424	27564	0.2476	126.786	302.060	36.055	275.907	1.7920	127.862	322.045
(90482) Orcus-Vanth	**0.00170**	**0.003**	**634.265**	**8995**	**0.0008**	**90.484**	**285.772**	**50.549**	**190.674**	**0.0158**	**103.357**	**118.930**
(119979) 2002 WC$_{19}$, *pro.*	0.84427	0.010	79.218	4132	0.2208	23.712	136.709	121.284	359.573	0.0143	58.997	160.318
(119979) 2002 WC$_{19}$, *retro.*	0.21941	0.009	73.095	4023	0.2419	162.290	169.630	243.760	343.458	0.0235	157.775	85.412
(120347) Salacia-Actaea	**0.00028**	**0.011**	**498.199**	**5746**	**0.0052**	**17.512**	**276.631**	**110.476**	**273.107**	**0.0195**	**109.417**	**306.670**
(123509) 2000 WK$_{183}$, *blended*	0.40756	0.003	1.130	2388	0.0114	98.754	168.892	151.805	296.359	0.4792	109.633	275.744
(134860) 2000 OJ$_{67}$, *blended*	0.96827	0.002	1.877	2257	0.0358	81.435	151.329	257.076	27.989	0.0145	81.781	12.101
(148780) Altjira	**0.01624**	**0.001**	**4.003**	**9950**	**0.3474**	**25.176**	**191.938**	**274.506**	**123.690**	**0.4787**	**159.051**	**187.387**
(160091) 2000 OL$_{67}$, *pro.*	0.99577	0.005	0.2850	7563	0.232	85.499	37.090	226.364	87.724	0.0311	86.771	291.541
(160091) 2000 OL$_{67}$, *retro.*	1.01109	0.004	0.308	7757	0.2169	85.271	40.593	288.921	84.932	0.0298	114.926	248.907
(160256) 2002 PD$_{149}$	0.81370	0.008	0.550	26907	0.5907	26.377	143.969	96.259	172.878	1.0548	67.386	97.583
(174567) Varda-Ilmarë, *pro.*	**0.02790**	**0.004**	**266.803**	**4808**	**0.0119**	**63.392**	**296.882**	**313.943**	**171.285**	**0.0702**	**127.958**	**297.209**
(174567) Varda-Ilmarë, *retro.*	0.13531	0.005	267.863	4817	0.0178	79.784	309.956	2.040	142.580	0.2404	115.840	274.627
(225088) Gonggong-Xiangliu, *pro.*	**0.00620**	**0.003**	**1767.826**	**24206**	**0.2988**	**61.563**	**65.191**	**38.064**	**94.381**	**0.0841**	**108.045**	**73.731**
(225088) Gonggong-Xiangliu, *retro.*	0.24885	0.003	1758.133	24163	0.2958	121.773	67.608	88.035	95.070	0.1414	167.678	265.320
(229762) Gǃkúnǁ'hòmdímà-Gǃò'é ǃhú	0.59484	0.016	136.330	6038	0.0221	55.209	308.304	127.772	258.865	0.0109	82.470	289.514
(275809) 2001 QY$_{297}$	1.01557	0.0004	4.113	9965	0.4174	160.987	316.890	15.553	181.453	0.0018	161.279	68.401
(341520) Mors-Somnus	0.97259	0.023	0.745	20644	0.1568	15.623	320.190	331.366	294.476	0.1022	155.097	235.952
(364171) 2006 JZ$_{81}$	0.95893	0.047	1.291	33008	0.8478	12.746	170.621	81.052	75.688	0.4006	162.322	333.048
(385446) Manwë-Thorondor	0.66357	0.011	1.932	6663	0.5646	48.480	78.514	170.743	235.848	0.2750	77.739	92.703

Table A2 *continued*

Table A2 (*continued*)

Object	$\frac{\mathcal{L}_K}{\mathcal{L}_{NK}}$	Residual (arcsec)	M_{sys} (10^{18} kg)	a (km)	e	i (°)	ω (°)	Ω (°)	$\mathcal{M}$ (°)	J_2	i_{sp} (°)	Ω_{sp} (°)
(469705) ‡Kǎgára-Iháunu	0.73924	0.010	2.110	7587	0.6885	10.272	170.258	13.072	312.525	0.2921	162.551	82.769
(508788) 2000 CQ$_{114}$	0.95243	0.001	0.542	6928	0.0963	44.124	334.453	132.858	308.338	0.3054	89.798	333.487
(508869) 2002 VT$_{130}$, *pro.*	0.60596	0.002	2.313	3023	0.0144	65.104	33.765	129.898	272.126	0.1159	103.309	85.782
(508869) 2002 VT$_{130}$, *retro.*	0.25955	0.002	2.381	3052	0.0226	111.519	9.521	197.281	296.199	0.2488	105.822	119.414
(524366) 2001 XR$_{254}$	0.86142	0.002	4.071	9323	0.5547	20.099	287.158	321.814	265.548	0.3499	166.597	11.987
(524531) 2002 XH$_{91}$	0.86499	0.008	7.519	23567	0.7373	32.289	195.870	242.551	203.976	0.4515	125.906	90.043
(525462) 2005 EO$_{304}$	0.20246	0.054	2.125	69573	0.2148	13.212	209.267	258.120	184.769	2.7635	142.351	296.259
(612095) 1999 OJ$_4$	0.93881	0.010	0.406	3309	0.3671	54.519	82.718	259.123	67.569	0.2666	64.583	140.452
(612147) 2000 CF$_{105}$	0.86019	0.050	0.186	33379	0.2952	167.561	296.256	224.185	262.300	3.8540	127.820	221.565
(612176) 2000 QL$_{251}$	0.77542	0.002	3.111	4997	0.4885	132.000	12.407	89.402	353.609	0.2289	102.649	151.539
(612239) 2001 QC$_{298}$	0.37771	0.002	11.924	3818	0.3357	54.928	207.807	96.128	355.324	0.0592	30.340	104.721
(612687) 2003 UN$_{284}$	1.01884	0.076	1.273	53264	0.3736	25.629	168.468	93.554	290.990	0.2812	96.227	7.402
1998 WW$_{31}$	0.64207	0.008	2.682	22668	0.8164	48.109	221.621	116.717	42.893	0.4753	99.194	347.466
1999 RT$_{214}$	**0.03836**	**0.003**	**0.202**	**3441**	**0.2893**	**24.819**	**71.483**	**79.721**	**331.771**	**0.4357**	**131.628**	**180.017**
2001 QW$_{322}$	0.99997	0.092	2.033	103653	0.4592	150.778	251.286	241.500	164.669	0.0538	114.421	153.147
2003 QY$_{90}$	0.96631	0.016	0.516	8542	0.6596	54.590	146.471	131.557	26.008	0.3543	125.041	151.681
2003 TJ$_{58}$	0.88836	0.002	0.240	3856	0.5186	61.075	254.512	193.323	333.211	0.4378	149.733	168.308
2004 PB$_{108}$	0.95583	0.001	9.379	10363	0.4346	101.491	209.943	119.949	176.609	0.4518	138.515	297.249
2006 BR$_{284}$	0.10005	0.040	0.576	25359	0.2760	55.354	13.799	41.542	182.234	3.8250	139.757	54.153
2006 CH$_{69}$	0.77312	0.045	1.178	31089	0.9145	132.054	154.503	110.849	234.770	0.4294	128.997	96.168

Note.—All fitted angles are relative to the J2000 ecliptic plane. Residual indicates the combined RMS residual for the best fit. In our fits, we use $\ln J_2 R^2$ as our fitted parameter. Here, we present only the J_2 to enable comparison with the literature. For R, we use the volumetric radius of the modeled body (see Table 1). Bold-face data indicates TNBs that have significant detections of non-Keplerian motion.

REFERENCES

Acton Jr, C. H. 1996, Planetary and Space Science, 44, 65

Annex, A. M., Pearson, B., Seignovert, B., et al. 2020, Journal of Open Source Software, 5, 2050

Arakawa, S., Hyodo, R., Shoji, D., & Genda, H. 2021, The Astronomical Journal, 162, 226

Barr, A. C., & Schwamb, M. E. 2016, MNRAS, 460, 1542

Beauvalet, L., & Marchis, F. 2014, Icarus, 241, 13

Benecchi, S. D., Noll, K., Grundy, W., & Levison, H. 2010, Icarus, 207, 978

Benecchi, S. D., & Sheppard, S. S. 2013, The Astronomical Journal, 145, 124

Benecchi, S. D., Noll, K., Thirouin, A., et al. 2014, Icarus, 229, 423

Benedetti-Rossi, G., Sicardy, B., Buie, M. W., et al. 2016, The Astronomical Journal, 152, 156

Bierson, C. J., & Nimmo, F. 2019, Icarus, 326, 10

Brown, M., Ragozzine, D., Stansberry, J., & Fraser, W. 2010, The Astronomical Journal, 139, 2700

Brown, M. E. 2013, The Astrophysical Journal Letters, 778, L34

Brown, M. E., & Butler, B. J. 2017, The Astronomical Journal, 154, 19

—. 2018, The Astronomical Journal, 156, 164

Brown, M. E., & Schaller, E. L. 2007, Science, 316, 1585

Brož, M., Marchis, F., Jorda, L., et al. 2021, Astronomy & Astrophysics, 653, A56

Brunini, A., & López, M. C. 2020, Monthly Notices of the Royal Astronomical Society, 499, 4206

Campbell, H. M., Stone, L. R., & Kaib, N. A. 2022, The Astronomical Journal, 165, 19

Correia, A. C. 2018, Icarus, 305, 250

Dotto, E., Perna, D., Barucci, M. A., et al. 2008, Astronomy & Astrophysics, 490, 829

Duffard, R., Ortiz, J., Thirouin, A., Santos-Sanz, P., & Morales, N. 2009, Astronomy & Astrophysics, 505, 1283

Duffard, R., Pinilla-Alonso, N., Ortiz, J., et al. 2014, Astronomy & Astrophysics, 568, A79

Elliot, J. L., Person, M. J., Zuluaga, C., et al. 2010, Nature, 465, 897

Emelyanov, N. V., & Drozdov, A. E. 2020, MNRAS, 494, 2410

Fang, J., Margot, J.-L., Brozovic, M., et al. 2011, The Astronomical Journal, 141, 154

Fang, J., Margot, J.-L., & Rojo, P. 2012, The Astronomical Journal, 144, 70

Foreman-Mackey, D., Hogg, D. W., Lang, D., & Goodman, J. 2013, Publications of the Astronomical Society of the Pacific, 125, 306

Foreman-Mackey, D., et al. 2016, J. Open Source Softw., 1, 24

Foreman-Mackey, D., Farr, W. M., Sinha, M., et al. 2019, arXiv preprint arXiv:1911.07688

Fornasier, S., Lellouch, E., Müller, T., et al. 2013, Astronomy & Astrophysics, 555, A15

Fraser, W. C., & Brown, M. E. 2010, The Astrophysical Journal, 714, 1547

Ginsburg, A., Sipőcz, B. M., Brasseur, C., et al. 2019, The Astronomical Journal, 157, 98

Gourgeot, F., Carry, B., Dumas, C., et al. 2016, Astronomy & Astrophysics, 593, A19

Grundy, W., Benecchi, S., Porter, S., & Noll, K. 2014, Icarus, 237, 1

Grundy, W., Noll, K., Buie, M., et al. 2009, Icarus, 200, 627

Grundy, W., Noll, K., Virtanen, J., et al. 2008, Icarus, 197, 260

Grundy, W., Noll, K., Nimmo, F., et al. 2011, Icarus, 213, 678

Grundy, W., Benecchi, S., Rabinowitz, D., et al. 2012, Icarus, 220, 74

Grundy, W., Noll, K., Roe, H., et al. 2019, Icarus, 334, 62

Grundy, W. M., Noll, K. S., Buie, M. W., et al. 2019, Icarus, 334, 30

Grundy, W. M., Stansberry, J. A., Noll, K. S., et al. 2007, Icarus, 191, 286

Harris, A., & Warner, B. D. 2020, Icarus, 339, 113602

Hastings, D. M., Ragozzine, D., Fabrycky, D. C., et al. 2016, The Astronomical Journal, 152, 195

Holler, B. J., Grundy, W. M., Buie, M. W., & Noll, K. S. 2021, Icarus, 355, 114130

Hou, F., Goodman, J., Hogg, D. W., Weare, J., & Schwab, C. 2012, The Astrophysical Journal, 745, 198

Kecskeméthy, V., Kiss, C., Szakáts, R., et al. 2023, The Astrophysical Journal Supplement Series, 264, 18

Kern, S. D. 2006, PhD thesis, Massachusetts Institute of Technology

Kiss, C., Marton, G., Farkas-Takács, A., et al. 2017, The Astrophysical Journal Letters, 838, L1

Kiss, C., Marton, G., Parker, A. H., et al. 2019, Icarus, 334, 3

Leiva, R., Buie, M. W., Keller, J. M., et al. 2020, The Planetary Science Journal, 1, 48

Lellouch, E., Santos-Sanz, P., Lacerda, P., et al. 2013, Astronomy & Astrophysics, 557, A60

Marchis, F., Descamps, P., Hestroffer, D., & Berthier, J. 2005a, Nature, 436, 822

Marchis, F., Hestroffer, D., Descamps, P., et al. 2005b, Icarus, 178, 450

Marchis, F., Durech, J., Castillo-Rogez, J., et al. 2014, The Astrophysical journal letters, 783, L37

McKinnon, W., Richardson, D., Marohnic, J., et al. 2020, Science, 367, eaay6620

Mommert, M. 2013, PhD thesis

Nesvornỳ, D., Li, R., Simon, J. B., et al. 2021, The Planetary Science Journal, 2, 27

Nesvornỳ, D., Li, R., Youdin, A. N., Simon, J. B., & Grundy, W. M. 2019, Nature Astronomy, 3, 808

Nesvornỳ, D., Youdin, A. N., & Richardson, D. C. 2010, The Astronomical Journal, 140, 785

Ortiz, J. L., Santos-Sanz, P., Sicardy, B., et al. 2017, Nature, 550, 219

Osip, D. J., Kern, S., & Elliot, J. 2003, Earth, Moon, and Planets, 92, 409

Pál, A., Kiss, C., Müller, T. G., et al. 2016, The Astronomical Journal, 151, 117

Parker, A. H., & Kavelaars, J. 2011, The Astrophysical Journal, 744, 139

Parker, A. H., Kavelaars, J., Petit, J.-M., et al. 2011, The Astrophysical Journal, 743, 1

Porter, S. B., & Grundy, W. M. 2012, Icarus, 220, 947

Proudfoot, B., & Ragozzine, D. 2021in , 107–10

Proudfoot, B. C., & Ragozzine, D. 2019, The Astronomical Journal, 157, 230

Rabinowitz, D. L., Benecchi, S. D., Grundy, W. M., & Verbiscer, A. J. 2014, Icarus, 236, 72

Rabinowitz, D. L., Benecchi, S. D., Grundy, W. M., Verbiscer, A. J., & Thirouin, A. 2019, The Astronomical Journal, 159, 27

Rabinowitz, D. L., Schaefer, B. E., & Tourtellotte, S. W. 2006, The Astronomical Journal, 133, 26

Ragozzine, D., & Brown, M. E. 2009, AJ, 137, 4766

Ragozzine, D., Pincock, S., Proudfoot, B. C. N., et al. 2023, in prep.

Robinson, J. E., Fraser, W. C., Fitzsimmons, A., & Lacerda, P. 2020, Astronomy & Astrophysics, 643, A55

Rousselot, P., Petit, J.-M., Poulet, F., & Sergeev, A. 2005, Icarus, 176, 478

Santos-Sanz, P., Lellouch, E., Fornasier, S., et al. 2012, Astronomy & Astrophysics, 541, A92

Scheeres, D., Williams, B. G., & Miller, J. K. 2000, Journal of Guidance, Control, and Dynamics, 23, 466

Schindler, K., Wolf, J., Bardecker, J., et al. 2017, Astronomy & Astrophysics, 600, A12

Sheppard, S. S., & Jewitt, D. 2004, The Astronomical Journal, 127, 3023

Sheppard, S. S., Ragozzine, D., & Trujillo, C. 2012, The Astronomical Journal, 143, 58

Showalter, M. R., Benecchi, S. D., Buie, M. W., et al. 2021, Icarus, 356, 114098

Sickafoose, A., Bosh, A., Levine, S., et al. 2019, Icarus, 319, 657

Spencer, J. R., Stansberry, J., Grundy, W., & Noll, K. 2006, in AAS/Division for Planetary Sciences Meeting Abstracts# 38, Vol. 38, 34–01

Stansberry, J., Grundy, W., Brown, M., et al. 2008, The Solar System Beyond Neptune, 161

Stern, S., Weaver, H., Spencer, J., et al. 2019, Science, 364, eaaw9771

Tegler, S. C., Romanishin, W., Consolmagno, G., et al. 2005, Icarus, 175, 390

Thirouin, A., Noll, K. S., Ortiz, J., & Morales, N. 2014, Astronomy & Astrophysics, 569, A3

Thirouin, A., Ortiz, J., Campo Bagatin, A., et al. 2012, Monthly Notices of the Royal Astronomical Society, 424, 3156

Thirouin, A., & Sheppard, S. S. 2018, The Astronomical Journal, 155, 248

—. 2019, The Astronomical Journal, 157, 228

Vachier, F., Berthier, J., & Marchis, F. 2012, Astronomy & Astrophysics, 543, A68

Veillet, C., Parker, J. W., Griffin, I., et al. 2002, Nature, 416, 711

Vilenius, E., Kiss, C., Mommert, M., et al. 2012, Astronomy & Astrophysics, 541, A94

Vilenius, E., Kiss, C., Müller, T., et al. 2014, Astronomy & Astrophysics, 564, A35

Weaver, H., Porter, S., Spencer, J., Team, N. H. S., et al. 2022, The Planetary Science Journal, 3, 46

Yoder, C. F. 1995, 1

Chapter 4

Beyond Point Masses III: Detecting Haumea's Nonspherical Gravitational Field

The content of this chapter has been submitted to The Planetary Science Journal. The version below is a preprint version in journal specific style.

Beyond Point Masses III: Detecting Haumea's Nonspherical Gravitational Field

BENJAMIN C.N. PROUDFOOT,[1] DARIN A. RAGOZZINE,[1] WILLIAM GIFOROS,[1] WILL M. GRUNDY,[2, 3] MARIAH MACDONALD,[4] AND WILLIAM J. OLDROYD[3]

[1] *Brigham Young University, Department of Physics & Astronomy, N283 ESC, Brigham Young University, Provo, UT 84602, USA*
[2] *Lowell Observatory, 1400 W Mars Hill Rd, Flagstaff, AZ 86001, USA*
[3] *Northern Arizona University, Department of Astronomy & Planetary Science, PO Box 6010, Flagstaff, AZ 86011, USA*
[4] *The College of New Jersey, NJ, USA*

ABSTRACT

The dwarf planet Haumea is one of the most compelling transneptunian objects (TNOs) to study, hosting two small, dynamically interacting satellites, a family of nearby spectrally unique objects, and a ring system. Haumea itself is extremely oblate due to its 3.9 hour rotation period. Understanding the orbits of Haumea's satellites, named Hi'iaka and Namaka, requires detailed modeling of both satellite-satellite gravitational interactions and satellite interactions with Haumea's nonspherical gravitational field (parameterized here as J_2). Understanding both of these effects allows for a detailed probe of the satellites' masses and Haumea's J_2 and spin pole. Measuring Haumea's J_2 provides information about Haumea's interior, possibly determining the extent of past differentation. In an effort to understand the Haumea system, we have performed detailed non-Keplerian orbit fitting of the Haumea's satellites Hi'iska and Namaka using a decade of ultra-precise observations. Our fits strongly detect Haumea's J_2 and spin pole at $\gtrsim 2.5\sigma$ confidence. Degeneracies present in the dynamics prevent us from precisely measuring Haumea's J_2 with the current data, but future observations should enable a precise measurement. Our dynamically determined spin pole shows excellent agreement with past results, illustrating the strength of non-Keplerian orbit fitting. We also explore the spin-orbit dynamics of Haumea and its satellites, showing that axial precession of Hi'iaka may be detectable over decadal timescales. Finally, we present an ephemeris of the Haumea system over the coming decade, enabling high-quality observations of Haumea and its satellites for years to come.

1. INTRODUCTION

Almost all of the largest transneptunian objects (TNOs) are known to host satellites (e.g. Christy & Harrington 1978; Brown et al. 2005, 2006; Brown & Suer 2007; Noll et al. 2007; Parker et al. 2016; Kiss et al. 2017). These satellites are generally small relative to the system primary, and are thought to have formed by collisions (Barr & Schwamb 2016; Arakawa et al. 2019). The current density of the transneptunian region is far too low to have formed so many satellites by collision (Campo Bagatin & Benavidez 2012; Abedin et al. 2022), implying that these systems must not have formed insitu. The emerging consensus is that large TNOs formed in a relatively massive primordial disk exterior to the giant planets, which was subsequently scattered by Neptune's outwards migration (Nesvorný 2018; Gladman & Volk 2021). The large TNOs we see today, which are on excited orbits, are the remnants of this primordial disk. By understanding the satellites of large TNOs, how they formed, and how they evolve, we can probe the conditions of the early primordial disk where these systems formed.

(136108) Haumea (2003 EL61), the third most massive TNO known, is host to two satellites: Hi'iaka on a $\sim$50 day orbit and Namaka on a $\sim$20 day orbit (Brown et al. 2005, 2006). Haumea's satellites may have formed during a collision, which simultaneously spun up Haumea, created the satellites, and also formed Haumea's unique, icy collisional family (Leinhardt et al. 2010; Proudfoot & Ragozzine 2022), but there remains some disagreement on these circumstances (e.g., Ortiz et al. 2012; Campo Bagatin et al. 2016; Noviello et al. 2022). Despite many proposals, connecting a formation model to all of the system's unique characteristics has been difficult (e.g., Proudfoot & Ragozzine 2019).

Corresponding author: Benjamin Proudfoot
benp175@gmail.com

Our understanding of the complex nature of the Haumea system can be advanced by detailed study of the satellites' orbits. Study of the orbits potentially allows for a measurement of the masses of each component, as the two satellites strongly interact with each other (Ragozzine & Brown 2009, hereafter RB09). In addition to satellite-satellite interactions, interactions with Haumea's nonspherical gravitational potential from its highly elongated shape (due to rapid rotation). Haumea's gravitational potential is determined both by its shape and internal density distribution. Since Haumea's shape is fairly well known (due to observations of a stellar occultation, see Ortiz et al. 2017), measuring the gravitational harmonics of Haumea may allow us to constrain its internal density distribution. The internal density distributions of TNOs are almost completely unconstrained, although large TNOs are expected to be differentiated (McKinnon et al. 2008; Dunham et al. 2019).

Haumea, in particular, has evidence for differentiation in the form of the collisional family. Haumea's family members are spectroscopically unique showing strong water ice features and no other major constituents (Souza Feliciano et al., in prep.). In combination with very high albedos (Elliot et al. 2010; Vilenius et al. 2014), it seems like the family members could be made of pure water ice. This would suggest that the proto-Haumea was a differentiated "ocean world" and that Haumea family members are pieces of the water ice mantle. The implication is that studying present-day Haumea gives us unique insight into the interiors of ocean worlds.

Haumea's gravitational potential is described by a spherical harmonic expansion. To quadrupole order, the gravitational field of Haumea, U, with mass, M, at a distance r can be written as:

$$U(r, \theta, \phi) = -\frac{GM}{r} \left[1 - J_2 \left(\frac{R}{r}\right)^2 \left(\frac{3}{2}\sin^2\theta - \frac{1}{2}\right) \right. \\ \left. + C_{22} \left(\frac{R}{r}\right)^2 \cos^2\theta \sin 2\phi + \mathcal{O}\left(r^{-3}\right) \right] \quad (1)$$

where J_2 and C_{22} are the second-order gravitational harmonic coefficients, θ is the body-fixed latitude angle, ϕ is the body-fixed longitude angle, and R is an "reference" radius (Yoder 1995; Scheeres et al. 2000). In this work, we assume that R is equivalent to volumetric radius. The coefficients J_2 and C_{22} describe Haumea's shape and internal density structure. Taking the shape found by Ortiz et al. (2017) and assuming a homogeneous density, Haumea is expected to have $J_2 = 0.24$ and $C_{22} = 0.05$. However, when taking differentia-

tion into account and using the Dunham et al. (2019) model of Haumea's interior, these harmonics would be $J_2 = 0.16$ and $C_{22} = 0.03$. While both of these models are simplified, they serve as a useful guide.

In the original work that determined the orbits of Haumea's satellites (RB09), Haumea's nonspherical gravitational field was not clearly detected, although they were able to robustly detect satellite-satellite interactions. Subsequent follow up studies have also been unsuccessful in detecting the nonspherical field (Gourgeot et al. 2016). However, with new ultra-precise HST observations from the past decade, another analysis of the satellites' orbits is in order. By leveraging these observations, as well as new computational techniques, we present a new, updated set of orbital fits to the Haumea system. We are able to detect the nonspherical gravitational potential of Haumea, constrain the masses of Haumea's satellites, and study the spin-orbit evolution of the system. The paper will proceed as follows. In Section 2, we describe the observations used in our analysis. Then in Section 3, we describe our non-Keplerian orbital model and fitting procedure. Results of the fitting are presented in Section 4, and discussed in Section 5. We then conclude in Section 6 and discuss future work.

2. OBSERVATIONS AND DATA ANALYSIS

The data we use in our orbit fitting comes from a variety of sources, but can be broadly broken into three separate groups. The first dataset comes directly from RB09, which extracted satellite positions from Keck and HST observations. The second dataset consists of HST observations from HST Programs 12243 and 13873. The last dataset is made up of Keck observations from 2020-2022. For our orbit fitting, we combined the relative astrometry from each data set and simultaneously fit all the data. Our compiled data is presented in Table 1.

The published astrometry from RB09 was found to have a sign error in their listed RA offsets (in their Table 1). This error can be seen in their Figure 1 as RA decreases towards the east, opposite to convention. This mistake affected their orbital modeling, preventing them from correctly determining the orbital plane of the system, although the rest of their analysis is relatively unaffected. In our analysis, we use the RB09 data, although we correct the error and use the mirrored RA values.

HST Programs 12243 and 13873 used HST's Wide Field Camera 3 (WFC3) to observe the Haumea system with a combined 13 orbits of coverage. Program 12243 imaged the system, using 10 consecutive HST orbits, in an attempt to observe a Haumea-Namaka mutual event. Program 13873 used 3 single-orbit visits to measure satellite relative astrometry to better constrain

orbit models. Both of these programs took ∼30 individual exposures per orbit, using the F350LP filter to maximize signal-to-noise. The images from these programs were analyzed using the same method used in RB09, although changes were made to fit the WFC3 data, replacing the older cameras used in previous programs.

Keck observations used the laser guide star adaptive optics system (LGS AO) (Wizinowich et al. 2006) with the narrow camera of NIRC2 (https://www2.keck.hawaii.edu/inst/nirc2). In the 2020 and 2021 observations, nearby field stars were used for tip-tilt correction, since they were brighter than Haumea. All Keck observations were done in the infrared H filter, covering wavelengths from ∼1.48 to 1.77 μm, with a series of dithered exposures for sky subtraction and to minimize the effect of bad pixels.

To extract relative astrometry of the satellites from the Keck data, we simultaneously fit 2-dimensional Gaussian PSFs to each object in individual images. While a Gaussian is a relatively poor approximation for the NIRC2 PSF, it is still able to measure the center of each PSF quite accurately. Relative detector positions were then converted to relative right ascension and declination assuming a mean plate scale of 9.952 mas/pixel and an orientation offset of 0.252° (Konopacky et al. 2010; Yelda et al. 2010; Service et al. 2016). The median and standard deviation offsets of individual measurements are used for the astrometric offsets and error for each night, although we implemented a conservative noise floor of 10 milliarcseconds to account for unknown systematics. This method has been extensively used to extract relative astrometry from Keck NIRC2 images (e.g. Grundy et al. 2015).

As can be seen in Table 1, both satellites are not always detected at each epoch either due to lack of angular resolution when the satellite is close to Haumea or insufficient exposure time. In principle, non-detections can be used to help constrain the satellites' orbits, but in practice, given the already well-known orbits, they barely constrain the fits. Hence, during our orbit fitting process, we do not use non-detections in any way.

3. METHODS

For our orbit fitting, we use MultiMoon, a state-of-the-art orbit fitter designed for use with TNOs (Ragozzine et al., submitted). MultiMoon is built around an n-quadrupole integrator that can simulate the gravitational interactions of an arbitrary number of quadrupoles. Internally, it uses emcee (Foreman-Mackey et al. 2013, 2019), a popular Markov chain

Monte Carlo (MCMC) ensemble sampler, allowing us to treat the orbit fit as a Bayesian inference problem. In its simplest form, MultiMoon uses a least squares method for evaluating the goodness-of-fit of a given orbital model, although it can accommodate a more complicated goodness-of-fit metric, which we describe later in this paper.

In our fits, we only consider the J_2 and no other gravitational harmonics since it is by far the most dominant harmonic. The other second order harmonic, C_{22} which is related to the prolateness of Haumea, is relevant for understanding dynamics of orbits around Haumea, but only within a few times the corotation radius (Proudfoot & Ragozzine 2021). Even within this range, C_{22} averages out over many orbits except when close to a spin-orbit resonance (SOR). Haumea also certainly has substantial higher-order harmonics (most notably J_4), but their effect is small due to the r^{-5} distance dependence of the next level of harmonics. As further justification of this assumption, we can analytically estimate the precession induced by Haumea's J_4, and find it is only ∼0.1% the strength of J_2 precession for Namaka, and even smaller for Hi'iaka. Thus we believe that our simple model of Haumea's gravitational potential is sufficient to describe the dynamics taking place in the Haumea system.

For the orbit fits presented here, we only model the gravitational harmonics of Haumea, ignoring the (presumably) nonspherical shapes of Hi'iaka and Namaka, although we do revisit this assumption later. With this in mind, our baseline orbit model has 18 free parameters, including the mass, J_2, and 2 spin pole direction angles of Haumea, as well as the masses and 6 orbital elements of both Hi'iaka and Namaka. In addition to these 18 free parameters, our model requires the input of Haumea's rotational period, to correctly model any axial precession which the satellites may cause. Although this value could, in principle, be a free parameter in the model, it is known with high precision and has very little influence on the orbital dynamics of the system. Hence we opt to use a fixed value of 3.915 hours (Rabinowitz et al. 2006).

To account for possible systematics arising from the use of a variety of data sets, we have implemented a sophisticated likelihood function within MultiMoon. This likelihood function is adapted from the outlier pruning methods presented in Hogg et al. (2010). Since we, *a priori*, do not describe the systematic errors that may arise in the fitting process, we use an extremely flexible framework. Our likelihood model is a mixture model that combines two least-squares terms. The first is a common least-squares likelihood model, the standard technique

4   Proudfoot et al.

Table 1. Observed Astrometric Positions of Haumea's Satellites

Julian Date	Date	Telescope	Camera	Δx_N (")	Δy_N (")	$\sigma_{\Delta x_N}$ (")	$\sigma_{\Delta y_N}$ (")	Δx_H (")	Δy_H (")	$\sigma_{\Delta x_H}$ (")	$\sigma_{\Delta y_H}$ (")
2453397.162	2005 Jan 26	Keck	NIRC2	$\cdots$	$\cdots$	$\cdots$	$\cdots$	-0.03506	-0.63055	0.01394	0.01394
2453431.009	2005 Mar 1	Keck	NIRC2	-0.00992	0.52801	0.02986	0.02986	-0.29390	-1.00626	0.02291	0.02291
2453433.984	2005 Mar 4	Keck	NIRC2	$\cdots$	$\cdots$	$\cdots$	$\cdots$	-0.33974	-1.26530	0.01992	0.01992
2453518.816	2005 May 28	Keck	NIRC2	$\cdots$	$\cdots$	$\cdots$	$\cdots$	0.06226	0.60575	0.00996	0.00996
2453551.810	2005 Jun 30	Keck	NIRC2	0.03988	-0.65739	0.03978	0.03978	0.19727	0.52106	0.00498	0.00996
2453746.525	2006 Jan 11	HST	ACS/HRC	-0.04134	-0.18746	0.00267	0.00267	0.20637	0.30013	0.00256	0.00256
2453746.554	2006 Jan 11	HST	ACS/HRC	-0.03867	-0.19174	0.00267	0.00267	0.20832	0.30582	0.00257	0.00257
2454138.287	2007 Feb 6	HST	WFPC2	0.02627	-0.57004	0.00702	0.00351	0.21088	0.22019	0.00252	0.00197
2454138.304	2007 Feb 6	HST	WFPC2	0.03107	-0.56624	0.00210	0.00782	0.21132	0.22145	0.00095	0.00204
2454138.351	2007 Feb 6	HST	WFPC2	0.03009	-0.55811	0.00527	0.00564	0.21515	0.23185	0.00301	0.00206
2454138.368	2007 Feb 6	HST	WFPC2	0.03133	-0.56000	0.00482	0.00663	0.21402	0.23314	0.00192	0.00230
2454138.418	2007 Feb 6	HST	WFPC2	0.03134	-0.54559	0.00385	0.00376	0.21705	0.24202	0.00103	0.00282
2454138.435	2007 Feb 6	HST	WFPC2	0.02791	-0.54794	0.00571	0.00524	0.21449	0.24450	0.00323	0.00254
2454138.484	2007 Feb 6	HST	WFPC2	0.02972	-0.53385	0.00797	0.01330	0.21818	0.25301	0.00153	0.00224
2454138.501	2007 Feb 7	HST	WFPC2	0.03226	-0.53727	0.00531	0.00400	0.21807	0.25639	0.00310	0.00291
2454138.551	2007 Feb 7	HST	WFPC2	0.03429	-0.53079	0.00497	0.00582	0.22173	0.26308	0.00146	0.00230
2454138.567	2007 Feb 7	HST	WFPC2	0.03576	-0.52712	0.00270	0.00479	0.21978	0.26791	0.00202	0.00226
2454469.653	2008 Jan 4	HST	WFPC2	0.02399	-0.28555	0.00670	0.00831	-0.23786	-1.27383	0.00404	0.00824
2454552.897	2008 Mar 27	Keck	NIRC2	$\cdots$	$\cdots$	$\cdots$	$\cdots$	-0.19974	-0.10941	0.00930	0.00956
2454556.929	2008 Mar 31	Keck	NIRC2	-0.00439	-0.76848	0.01239	0.01280	-0.32988	-0.77111	0.00455	0.00557
2454556.948	2008 Mar 31	Keck	NIRC2	-0.01363	-0.76500	0.01976	0.01252	-0.33367	-0.77427	0.00890	0.00753
2454556.964	2008 Mar 31	Keck	NIRC2	-0.00576	-0.77375	0.01212	0.01283	-0.33267	-0.77874	0.00676	0.00485
2454557.004	2008 Mar 31	Keck	NIRC2	-0.00854	-0.77313	0.01199	0.00897	-0.33543	-0.78372	0.00404	0.00592
2454557.020	2008 Mar 31	Keck	NIRC2	-0.00075	-0.76974	0.00907	0.01015	-0.33491	-0.78368	0.00374	0.00473
2454557.039	2008 Mar 31	Keck	NIRC2	-0.00988	-0.77084	0.01793	0.01543	-0.33712	-0.78464	0.00740	0.00936
2454557.058	2008 Mar 31	Keck	NIRC2	-0.01533	-0.76117	0.00765	0.01571	-0.33549	-0.78692	0.00868	0.00852
2454557.074	2008 Mar 31	Keck	NIRC2	-0.00645	-0.76297	0.01639	0.01390	-0.33128	-0.78867	0.01431	0.01411
2454557.091	2008 Mar 31	Keck	NIRC2	-0.00708	-0.76986	0.01532	0.00787	-0.33687	-0.79462	0.00803	0.00717
2454593.726	2008 May 7	HST	NICMOS	-0.00243	-0.75878	0.00576	0.00761	0.18297	1.08994	0.00354	0.00425
2454600.192	2008 May 13	HST	WFPC2	0.02325	0.19934	0.00480	0.01161	-0.10847	0.17074	0.00508	0.00427
2454601.990	2008 May 15	HST	WFPC2	0.02293	0.50217	0.00618	0.00614	-0.18374	-0.13041	0.00729	0.00504
2454603.788	2008 May 17	HST	WFPC2	0.01174	0.59613	0.00366	0.00485	-0.24918	-0.43962	0.00207	0.00574
2454605.788	2008 May 19	HST	WFPC2	-0.00006	0.29915	0.00425	0.00613	-0.29818	-0.75412	0.00467	0.00966
2455375.655	2010 Jun 28	HST	WFC3	0.00735	0.19620	0.00168	0.00161	$\cdots$	$\cdots$	$\cdots$	$\cdots$
2455375.661	2010 Jun 28	HST	WFC3	$\cdots$	$\cdots$	$\cdots$	$\cdots$	0.26874	1.22502	0.00159	0.00154
2455375.673	2010 Jun 28	HST	WFC3	0.00766	0.18829	0.00326	0.00336	$\cdots$	$\cdots$	$\cdots$	$\cdots$
2455375.719	2010 Jun 28	HST	WFC3	0.00729	0.18426	0.00202	0.00778	$\cdots$	$\cdots$	$\cdots$	$\cdots$
2455375.727	2010 Jun 28	HST	WFC3	$\cdots$	$\cdots$	$\cdots$	$\cdots$	0.26632	1.22294	0.00126	0.00164
2455375.737	2010 Jun 28	HST	WFC3	0.00612	0.17861	0.00170	0.00252	$\cdots$	$\cdots$	$\cdots$	$\cdots$
2455375.786	2010 Jun 28	HST	WFC3	0.00926	0.16304	0.00144	0.00274	$\cdots$	$\cdots$	$\cdots$	$\cdots$
2455375.793	2010 Jun 28	HST	WFC3	$\cdots$	$\cdots$	$\cdots$	$\cdots$	0.26374	1.22053	0.00138	0.00193
2455375.859	2010 Jun 28	HST	WFC3	$\cdots$	$\cdots$	$\cdots$	$\cdots$	0.26187	1.21840	0.00131	0.00182
2455375.928	2010 Jun 28	HST	WFC3	$\cdots$	$\cdots$	$\cdots$	$\cdots$	0.25945	1.21625	0.00150	0.00175
2455375.993	2010 Jun 28	HST	WFC3	$\cdots$	$\cdots$	$\cdots$	$\cdots$	0.25813	1.21560	0.00137	0.00189
2455376.058	2010 Jun 28	HST	WFC3	$\cdots$	$\cdots$	$\cdots$	$\cdots$	0.25598	1.21306	0.00165	0.00136
2456995.589	2014 Dec 4	HST	WFC3	-0.04910	-0.34609	0.00200	0.00222	0.17725	1.13669	0.00200	0.00200
2457155.338	2015 May 12	HST	WFC3	-0.09964	-0.45547	0.00315	0.00433	-0.44571	-0.69806	0.00454	0.00568
2457203.995	2015 Jun 30	HST	WFC3	0.14931	0.69611	0.00200	0.00200	-0.42272	-0.63347	0.00200	0.00200
2458885.090	2020 Feb 5	Keck	NIRC2	0.21330	0.29118	0.01000	0.01000	-0.03064	-1.15403	0.01000	0.01000
2459272.041	2021 Feb 26	Keck	NIRC2	$\cdots$	$\cdots$	$\cdots$	$\cdots$	-0.37255	-1.36839	0.01000	0.01000
2459598.127	2022 Jan 18	Keck	NIRC2	$\cdots$	$\cdots$	$\cdots$	$\cdots$	-0.13988	0.80436	0.01000	0.01000

Note—The relative right ascension and declination positions of Haumea's satellites. At some epochs, Hi'iaka or Namaka were not visible in the images, for a variety of reasons. For these entries, no data is listed and our orbit fits were not constrained by their non-detection. Data from before 2010 are taken from Ragozzine & Brown (2009), although we correct their sign error in the Δx columns.

for orbit fitting. This term is combined with another least-squares model with an additional error term. The error term, which we call σ_{sys}, is combined with the measured uncertainties of our observations in quadrature. Also included is a normalization factor (f_{sys}) describing the fraction of data displaying systematic errors, which also acts as a penalty for exclusion of data. The entire likelihood function can be written:

$$\mathcal{L} = \prod_{i=1}^{N} \left[\left(\frac{1 - f_{sys}}{\sqrt{2\pi\sigma_i^2}} \right) \exp\left(-\frac{(y_i - y_{i,m})^2}{2\sigma_i^2} \right) \right. \tag{2}$$
$$\left. + \left(\frac{f_{sys}}{\sqrt{2\pi(\sigma_i^2 + \sigma_{sys}^2)}} \right) \exp\left(-\frac{(y_i - y_{i,m})^2}{2(\sigma_i^2 + \sigma_{sys}^2)} \right) \right]$$

where y_i and σ_i are the N observations and uncertainties, and $y_{i,m}$ is the model. Technically, $y_{i,m}$ and σ_i are vectors where each have two dimensions ($\Delta\alpha\cos\delta$, $\Delta\delta$) and there is an implied summation over both of these dimensions. For brevity, however, we exclude this summation, although it is implemented in its full form internally. If there are significant outliers in the data, this prescription downweights them relative to the typical least-squares assumptions and thus qualifies as a "robust" (to outliers) statistical method. In this sense, it operates similar to an automated sigma-clipping technique. It also allows for the expansion of systematic uncertainties when the quoted statistical uncertainties are too small to explain the scatter in residuals relative to the model.

The factors $(1 - f_{sys})$ and f_{sys} are critical for normalizing the two likelihood models and provide an implicit prior that penalizes overestimation of systematic effects. However, when $\sigma_{sys} \ll \sigma_i$ (i.e. there are no systematic errors present in the data), f_{sys} is not well defined as both likelihood functions asymptotically approach one another. To prevent this degeneracy from becoming problematic, we implement a prior forcing $\sigma_{sys} \geq 1$ milliarcsecond. This likelihood model adds an additional two free parameters to our model (σ_{sys}, f_{sys}). However, instead of fitting σ_{sys}, we opt to fit $\log_{10}\sigma_{sys}$, allowing the MCMC algorithm to more easily explore a greater range of values. This "robust" likelihood model has now been implemented into `MultiMoon` and is publicly available on GitHub[1]. We have extensively validated this likelihood model using synthetically produced data sets that have large systematics applied. We find that when using this model, `MultiMoon` can recover the original parameters even when systematic uncertainties of 10s of milliarcseconds are applied to ~50% of the data set.

During our data fitting process, we found that large systematics were present when combining both the Keck and HST data that necessitated the use of this robust likelihood model. Unfortunately, our model could not resolve these issues and unusual systematics remained unaccounted for. To remain as conservative as possible, we elected to complete an orbit fit using the HST data only with a standard least-squares likelihood model. We discuss the drawbacks of the HST+Keck fit further in Section 4 and 5.

As part of the Bayesian framework `MultiMoon` uses, we set priors for all parameters to be uninformative (except for σ_{sys} as discussed above), allowing the data to constrain the posterior distribution. However, in our HST only fit, we set priors on the spin pole direction of Haumea to prevent walkers from getting stuck in a lower dimensional subspace. The priors were chosen to bracket the best region of likelihood space within $\sim 10°$, as identified in preliminary fits. After the fit was completed, we confirmed that this prior did not significantly prevent walkers from exploring favorable parts of likelihood space.

We drew initial walker positions from Gaussian distributions centered near the location of highest likelihood that was identified in preliminary runs. These preliminary runs were conducted to broadly search parameter space and used very broad initial guesses, allowing for a rigorous search of the 18-dimensional parameter space (20-dimensional for the HST+Keck fits). Our preliminary fits showed no signs of other likelihood maxima with acceptable fit quality. Our baseline orbit fits used 960 walkers in the MCMC ensemble, which were run for 5000 burn-in steps. We then pruned underperforming walkers, replacing them with random linear combinations of highly performing walkers, after which the ensemble was run for 1000 more burn-in steps. The ensemble was then run for 20000 steps to sample the posterior distribution. We confirmed that the resulting chains were converged by visual inspection of walker trace plots and marginal parameter-likelihood plots.

4. RESULTS

When comparing our different orbit fits, we find that there is strong disagreement between the two datasets (HST+Keck and HST only). When fitting to the combined dataset, we find that the most recent Keck observations of the system are at odds with the 2014-2015 HST observations. Using our robust likelihood model and the combined HST+Keck dataset, we find that our best fit is $\sim 10\sigma$ inconsistent with the 2014 HST obser-
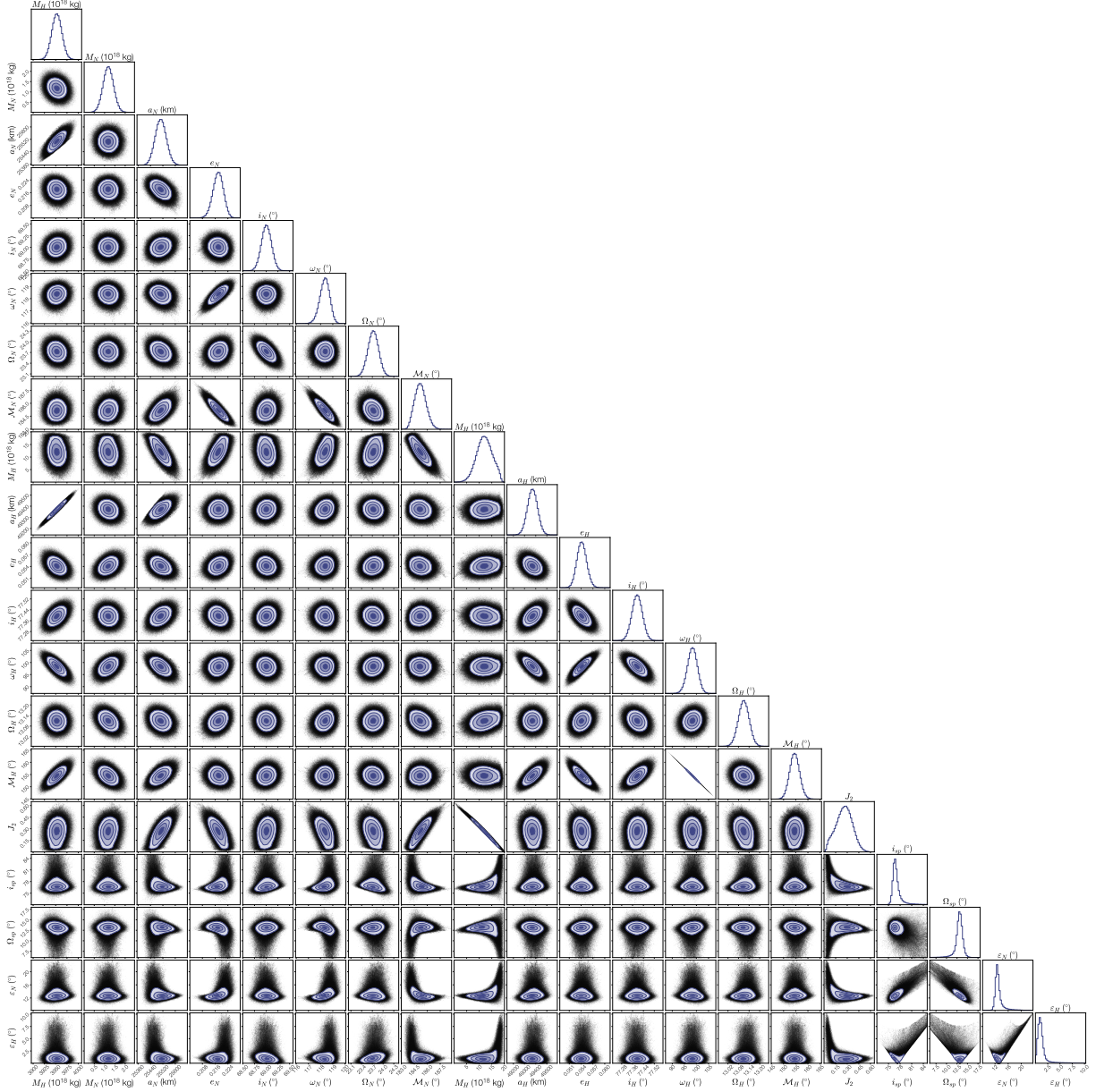
Figure 1. A corner plot for the HST only orbit fit to the Haumea system. We include all 18 fitted parameters along with 2 derived parameters. To facilitate easy interpretation, we list J_2 rather than $J_2 R^2$ by taking the volumetric radius R from the occultation derived shape model (Ortiz et al. 2017). We also show the inclinations of each satellite with respect to Haumea's equator in the last two columns. Along the top of each column is the marginal posterior distribution for each parameter in our fit. Below the marginal distributions are the 2-dimensional joint posterior distributions for every pair of parameters. Contours correspond to 1, 2, and 3σ levels. Small black points mark individual samples from our MCMC chains. The best fit parameter set in our MCMC chains corresponds to a χ^2 of 99.1 with 90 degrees of freedom. Of particular note is the strong exclusion of $J_2 = 0$ in the marginal posterior for Haumea's J_2, alongside strong correlations between J_2 and a variety of other parameters.

**Table 2.** Non-Keplerian Orbit Solutions for Haumea's Satellites

Parameter		HST only fit	HST+Keck fit
Fitted parameters			
Mass, Haumea (10^{18} kg)	M_P	$3952.44^{+11.09}_{-11.03}$	$3952.62^{+9.33}_{-9.09}$
Mass, Namaka (10^{18} kg)	M_N	$1.18^{+0.25}_{-0.25}$	$1.1^{+0.17}_{-0.18}$
Semi-major axis, Namaka (km)	a_N	25506^{+36}_{-36}	25548^{+27}_{-28}
Eccentricity, Namaka	e_N	$0.2179^{+0.0032}_{-0.0033}$	$0.2137^{+0.0042}_{-0.0043}$
Inclination, Namaka (°)	i_N	$69.005^{+0.108}_{-0.107}$	$69.048^{+0.103}_{-0.103}$
Argument of periapse, Namaka (°)	ω_N	$118.35^{+0.39}_{-0.42}$	$117.82^{+0.58}_{-0.60}$
Longitude of the ascending node, Namaka (°)	Ω_N	$23.725^{+0.149}_{-0.15}$	$23.606^{+0.162}_{-0.154}$
Mean anomaly at epoch, Namaka(°)	$\mathcal{M}_N$	$185.19^{+0.69}_{-0.65}$	$186.32^{+0.73}_{-0.70}$
Mass, Hi'iaka (10^{18} kg)	M_H	$12.13^{+3.22}_{-3.11}$	$6.65^{+1.67}_{-1.52}$
Semi-major axis, Hi'iaka (km)	a_H	49371^{+45}_{-45}	49352^{+37}_{-35}
Eccentricity, Hi'iaka	e_H	$0.0542^{+0.0012}_{-0.0012}$	$0.0545^{+0.0009}_{-0.0009}$
Inclination, Hi'iaka (°)	i_H	$77.394^{+0.038}_{-0.038}$	$77.376^{+0.035}_{-0.035}$
Argument of periapse, Hi'iaka (°)	ω_H	$98.34^{+2.02}_{-2.06}$	$99.05^{+1.48}_{-1.49}$
Longitude of the ascending node, Hi'iaka (°)	Ω_H	$13.11^{+0.030}_{-0.031}$	$13.071^{+0.030}_{-0.029}$
Mean anomaly at epoch, Hi'iaka (°)	$\mathcal{M}_H$	$154.53^{+2.05}_{-2.00}$	$153.88^{+1.48}_{-1.47}$
Second zonal gravitational harmonic	J_2	$0.262^{+0.103}_{-0.112}$	$0.431^{+0.046}_{-0.051}$
Rotation axis obliquity (°)	i_{sp}	$76.83^{+1.03}_{-0.59}$	$75.32^{+0.68}_{-0.59}$
Rotation axis precession (°)	Ω_{sp}	$13.1^{+0.65}_{-0.75}$	$13.4^{+0.57}_{-0.52}$
Systematic error fraction	f_{sys}	$\cdots$	$0.122^{+0.115}_{-0.065}$
Systematic error uncertainty	$\log_{10}(\sigma_{sys}/1'')$	$\cdots$	$-2.085^{+0.169}_{-0.201}$
Derived parameters			
Inclination w.r.t. Haumea's equator, Namaka (°)	ε_N	$12.79^{+1.01}_{-0.58}$	$11.56^{+0.70}_{-0.65}$
Inclination w.r.t. Haumea's equator, Hi'iaka (°)	ε_H	$1.01^{+0.66}_{-0.47}$	$2.13^{+0.63}_{-0.68}$
Haumea pole right ascension (°)	α_p	$282.9^{+0.6}_{-0.7}$	$283.1^{+0.5}_{-0.5}$
Haumea pole declination (°)	δ_p	$-9.7^{+0.6}_{-1.0}$	$-8.1^{+0.6}_{-0.7}$
Orbit pole right ascension, Namaka (°)	α_N	$292.1^{+0.1}_{-0.1}$	$292.0^{+0.1}_{-0.1}$
Orbit pole declination, Namaka (°)	δ_N	$-0.6^{+0.1}_{-0.1}$	$-0.7^{+0.1}_{-0.1}$
Orbit pole right ascension, Hi'iaka (°)	α_H	$283.00^{+0.03}_{-0.03}$	$282.96^{+0.03}_{-0.03}$
Orbit pole declination, Hi'iaka (°)	δ_H	$-10.24^{+0.04}_{-0.04}$	$-10.23^{+0.04}_{-0.04}$

NOTE—Reported values represent the median value taken from the posterior distribution, while the stated uncertainties represent the 16th and 84th percentiles. All fitted angles are relative to the J2000 ecliptic plane on Haumea-centric JD 2454615.0 (2008 May 28 12:00 UT), chosen to match the epoch used in Ragozzine & Brown (2009). Assumed c-axis for Haumea is 537 km (Dunham et al. 2019) and spin period is 3.915 hours (Rabinowitz et al. 2006), however, altering these values produces no meaningful change to the fit. To transform to J_2 from only the more physically meaningful J_2R^2, we use a volumetric radius of 798 km (Ortiz et al. 2017).

vation of Namaka. This inconsistency was attributable to the data rather than the model, as shown by fits both with and without our robust likelihood model. Our robust likelihood model parameters indicated that approximately 10% of the data had uncertainties underestimated by $\sim$10 milliarcseconds. Fits without the robust likelihood model were extremely similar to those with it, except the fit quality was much worse. When closely examined, no obvious problems were seen in the Keck or HST images, and no difficulties arose during our analysis of the images. To examine whether our image analysis techniques were to blame, we attempted to extract astrometry from the images with a variety of techniques (e.g., Gaussian PSF fitting, WFC3 model PSF fitting, etc.), all of which yielded similar results.

In addition to the internal inconsistency, the HST-Keck combined fit also produced a measurement for Haumea's J_2 that was too high to be compatible with other observations of the Haumea system (see Section 5 for more discussion). In comparison, the HST only fit showed no such issues. When the orbit fits are compared, very little changes between the models with the exception of Hi'iaka's mass, Haumea's J_2, and Haumea's spin pole direction. As unknown systematic errors are affecting our orbit fit, we choose to proceed by eliminating possible sources of these systematic errors. Since HST's PSF is extremely stable and has been extensively cross-calibrated across instruments, we adopt the HST only orbit fits for the purpose of this work. This choice results in larger uncertainties within the model, but allows us to be more confident that our results are not affected by systematics. Although we adopt the HST only fit, we still discuss the implications of our combined orbit fit in Section 5, as well as reporting its results in Table 2.

The results presented here are our most refined orbital fits. Including our preliminary analysis, exploratory fits, and fits using different likelihood models, our nominal orbit model is the result of well over 10^9 individual likelihood evaluations. We show the HST only orbit model in it entirety as a corner plot (Foreman-Mackey et al. 2016) in Figure 1. Each column in the corner plot displays the marginal posterior distribution for each parameter as a histogram (at the top) and 2-dimensional joint posterior distribution as a contour plot. In addition, we display the marginal posteriors for both fits in Table 2. Both Figure 1 and Table 2 also contain several derived parameters, parameters that are functions of our fitted parameters. To display the fit quality, we show the residuals of the best fit parameter set in Figure 2, alongside 1, 2, and 3 σ error contours. While this best fit parameter set is
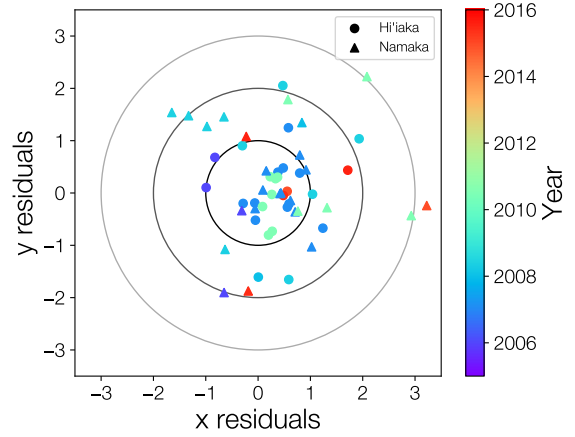
Figure 2. The normalized residuals of the best parameter set from our HST-only (non-robust) orbit fit. x and y correspond to ecliptic longitude and latitude, which is the primary coordinate system used in `MultiMoon`. Hi'iaka residuals are shown as circles and Namaka with triangles. The color of each point corresponds to the observation date. The circles correspond to 1, 2, and 3σ error contours. As reported in the text, this fit corresponded to a reduced $\chi^2 \sim 1.10$. We find that although the fit quality is worse than would be desired, the p-value of associated with the χ^2 statistic is 0.23, indicating an acceptable fit.

only one realization of our entire posterior distribution, it illustrates the overall quality of our fit.

One of the outstanding features of our orbit fit is our detection of Haumea's J_2. When assuming the shape model derived from stellar occultation measurements (Ortiz et al. 2017), we find $J_2 = 0.262$. However, our orbit fit shows that Haumea's J_2 and Hi'iaka's mass are highly degenerate with one another. In Figure 3, we show, in detail, the degeneracy between these parameters as a function of reduction in fit quality. It is clear that a large range of values for these two parameters are acceptable, with nearly no reduction in fit quality. In our HST+Keck orbit fit, we find that Haumea's J_2 has much lower uncertainties, but is unexpectedly high, $J_2 = 0.431$. Although probably attributable to unidentified systematic errors in our dataset, we will discuss possible causes/interpretations of this unusual measurement in Section 5. Our detection of Haumea's J_2 is significant in both orbit fits. The HST only fit detects J_2 at $\sim$2.5σ confidence, while the HST+Keck fit detects it at $> 5\sigma$ confidence. Alongside our detection and measurement of Haumea's J_2, we also provide a measurement of Haumea's rotation pole. We find that Haumea's pole (or more precisely, the pole of Haumea's gravitational quadrupole) points toward
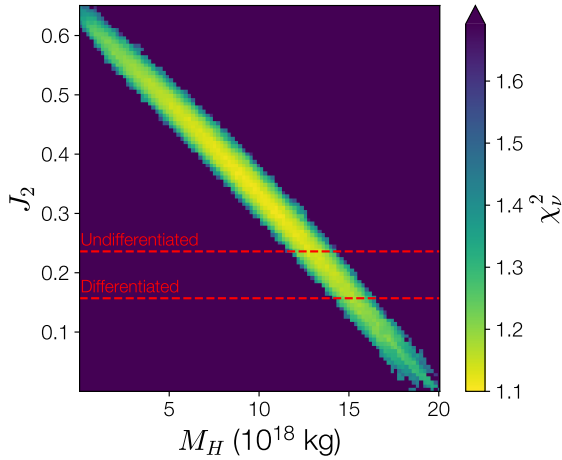
Figure 3. The joint Haumea J_2–Hi'iaka mass posterior distribution. Instead of displaying the density of sampled points as in Figure 1, we show the maximum fit quality (as measured by reduced χ^2) in a small bin. Bins without any sampled points, indicating extremely poor quality fits, were set to the minimum bin value, although the true value is likely much worse. We find that the best fit with $\chi_\nu^2 \sim 1.1$ has a p-value of 0.23, meaning there is a 23% chance that random chance would produce a worse fit. A $\chi_\nu^2 \sim 1.25$ corresponds to a p-value of 0.05. Dashed red lines show the expected J_2 values from different internal density models. The undifferentiated model assumes a homogeneous interior along with the occultation derived shape model (Ortiz et al. 2017). The differentiated model is a two layer model proposed by Dunham et al. (2019). The posterior shows that both models are consistent with the data, although the differentiated model is slightly disfavored.

$(\alpha_p, \delta_p) = (282.9^{+0.6}_{-0.7}, -9.7^{+0.6}_{-1.0})$, very close to the occultation derived rotation pole (Ortiz et al. 2017).

In our orbit fit, we are able to significantly detect the masses of both satellites at significance $> 3\sigma$. RB09 previously detected Namaka and Hi'iaka's masses, but only with 1.2σ confidence for Namaka. While our fit strongly detects both, the uncertainty on Hi'iaka's mass is substantial due to its degeneracy with Haumea's J_2. Alongside mass measurements, we are also able to constrain the satellites' inclinations with respect to Haumea's equator. We find inclinations of $12.8^{+0.8\circ}_{-0.6}$ and $1.0^{+0.6\circ}_{-0.5}$, for Namaka and Hi'iaka, respectively. We also measure the satellites' mutual inclination of $13.2^{+0.2\circ}_{-0.2}$.

Our orbit fits are significantly different from past orbit fits (Ragozzine & Brown 2009; Gourgeot et al. 2016). While this difference is expected since we include more dynamical effects (e.g. including J_2), some important differences are still present. Most notable is the change in orbit angles, which stems from RB09's incorrectly tabulated astrometry, allowing for close agreement with

the orbit planes found in Gourgeot et al. (2016). We find a lower eccentricity for Namaka ($0.2179^{+0.0032}_{-0.0033}$) compared to RB09 ($0.249 \pm 0.015$ using the same epoch), also presumably due to their incorrect astrometry. Another notable difference is the change in Hi'iaka's mass ($12.13^{+3.22}_{-3.11} \times 10^{18}$ kg) when compared to RB09 ($17.9 \pm 1.1 \times 10^{18}$ kg), due to our inclusion of Haumea's J_2. Our preliminary fits showed that our orbit model, when evaluated with a small J_2 approximately reproduces RB09's measurement of Hi'iaka's mass.

When compared to the orbit model presented in Gourgeot et al. (2016), we find quite large differences in orbital parameters especially in the fit for Namaka's orbit. This is unsurprising since their orbit model was a pure Keplerian orbit fit, neglecting both Haumea's J_2 and Hi'iaka's gravitational force. Their analysis claimed that there was no signature of non-Keplerian effects caused by Haumea's J_2 in the system, although they use a much shorter span of data than our analysis. We find that non-Keplerian effects from both satellite-satellite interactions and Haumea's J_2 are strongly detected, however it remains uncertain how strong each effect is.

5. DISCUSSION

5.1. *Haumea's Large J_2*

Assuming a homogeneous density structure and using the equations found in Yoder (1995), the occultation derived shape implies a J_2 of 0.24 (Ortiz et al. 2017). Allowing for differentiation decreases J_2 significantly. The model for a two-layer differentiated Haumea presented in Dunham et al. (2019), gives an overall J_2 of $\sim$0.16. Our model fitting to all available data (HST+Keck) is 3σ inconsistent with both of these models. However, the fit with only HST data is consistent with both, encouraging us to explore possible reasons Haumea's J_2 may be higher.

One possible reason could be the gravitational contributions from Haumea's ring. Assuming a circular ring, the following expression can be derived for the J_2 contribution of a ring:

$$J_2 R^2 = \frac{1}{2} \frac{M_r}{M_P} r^2 \qquad (3)$$

where M_r and M_P are the masses of the ring and Haumea, respectively, and r is the radius of the ring. For the ring to contribute $\sim$1% of the measured $J_2 R^2$ of our HST only fit, the ring would have to be of order 10^{18} kg, about the mass of Namaka, given the known ring radius of 2287 km. For it to be the cause of Haumea's unexpectedly high J_2, the ring would need to be two orders of magnitude more massive, equivalent to tens of

Hi'iaka masses. While no mass constraints on the ring are found in the literature, this value is absurdly high. Hence, the ring is unlikely to contribute significantly to our measured J_2. There is a distinct possibility that more rings may be detected in future occultations (e.g. Pereira et al. 2023), but even when combined, a ring system is unlikely to contain enough mass to substantially contribute to Haumea's J_2.

Another potential source is an undetected satellite within Namaka's orbit. Averaged over an orbit, the putative inner satellite would act similar to a solid ring of material. Hence, using Equation 3 above to calculate the J_2 of a putative inner satelite orbiting at 10000 km, we find that an inner satellite with a mass near Namaka's mass could significantly contribute to Haumea's measured J_2. Unfortunately, Burkhart et al. (2016) significantly ruled out satellites more than 60 km in diameter closer than 10000 km by using a nonlinear shift-and-stack image analysis technique. This diameter implies a mass approximately one-tenth of Namaka's mass, which would scarcely contribute to the overall J_2. Given this, we believe it is unlikely that our results could be caused by an unknown inner satellite. Likewise, undiscovered satellites external to Hi'iaka's orbit would not produce the observed signature.

An alternative reason could be an extreme mass anomaly on Haumea's surface, either positive or negative, which would cause Haumea's J_2 to be larger than expected. Unfortunately, the mass surplus (or deficit) would have to be substantial, of order $\sim 10\%$ of Haumea's total mass. Maintaining a mass anomaly of that magnitude would require Haumea to have implausibly high material strength. Using the method developed by Johnson & McGetchin (1973), we optimistically estimate that Haumea may support a maximum topographic feature of ~ 10 km, amounting to far less than the ~ 100 km required to produce an unusually high J_2. Likewise, Haumea could have an unusual interior density distribution. If Haumea formed in the aftermath of a large collision, it may have an unusually shaped core left over as a remnant of this impact. Alternatively, its core could be offset relative to its external figure, potentially explaining Haumea's "Dark Red Spot" (Lacerda 2009). Assuming Haumea's core is triaxial and adopting the external figure of Haumea as measured by stellar occultation, we can calculate the J_2 of Haumea with an arbitrary triaxial core shape with an offset. We find that for any realistic core shape or offset, Haumea's J_2 can not increase by more than 50%, still well below the constraint provided by the HST+Keck fit. In any case, the extreme version of these hypotheses are unlikely to be geophysically viable as they ignore fluid-like relax-ation of Haumea's core and mantle. We believe that an unusual interior is unlikely the cause of our results.

Due to the implausibility of all of these solutions, we conclude that our result is due to factors dependent on our modeling techniques or data. One possible explanation is higher order non-Keplerian dynamics taking place within the system. Since our model only includes Haumea's J_2, other gravitational harmonics may be needed to fully model the system. To investigate the effect of C_{22}, we ran a `MultiMoon` fit that included Haumea's C_{22} potential. This fit gave nearly identical results and found no constraint on C_{22}, indicating that the orbital dynamics of the system are not strongly coupled to C_{22}. Indeed, previous work exploring the effects of C_{22} found that it is only relevant when $P_{orb} \sim P_{spin}$, or near a low order SOR (Proudfoot & Ragozzine 2021). Beyond quadrupole dynamics, fourth-order, or hexadecapole, dynamics could contribute to orbital precession, but as previously discussed their r^{-5} dependency ensures that their contributions are small. Odd harmonics (e.g., J_3, C_{31}, etc.) could, in theory, also play a role in the system's orbital dynamics. (Note that the "dipole" term is 0 due to using the center-of-mass as the coordinate system; a center-of-mass–center-of-figure offset can contribute to J_2 which was included in the calculations with the offset core above). Taking the J_3 harmonic as an example, we find that the ratio of nodal precession caused by the J_3 and J_2 harmonics is $\dot{\Omega}_{J_3}/\dot{\Omega}_{J_2} \approx 0.006 \frac{J_3}{J_2}$ when $\dot{\Omega}_{J_3}$ is at its maximum. Typically the J_3 harmonic is much smaller than J_2, implying the nodal precession induced by J_3 is a very small effect. The same is true of the apsidal precession. While it seems unlikely that J_3 or other odd harmonics cause significant changes in the dynamics on the timescale of our observational data, future investigations should explicitly test whether odd numbered harmonics are necessary for accurate modeling of the Haumea system.

Another possible effect that we do not account for is the satellites' putatively nonspherical gravitational fields. Our model assumes that Hi'iaka and Namaka are point masses, although they are likely to be substantially nonspherical. In some cases, however, the gravitational harmonics of a system's secondary can play a major role in the overall orbital dynamics (e.g. Ragozzine & Wolf 2009). `MultiMoon` is well poised to explicitly test this assumption. Rather than adding six parameters to our overall model, which would be computationally expensive, we can simply add the satellites' harmonics as fixed values. We can then compare a model without their harmonics to one with them, allowing us to see the change in system dynamics. In this comparison, we use the characteristics of all our observations (HST+Keck) to explic-
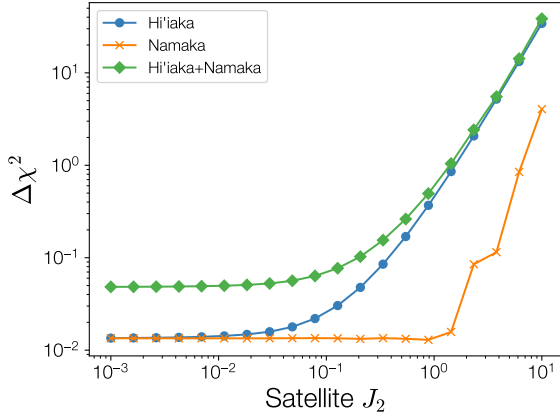
Figure 4. Change in orbit fit quality due to the nonspherical shapes of Haumea's satellites. In this plot, $\Delta\chi^2 = \sum^i (x_{i,J_2} - x_{i,J_2=0})/\sigma_{i,obs}$, where x_{i,J_2} and $x_{i,J_2=0}$ are synthetic astrometric measurements from models including satellite J_2 and those without. $\sigma_{i,obs}$ are the true measurement uncertainties for the system as tabulated in Table 1. This formulation allows us to directly determine whether the satellites' J_2 values produce detectable changes in the system relative astrometry, given our current observations (HST+Keck). The parameters for the models used were taken from the best fit of our orbit fits. The rotational poles of the satellites were chosen to have high obliquities (w.r.t. their Haumea-centric orbits) to enhance the effect of J_2. The three separate lines show each satellite's individual contribution, as well as a comparison where both satellites have (the same) J_2. For reasonable values, $J_2 \lesssim 0.5$, very little change in fit quality is found, although for extremely nonspherical shapes, Hi'iaka's J_2 could begin to alter the fit.

itly connect the dynamical change to actual observability. In Figure 4, we show the change in orbit fit quality as a function of Hi'iaka and Namaka's J_2, when both satellites have a moderately high obliquity. We define change in fit quality as $\Delta\chi^2 = \sum^i (x_{i,J_2} - x_{i,J_2=0})/\sigma_{i,obs}$, where x_{i,J_2} and $x_{i,J_2=0}$ are synthetic astrometric measurements from models including satellite J_2 and those without and $\sigma_{i,obs}$ are the measurement uncertainties for the system as tabulated in Table 1. Using those measurement uncertainties allows us to connect the system's dynamics to the actual observations. Overall, we find the fit quality is barely decreased when reasonable values for J_2 are tested. Hi'iaka would need $J_2 > 2$ for a detectable change, while Namaka would need $J_2 > 10$. For comparison, Arrokoth, a contact binary, has a $J_2 \sim 0.3$. While not an exhaustive search of parameter space, this is strong evidence that Hi'iaka and Namaka's nonspherical shapes do not significantly contribute to the system's dynamics with the present data.

In our view, the only remaining option is the presence of unknown systematic errors plaguing our dataset. Despite our use of novel statistical techniques, our model cannot account for all systematic errors arising from combining our dataset. For example, time-varying distortions in the NIRC2 field cannot be appropriately accounted for by our model. Likewise, wavelength-dependent offsets between Haumea's center of light and center of mass, potentially caused by the known wavelength-dependent rotational variability known as the "Dark Red Spot" (Lacerda 2009) may introduce unwanted systematics when combining the data sets. Indeed, when combining the datasets, we find that the Keck data from the 2020s is incompatible with the HST visit from 2014. Our combined dataset produces large residuals for the 2014 HST visit, while the HST only fit shows no such effect. While disconcerting, this conclusion is not extremely surprising given a similar result in RB09, from which we draw much of our data. Those authors similarly found that the Keck data was inconsistent with the HST-only fits. We thus argue that unknown systematic errors are the source of our unusually high measurement of J_2. HST instruments are extremely well-studied and have been rigorously cross-validated, so we view the HST only fit as more trustworthy. To remain as conservative as possible, we adopt the HST only fit as our nominal model for the rest of the analysis in this work.

5.2. *Haumea's Pole*

Among TNOs, very few spin poles have been constrained. When disregarding non-Keplerian fitting, the only techniques currently able to characterize the spin poles of TNOs are long-term light curve monitoring and occultations. Light curve inversion techniques require observations of a TNO over a significant portion of their orbit, which is implausible due to TNOs' long heliocentric orbital periods. Occultations are extremely powerful for inferring spin poles, but observations of multiple multi-chord events are required, which are only available for a few TNOs. Non-Keplerian orbit fitting now adds an additional tool which can be used to understand the spin poles of TNOs[2]. Normally, non-Keplerian fitting cannot find a unique pole solution, but is able to determine the angle between the primary's spin pole and the secondary's orbit normal. However, since Haumea has two satellites, the spin pole can be found unambiguously.

---

[2] Technically, non-Keplerian fitting finds the pole direction of the nonspherical gravitational field, not the figure of the overall body. However, in practice these are functionally identical, especially for large objects like Haumea (Ragozzine et al., submitted).

Our measurement in this work represents the first dynamically determined spin pole among TNOs. We are able to place tight constraints on the spin pole direction of Haumea, finding $(\alpha_p, \delta_p) = (282.9^{+0.6\circ}_{-0.7}, -9.7^{+0.6\circ}_{-1.0})$. Our dynamically determined spin pole measurement lies $2.3°$ from the ring pole determined by stellar occultation $(\alpha_p, \delta_p) = (285.1 \pm 0.5°, -10.6 \pm 1.2°)$ (Ortiz et al. 2017). Given that our methods are completely different from those used in analyzing the stellar occultation and we use no constraints from that work, the close match is encouraging. Formally, however, these two spin pole measurements are $\sim 2\sigma$ apart. The difference could be a real effect (i.e., Haumea's ring is inclined with respect to Haumea's nonspherical gravitational field), but the nodal precession of ring particles induced in this case is likely to erode the rings excessively (Marzari 2020). It seems much more likely that the ring is coplanar with Haumea's gravitational field, and the disagreement is due to model dependent factors or random chance. For example, Ortiz et al. (2017) modeled Haumea's ring as a flat, circular annulus, but the true ring may have substantial eccentricity and/or thickness. Alternatively, since the spin pole in our fit is highly correlated with J_2, our large uncertainties may cause/contribute to the disagreement. When examining our HST+Keck fit, we find the spin pole measurements are even further apart, lending further credibility to the HST only model.

5.3. *The Origin and Evolution of Haumea's Satellites*

Our new information on the properties of the Haumea system give more accurate insight into the formation and evolution of Haumea and its satellites.

Presumably, Haumea's satellites (and possibly its ring) formed in the same event that created the Haumea family. The many proposed paths for the formation of the family were reviewed in Proudfoot & Ragozzine (2019). Geophysically, a catastrophic collision is not a plausible scenario for explaining family members that are a low fraction of Haumea's mass ejected at far below escape velocity with a shallow size-distribution slope that are made of chunks of somewhat pure water ice in a low-probability environment for collisions. Instead, these observations suggest that a differentiated proto-Haumea spun too fast for self-gravity to maintain coherent and an icy slurry was released from the tips of Haumea in chunks of various sizes ejected at relatively low speeds as in the modeling of Leinhardt et al. (2010) which is able to reproduce (with some uncertainties) most of the observed properties of the family. Originally, Proudfoot & Ragozzine (2019) rejected this model (and all other models) because this scenario would nominally produce family members with correlations in proper or-

bital elements that are not seen. However, Proudfoot & Ragozzine (2022) found that placing the formation of the Haumea family in context with the formation of the outer solar system allows for a reasonably timed family-forming event to occur before Neptune has completed its outward migration, including an eccentricity "jump" that stirs the family enough to remove the expected proper element correlations. This conclusion was robust to a range of Neptune migration models already proposed in the literature (e.g. Nesvorný 2015) without tuning. While Proudfoot & Ragozzine (2022) focused on finding a model that was probable and consistent with observations, positive definite evidence of this scenario will likely need to wait for the significant increase in Haumea family member discovery expected from the Vera C. Rubin Observatory's Legacy Survey of Space and Time (e.g. Pike et al. 2020). There is still some debate in the literature on the original reason that proto-Haumea had too much angular momentum: Proudfoot & Ragozzine (2022) propose the merger of a near-equal-mass binary similar to Pluto-Charon perhaps triggered by Kozai cycles initiated due to Haumea's placement on a higher inclination orbit. Noviello et al. (2022) point out that internal evolution could change the moment of inertia, leading to excess angular momentum for a Haumea that was initially rapidly rotating. Ortiz et al. (2012) and others suggest that it may be the cumulative effect of many smaller impacts, though starting with a rapid rotation would significant increase the probability that a random walk would lead to such a rapid rotation, keeping in mind that Haumea has the fastest spin period of all known large ($r \gtrsim 100$ km) solar system small bodies.

Whatever the origin, the general agreement is that Haumea goes through a phase of excess angular momentum where water ice chunks are ejected at low velocities from the tips of Haumea. We are not aware of any detailed analyses of how this configuration leads to the observed family and satellites beyond the output of Leinhardt et al. (2010). In any case, it is interesting to note that Hi'iaka is approximately the same size as the largest family members like 2002 TX$_{300}$ (Elliot et al. 2010) and similarly has a deep water ice spectrum (Barkume et al. 2006). Furthermore, objects with a mass of 10^{19} kg have an escape velocity of 300 m/s, comparable to the orbital velocity around Haumea near the Roche limit. This implies that objects of this size have a "Safronov number" near 1, meaning that encounters between these objects can lead to ejection from the Haumea system... but only with a small escape velocity consistent with that seen from Haumea family members. Thus, a plausible starting point for the formation of the satellites is a disk of

satellitesimals ejected from the fast-spinning Haumea, mostly composed of pure water ice with sizes similar to known satellites and family members. Leinhardt et al. (2010) report the formation of family members in their simulations, but it is not clear from these simulations or from other plausible scenarios whether Haumea family members are chunks ejected immediately from the tips of Haumea at beyond escape velocity without interaction with other chunks or whether the entire family is formed from ejection due to "chunk-chunk" interactions. Given that the distribution of velocities should be smooth with only the highest velocities actually escaping the Haumea system, it is fair to say that there are many chunks that remain in orbit and we refer to these as satellitesimals.

We note that this is a similar initial configuration as considered in Ćuk et al. (2013) from the destruction of an "ur-satellite," proposed there to be the origin of the family and satellites. The investigation of Proudfoot & Ragozzine (2019) suggests that the distribution of known family members is not well-matched by the destruction of a satellite collision, though they did not consider interactions between objects nor did they consider the possibility of changes in the distribution from Neptune migration as in Proudfoot & Ragozzine (2022). The rationale for satellite destruction as a family-formation hypothesis is to both increase the probability (since a much smaller impactor is needed) and to explain the low velocity dispersion of the family. This latter reasoning is based on the observation that the Haumea family's 100 m s^{-1} velocity dispersion is approximately the same as the escape velocity from an object with the total mass of the Haumea family. However, this order-of-magnitude argument does not seem plausible under more detailed investigation (Proudfoot & Ragozzine 2019). Furthermore, recent results from Pike et al. (2020) indicate that the size distribution of family members is very shallow, and there are far fewer small family members detected than would be expected in a catastrophic collision, even when accounting for observational biases. For this reason and other reasons discussed in Proudfoot & Ragozzine (2019) and Proudfoot & Ragozzine (2022), we do not consider the satellite-destruction theory further.

Without further modeling, the properties of the satellites themselves could be consistent with the ur-satellite destruction hypothesis as discussed in (Ćuk et al. 2013). They suggested that strong evidence for this hypothesis would result if it were possible to show that the satellites orbit retrograde relative to Haumea's spin. We agree with their assessment that such a configuration is consistent with observational data, even with the updates provided here. At that time, they suggested that addi-

tional observations could potentially detect this directly, but our work here shows that this would be extremely challenging to do with satellite astrometric observations. Additional investigation shows that detecting retrograde Haumea spin through C_{22} is implausible (Proudfoot & Ragozzine 2021). Not mentioned explicitly in Ćuk et al. (2013) is that retrograde spin could also be detected by observing the angular momentum exchange among the spin and the orbits of Namaka and Haumea. However, our fits show that Haumea has over 99.99% of the angular momentum and that its spin axis is hardly affected by the dynamical interactions with the satellites (see Section 5.5. We propose that the most plausible way to test this hypothesis is to look for astrometric offsets from Haumea's Dark Red Spot (Lacerda 2009) which could potentially be detectable using JWST or even HST archival data depending on the exact properties of the spot.

The initial disk of satellitesimals should rapidly evolve through ejections and collisions. The impacts are relatively low velocity and at cold temperatures, suggesting that they remain mostly in solid phase, though more detailed modeling would be required to determine what happens to the phase of the disk materials as a function of composition. We agree with (Ćuk et al. 2013) who propose that unejected material likely experiences a collisional cascade that leads to a final configuration of a ring of near-circular, near-coplanar disk of small particles. The observed ring could have derived from the parts of this initial ring that did not form into satellites.

More modeling will be necessary to determine whether the extent and properties of this initial ring are likely outcomes from a graze-and-merge impact (or satellite destruction). Combining SPH modeling with long-term dynamical evolution should provide valuable insight into plausible starting conditions. We encourage work on this problem.

After their initial formation, there are several physical processes which can influence the evolution of the satellites until they reach their current configuration. The most important effects are expected to be Hi'iaka-Namaka interactions, tidal evolution, excitation from passing TNOs and binaries, and possible interactions from previous satellites (Ćuk et al. 2013; Hastings et al. 2016). These are discussed in detail in Ćuk et al. (2013) and we focus here only things that are updated in our new fit.

Ćuk et al. (2013) found that long-term orbital stability would be significantly improved if the satellites were ∼50% of their nominal masses reported in Ragozzine & Brown (2009). Indeed, our new results are most consistent with satellites that are ∼60% of the initially es-

timated masses with the Namaka/Haumea mass ratio of $3.0 \pm 0.6 \times 10^{-4}$ and the Hi'iaka/Haumea mass ratio of $3.1 \pm 0.8 \times 10^{-3}$ in the HST-only fit (see Table 2), though this is strongly affected by the degeneracy discussed above.

Ćuk et al. (2013) also investigate in detail the effect of the 8:3 and 3:1 mean-motion resonances between the satellites, especially in the presence of tidal evolution. This was based on the observation by Ragozzine & Brown (2009) that the satellites were possibly in or near the 8:3 resonance, suggesting that tidal evolution in resonances could explain the source of the moderately eccentric and inclined orbits. This idea was further strengthened by the observation – still true with the new orbit fit – that the excitation is similar in eccentricity and inclination and is inversely proportional to the masses of the satellites. This means that the "Angular Momentum Deficit" (Laskar 1997) is approximately evenly partitioned between the two satellites, suggesting they have been strongly dynamically coupled at some point in the past (or present). We find a period ratio of Hi'iaka and Namaka of 2.689 ± 0.004 (including corrections to Newton's Version of Kepler's Third Law from J_2), slightly closer to the 8:3 mean-motion resonance that reported in Ragozzine & Brown (2009). With the residual uncertainty in Hi'iaka's mass and Haumea's J_2, we leave to future investigation whether the 8:3 resonance is currently dynamically active in the system. The general conclusion of (Ćuk et al. 2013) that resonance passage could explain the excited orbits remains consistent with the updated fits.

The primary challenge in explaining the current orbital configuration of the satellites is their distant orbits from Haumea at $\sim$36 and $\sim$70 primary radii. Tidal evolution to such distances is challenging in standard tidal theories, requiring Haumea tides to be extremely dissipative with an implausible combination of tidal parameters. This is exacerbated by a factor of $\sim$2 with the lower masses for the satellites, but Quillen et al. (2016) find that the triaxial shape of Haumea increases tidal evolution by a factor of a few (though not the factor of several hoped for by Ragozzine & Brown (2009) and Ćuk et al. (2013)). It is possible that this can be resolved by detailed investigations beyond simplified tidal and geophysical models, e.g., continuing work by Quillen et al. (2016) and Noviello et al. (2022) with more accurate modeling as summarized by Bagheri et al. (2022) and citations therein. It is interesting to note that, ignoring satellite-satellite interactions, the expected positions of two moons with a mass ratio of $\sim$10 is a semi-major axis ratio of $\sim$2 which is consistent with the relative locations of Namaka and Hi'iaka.

One potential resolution to the extreme tidal dissipation is to start Hi'iaka and Namaka near their current locations. (Since tidal expansion is very strongly dependent on separation, even starting at $\sim$90% of the present distance does not relieve pressure on tidal theories.) This is the reason that Ćuk et al. (2013) posited that the ur-satellite was destroyed at near the positions of the current satellites. Further modeling of the satellitesimal disk distribution created in a graze-and-merge impact is called for, but given that we observe objects ejected from this disk, it could have been extended out to the Hill sphere and readily allow for a disk at 1% of the Hill radius where Hi'iaka is located. Whether Namaka and Hi'iaka could have formed directly from this disk requires further investigation. Along these lines, we note that although the satellites seem well-separated, dynamically speaking they are only separated about 5 mutual Hill radii, suggesting they are dynamically packed. Indeed, Ćuk et al. (2013) found that masses larger than those from our fit are likely unstable. Intermediate satellites could not fit dynamically, so perhaps Namaka and Hi'iaka are the natural outcome of an extended disk near their present locations.

can form directly from a disk eventually formed from the same event that spun up Haumea and created the family.

In conclusion, the formation and evolution of Namaka and Hi'iaka are plausibly connected to the same process that spun up Haumea and created the family. One formation hypothesis is that water ice chunks which do not escape to form the family eventually collide and grind down to a disk near the present location of the satellites. Namaka and Hi'iaka perhaps form directly from this disk and recent dynamical interactions, e.g., from the nearby 8:3 resonance, lead to the orbits seen today, as proposed in Ćuk et al. (2013). Once Hi'iaka's mass is better known, a more detailed investigation into the secular, resonant, and tidal dynamics could confirm or refute this hypothesis. However, the most important next step is more detailed modeling of the post-spin-up and family ejection process, extending into the longer timescale of setting the initial conditions for the formation of the satellites.

5.4. *Ring-Satellite Interactions*

Haumea's ring, first discovered during a stellar occultation, is observed to lie close to Haumea's equatorial plane (Ortiz et al. 2017). This matches theoretical expectations, which show that ring particles should collisionally damp to the equatorial plane in the presence of Haumea's J_2. When accounting for interactions between ring particles and Haumea's satellites, however,

ring particles can preferentially settle in the satellite orbit plane (Marzari 2020). However, the satellites are too far away and/or not massive enough to cause this to occur for the ring. The satellites' main dynamical roles are to act as small perturbers that increase velocity dispersion. Marzari (2020) studied the increase in collision velocity of ring particles under the influence of Haumea's satellites and found that collision velocities still remained low with typical velocities < 1 m s^{-1}.

It may be possible that if other rings exist external to the currently known ring, satellite-ring dynamics may be more important. As the strength of satellite-ring interactions increases, the collision velocities between ring particles may become large enough to completely disperse the ring. Rings external to the Roche limit may be possible at the temperatures of the Kuiper belt (Morgado et al. 2023; Pereira et al. 2023), but in Haumea's case they are likely to be in a regime where perturbations make them long-term unstable.

5.5. *Rotational Dynamics*

The rotational dynamics of the Haumea system are extremely interesting to study. For Haumea itself, the torque from both satellites on Haumea's nonspherical body cause a small amount of axial precession. We show a 1000 year integration of Haumea's spin dynamics in Figure 5. The integration is performed by SPINNY, the spin-orbit integrator at the heart of MultiMoon (Ragozzine et al., submitted). We find that Haumea's axis precesses by $< 1°$ on a timescale of 100s of years. Visible is a complex precession cycle in Haumea's spin pole direction, with one 'fast' frequency and one 'slow' frequency. These two frequencies are caused by the torque from each satellite, with periods corresponding to each satellite's nodal precession period. Namaka's nodal precession period is strongly coupled with both Hi'iaka-Namaka interactions and Namaka-J_2 interactions. Since Namaka is coupled to Hi'iaka's nodal precession, Namaka's nodal precession then weakly couples to Hi'iaka-J_2 nodal precession, although this is a much smaller effect. Hi'iaka's nodal precession has a fast, low-amplitude component caused by Hi'iaka-Namaka interactions, as well as a slow, high-amplitude component from the Hi'iaka-J_2 interaction. The low amplitude, high frequency precession of Haumea's pole caused by Namaka would produce little detectable change in Haumea's light curve or occultation shadow. The Hi'iaka coupled precession has a much higher amplitude, but has a period of 100s of years, severely hampering detectability. Given Haumea's prolate shape, the satellites' torques can, in principle, also alter Haumea's rotation period, however this effect is

tiny due to Haumea's large angular momentum. Using SPINNY simulations, we estimate the period variations are $\sim 10^{-8}$ hours, approximately two orders of magnitude smaller than the uncertainty in the measured rotation period (Rabinowitz et al. 2006).

More amenable to detectability is possible precession of Hi'iaka's rotational axis. In Hastings et al. (2016), the light curve of Hi'iaka was studied using resolved photometry from HST images. They found that Hi'iaka is rapidly rotating ($\sim$9.8 hour double-peaked period) with an unusual sawtooth shaped light curve of amplitude $\Delta m \approx 0.23$. Using a simplified model of axial precession, they found that Hi'iaka's axial precession would be detectable on decade timescales if there was significant obliquity (w.r.t. its orbit). The detectability is significantly enhanced by Hi'iaka's high amplitude light curve. Detection of any precession would require long-term monitoring of Hi'iaka's light curve, which would slowly change amplitude and/or shape across the precession cycle. SPINNY provides an ideal framework for validating this possible method. Using the best fit from our nominal orbit model, we have explicitly modeled Hi'iaka's axial precession. In Figure 6, we show the evolution of Hi'iaka's rotation axis, assuming differing starting obliquities. Then in Figure 7, we illustrate how that precession translates to variation in Hi'iaka's light curve amplitude, assuming triaxial shapes as in Hastings et al. (2016). Interestingly, even in the case where Hi'iaka's pole is initially aligned with its orbit, precession still occurs. While initially surprising, the precession is due to Hi'iaka's nodal precession in its orbit around Haumea, which will always misalign Hi'iaka's spin pole. Encouragingly, even for a relatively small obliquity of $10°$, the precession is substantially different from the no precession case. This allows us to confirm previous results (e.g. Hastings et al. 2016) and show that small perturbations (e.g., Hi'iaka's eccentric orbit, torques from Namaka, etc.) seem to make little difference to the overall evolution. In the future, SPINNY and/or MultiMoon could be modified to explicitly model changes in light curve amplitudes. This method would provide a detailed model with which to understand the spin dynamics of Hi'iaka; we defer this to future work.

Even though Namaka has been solidly detected in several epochs of HST observations, no periodic brightness variations have been found, although photometry from HST programs is suggestive of a long rotation period (>1 day). Purely based on theoretical dynamical arguments, Namaka is expected to be significantly despun, except if its initial rotation period was extremely short (Hastings et al. 2016). Given Namaka's eccentric orbit, overlap between SORs is inevitably causes spin-
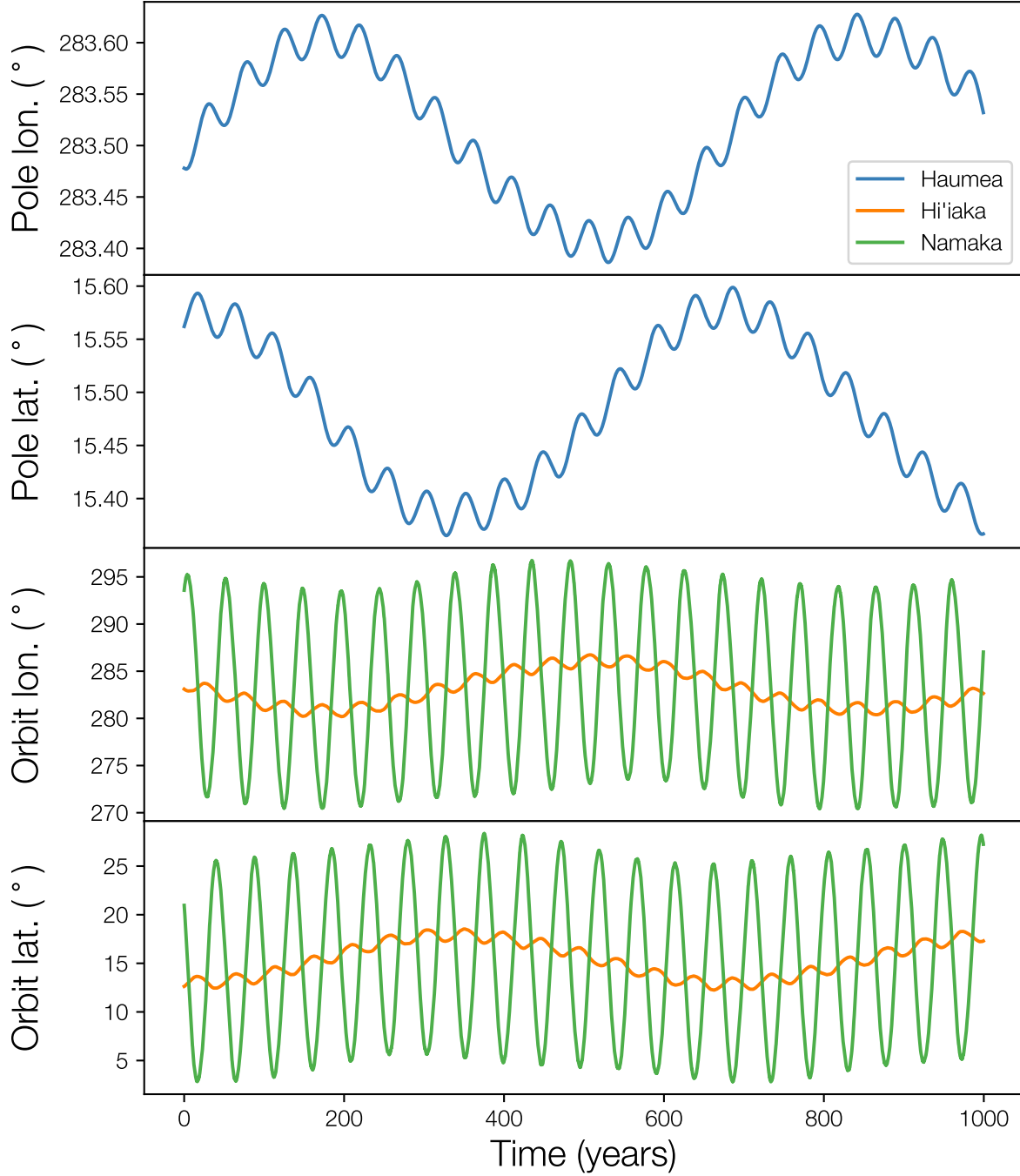
Figure 5. The spin precession of Haumea over a 1000 year integration. In the top two panels, we show the spin precession of Haumea in terms of pole ecliptic longitude and latitude. In the bottom two panels we show the precession of the orbit normal of Hi'iaka and Namaka, again in terms of ecliptic longitude and latitude. The integration parameters have been chosen to be representative of the posterior found in Table 2. Similar integrations with different values for Haumea's J_2 change the long-term precession period, but are qualitatively similar. Haumea's spin precession is coupled with the nodal precession of the satellites. High frequency, low amplitude variations in Haumea's pole direction are caused by Namaka's rapid precession, while low frequency, high amplitude variations are coupled with Hi'iaka's J_2 precession. As can be seen, the precession of all components are strongly coupled, both through Hi'iaka-Namaka gravitational interactions and interactions with Haumea's J_2.
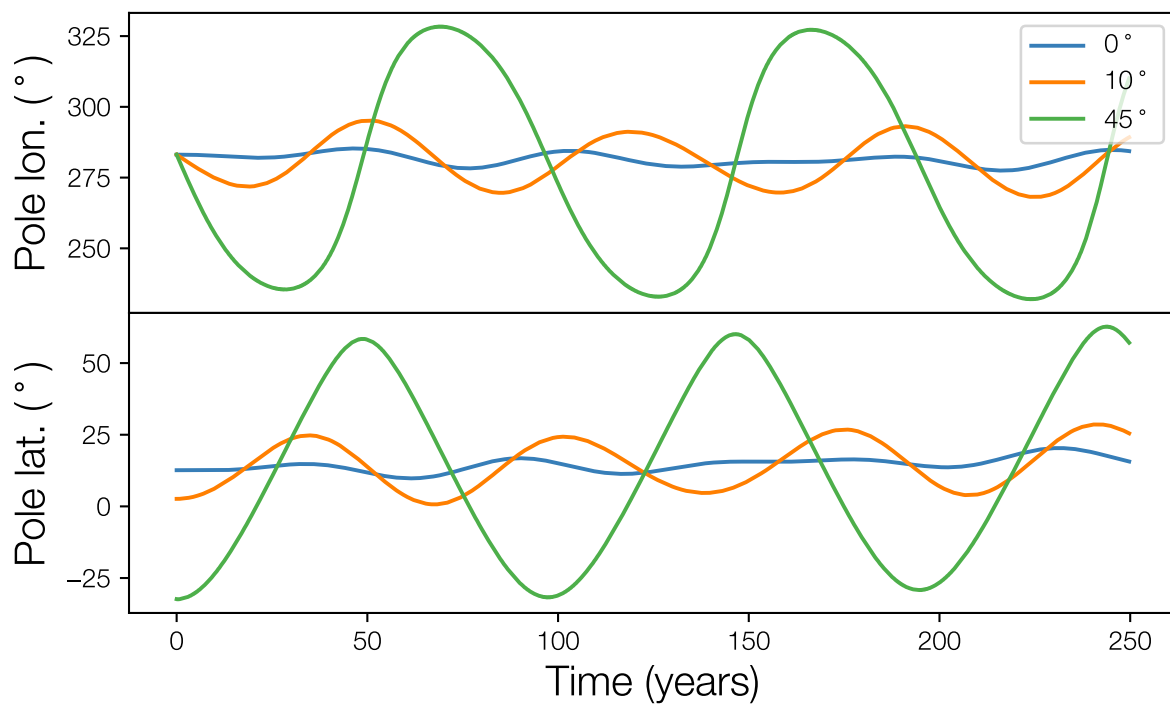
Figure 6. The precession of Hi'iaka's spin axis based on its initial obliquity. Similar to Figure 5, we show the precession of Hi'iaka's spin axis in terms of ecliptic longitude and latitude. Initial integration parameters have been chosen to be representative of the posterior found in Table 2. The moments of inertia of Hi'iaka were chosen to be similar to objects of similar size, although their values only change the frequency of the precession. For different initial obliquities, we find different precession periods, matching analytical theory and results in the literature (e.g. Hastings et al. 2016). Interestingly, there are small variations when Hi'iaka's spin is initially aligned with its orbit. Although initially there would be no net torque and no precession when aligned, since Hi'iaka's orbit precesses, the alignement is broken and precession begins.
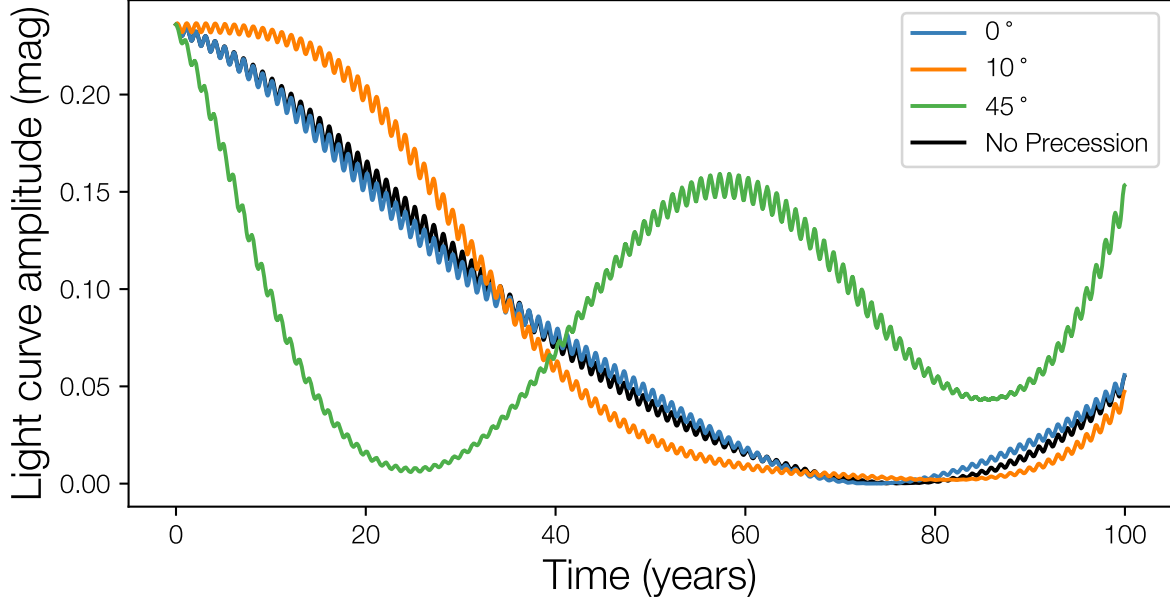
Figure 7. The change in Hi'iaka's light curve amplitude over time. Using the integrations similar to those shown in Figure 6, we calculate the light curve amplitude using Equation 1 from Hastings et al. (2016). Note that the x-axis is different than Figure 6. Axis ratios were chosen to be similar to other solar system objects at similar size, as well as approximately matching the light curve amplitude found in the literature (Hastings et al. 2016). The no precession case is found by taking a fixed pole direction. The fast variations in these functions are due to Earth's heliocentric orbit. Even for small obliquities, the light curve evolves significantly differently than the no precession case. As in Figure 6, we find that the aligned case (0°) still shows precession and slightly different light curve evolution when compared to the no precession case. Long-term monitoring of Hi'iaka's light curve may permit direct measurement of its spin pole over decadal timescales.

orbit chaos, very similar to Saturn's satellite Hyperion (Wisdom et al. 1984). As an illustration of chaotic rotation, the resonance overlap criterion, which predicts chaotic spin-orbit evolution if satisfied, near the 1:1 and 3:2 SORs is:

$$\sqrt{\frac{3(\mathcal{B} - \mathcal{A})}{\mathcal{C}}} \geq \frac{1}{2 + \sqrt{14e}} \qquad (4)$$

where $\mathcal{A}$, $\mathcal{B}$, and $\mathcal{C}$ are Namaka's principal moments of inertia and e is Namaka's orbital eccentricity. In this case, to avoid spin-orbit chaos Namaka's shape would have to satisfy $\frac{(\mathcal{B}-\mathcal{A})}{\mathcal{C}} < 0.025$. Satellites that are similar in size to Namaka generally have $\frac{(\mathcal{B}-\mathcal{A})}{\mathcal{C}} \gtrsim 0.1$. For example, with a mass between Namaka and Hi'iaka ($\sim 5 \times 10^{18}$ kg), Hyperion has $\frac{(\mathcal{B}-\mathcal{A})}{\mathcal{C}} \approx 0.26$.

While the above calculation is a simplistic example comparing just two resonances, in general, resonance overlap and spin-orbit chaos are expected for a slowly rotating Namaka. In Figure 8, we show the initiation of chaotic tumbling, where Namaka's attitude (i.e. pole direction) and rotation period evolve chaotically. Given

the difficulty of acquiring resolved photometric observations of Namaka and the long timespan needed to detect a slow (and possibly chaotic) rotation, confirming it may be extremely difficult. Similarly, searching for Namaka's light curve in unresolved photometry of the entire system is extremely difficult as Namaka's brightness only contributes ~1% of the total system flux.

5.6. *Future and past observations*

To enable future observations of the Haumea system, we have created an ephemeris of the system, containing the predicted $\Delta\alpha \cos\delta$ and $\Delta\delta$ of each satellite and the uncertainties on the positions. We compute the ephemeris using 500 random draws from our posterior distribution. The ephemeris contains the predicted positions every 8 hours between 2005 and 2035. In Table 3, we show the first 10 lines of the ephemeris. The ephemeris is published in its entirety in machine-readable format. Uncertainties on our predictions for both satellites are quite small ($\lesssim$50 mas) through the
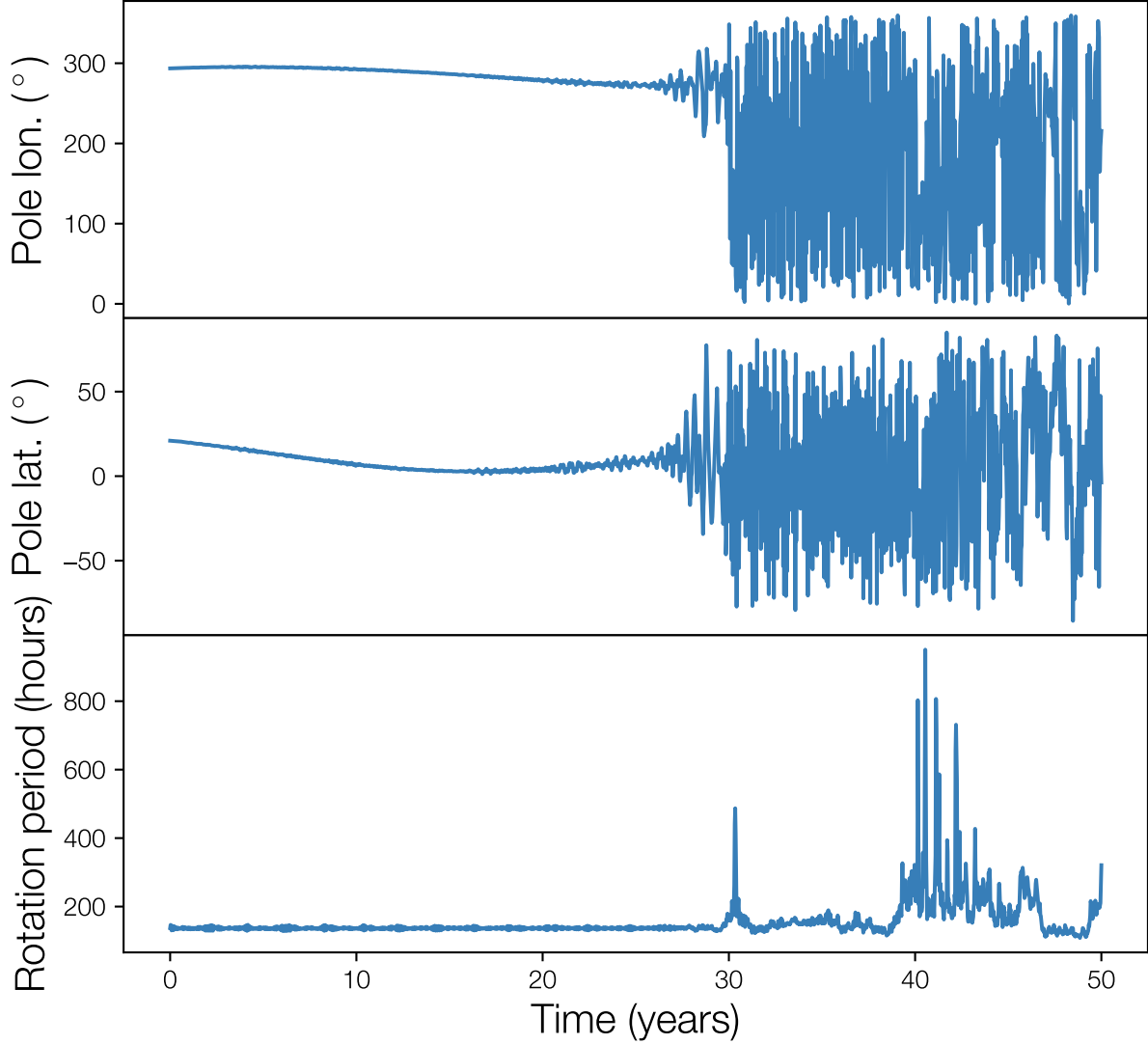
Figure 8. Chaotic rotation of Namaka. When initialized, Namaka rotates once every 6 hours and is aligned with its orbit. After just a few decades, Namaka becomes attitude unstable and begins to tumble. Chaos is a natural consequence of Namaka's eccentric orbit and is inevitable if Namaka has been substantially despun. In this sense, Namaka is very similar to Saturn's satellite Hyperion, which chaotically rotates due to its eccentric orbit around Saturn (Wisdom et al. 1984; Klavetter 1989).

2020s until 2030, at which time, the uncertainties begin to grow rapidly, especially for Namaka. By 2035, uncertainties on Namaka's position are of order ∼0.1 arcseconds. Rapid growth in uncertainty is attributable to the large degeneracy in our model (see Table 2 and Figure 3).

To ascertain whether future observations may be able to break the degeneracies in our fits, we have analyzed an ephemeris (similar to that presented above) where the predicted positions are also a function of Haumea's

J_2 (or equivalently Hi'iaka's mass). We find that the future positions of Hi'iaka and Namaka are strong functions of Haumea's J_2 indicating that the degeneracy will be broken with additional HST observations. Based on the HST+Keck fits, we can roughly estimate that ∼2-4 new epochs of observations are necessary to constrain Haumea's J_2 with ∼10% precision. Thus, future high-precision astrometric observations will allow future works to probe Haumea's interior and place strong constraints on its differentiation. Past work has shown that

Table 3. System Ephemeris

Julian Date	Date	Δx_N (")	Δy_N (")	$\sigma_{\Delta x_N}$ (")	$\sigma_{\Delta y_N}$ (")	r_N (")	σ_{r_N} (")	Δx_H (")	Δy_H (")	$\sigma_{\Delta x_H}$ (")	$\sigma_{\Delta y_H}$ (")	r_H (")	σ_{r_H} (")
2453371.500	2005-01-01 00:00:00	0.068	−0.190	0.002	0.005	0.202	0.004	0.057	0.649	0.001	0.003	0.651	0.003
2453371.833	2005-01-01 08:00:00	0.068	−0.121	0.002	0.005	0.139	0.004	0.043	0.600	0.001	0.003	0.601	0.003
2453372.167	2005-01-01 16:00:00	0.068	−0.051	0.002	0.005	0.085	0.003	0.029	0.549	0.001	0.003	0.550	0.003
2453372.500	2005-01-02 00:00:00	0.067	0.019	0.002	0.005	0.069	0.002	0.015	0.497	0.001	0.003	0.497	0.003
2453372.833	2005-01-02 08:00:00	0.065	0.090	0.002	0.006	0.111	0.004	0.000	0.444	0.001	0.003	0.444	0.003
2453373.167	2005-01-02 16:00:00	0.062	0.159	0.002	0.006	0.171	0.005	−0.014	0.391	0.001	0.003	0.391	0.003
2453373.500	2005-01-03 00:00:00	0.059	0.227	0.002	0.006	0.234	0.005	−0.028	0.336	0.001	0.003	0.337	0.003
2453373.833	2005-01-03 08:00:00	0.055	0.291	0.002	0.006	0.296	0.005	−0.042	0.281	0.001	0.003	0.284	0.003
2453374.167	2005-01-03 16:00:00	0.051	0.352	0.002	0.005	0.355	0.005	−0.056	0.225	0.001	0.003	0.232	0.003
2453374.500	2005-01-04 00:00:00	0.045	0.407	0.002	0.005	0.410	0.005	−0.070	0.168	0.001	0.004	0.182	0.003

NOTE—The predicted right ascension and declination positions of Namaka (N) and Hi'iaka (H) from 2005 to 2035. Δx and Δy are the predicted right ascension and declination, r is the total separation, and σ are the uncertainties on each value. All values are given in arcseconds. Predicted positions, separations, and uncertainties are taken from a sample of 500 random posterior draws. We display the first 10 rows of the table with the rest of the table available as a machine-readable table.

timing observations at certain, well-selected times can substantially improve the quality of the resulting orbit fits (Proudfoot et al., submitted). These times occur when the uncertainties in $\Delta\alpha\cos\delta$ and $\Delta\delta$ in Table 3 are at (local) maximum. We recommend that continued observations be taken by HST to prevent any systematic errors from arising, as we found in our HST+Keck fits.

Using a high resolution ephemeris from 2009-2020, we can evaluate past predictions of mutual events in light of our new orbit solution. We find that the mutual event predictions made in RB09 are generally accurate, even given their sign error in the system astrometry. We predict events that are similar in depth and duration, but are somewhat offset in time. The timing differences are only a few hours in 2009-2011, but steadily grow to tens of hours by the end of the mutual event season. Since the mutual event timings are quite sensitive to Namaka's eccentricity, and we find an eccentricity ∼15% lower than previously found, it is unsurprising that we find timing differences. The next mutual event season will occur in approximately half a heliocentric Haumea orbit, about midway through the 2200s. The exact timeframe will be dependent on Namaka and Hi'iaka's precise precession rates, which future observations will be able to precisely measure.

6. CONCLUSION

Using a state-of-the-art orbit fitter, `MultiMoon`, combined with several new epochs of observations from Keck and HST, we have refit the orbits of Haumea's satellites. The model we use can account for both satellite-satellite interactions and Haumea's oblate gravitational field. We find that unaccounted systematic errors are present

when fitting to the combined HST and Keck datasets, even when using robust statistical techniques that can account for some types of systematics. Although the HST+Keck fit can precisely constrain Haumea's J_2 and the masses of Hi'iaka and Namaka, we discount these fits since they have unreasonably high residuals and predict physically unrealistic values for Haumea's J_2. On the other hand, our orbit fit to only the HST data is more precise. Unfortunately, this fit suffers from a degeneracy between Hi'iaka's mass and Haumea's J_2, preventing a precise measurement of these two parameters.

For our HST only orbit fit, we detect Haumea's J_2 at ∼2.5σ confidence ($J_2 = 0.262^{+0.103}_{-0.112}$). Our fits are unable to discriminate between either a homogeneous or differentiated interior, but only a few additional epochs of precise astrometric observations will easily provide the precision to distinguish between these models. Our fit has also provided a measurement of Haumea's rotational pole $(\alpha_p, \delta_p) = (282.9^{+0.6\circ}_{-0.7}, -9.7^{+0.6\circ}_{-1.0})$, which lies extremely close to the orbit pole of Haumea's ring (Ortiz et al. 2017). In this sense, we presume that Haumea's ring lies in Haumea's equatorial plane and is minimally perturbed by Hi'iaka and Namaka. Determining Haumea's pole allows us to place tight constraints on the inclination of the satellites w.r.t. Haumea's equator, showing that Hi'iaka and Namaka are inclined by approximately $1.01^{+0.66\circ}_{-0.47}$ and $12.79^{+1.01\circ}_{-0.58}$, respectively. Both Hi'iaka and Namaka are on somewhat excited orbits, shown in both their inclination and eccentricity, hinting at past dynamical excitation (Ćuk et al. 2013).

Using our orbit fits, we have also characterized the rotational dynamics of the Haumea system using the spin-orbit integrator `SPINNY` (Ragozzine et al., submit-

ted). We find that Haumea's rotation axis precesses $< 0.5°$ on $\sim$kyr timescales, and is most strongly coupled to Hi'iaka's slow precession due to Haumea's J_2. Hi'iaka is expected to strongly precess on decadal timescales, which should have strong effects on the evolution of its light curve. Namaka is expected to rotate extremely slowly, based on both dynamical/tidal arguments and preliminary studies of its light curve. This putative slow rotation implies that Namaka chaotically rotates due to its significantly eccentric orbit.

To enable future observations of the Haumea system we have generated a satellite ephemeris over the next decade. These observations will enable a probe of Haumea's interior, aid in understanding the spin states of Haumea's satellites, and continue to provide insights into Haumea's formation. Understanding the Haumea system as a whole is crucial for understanding large TNO formation and evolution. The production of satellites and satellite systems seems to be ubiqitous across the transneptunian region, but the processes at play are still not well-explored. Thankfully, continued observations of Haumea and its satellites will enable deeper knowledge of the far reaches of our solar system.

REFERENCES

Abedin, A. Y., Kavelaars, J., Petit, J.-M., et al. 2022, The Astronomical Journal, 164, 261

Arakawa, S., Hyodo, R., & Genda, H. 2019, Nature Astronomy, 3, 802

Bagheri, A., Efroimsky, M., Castillo-Rogez, J., et al. 2022, Advances in Geophysics, 63, 231

Barkume, K., Brown, M., & Schaller, E. 2006, The Astrophysical Journal, 640, L87

Barr, A. C., & Schwamb, M. E. 2016, Monthly Notices of the Royal Astronomical Society, 460, 1542

Brown, M., & Suer, T.-A. 2007, International Astronomical Union Circular, 8812, 1

Brown, M., Bouchez, A., Rabinowitz, D., et al. 2005, The Astrophysical Journal, 632, L45

Brown, M. E., Van Dam, M., Bouchez, A., et al. 2006, The Astrophysical Journal, 639, L43

Burkhart, L. D., Ragozzine, D., & Brown, M. E. 2016, The Astronomical Journal, 151, 162

Campo Bagatin, A., & Benavidez, P. G. 2012, Monthly Notices of the Royal Astronomical Society, 423, 1254

22 Proudfoot et al.

Campo Bagatin, A., Benavidez, P. G., Ortiz, J., & Gil-Hutton, R. 2016, Monthly Notices of the Royal Astronomical Society, 461, 2060

Christy, J. W., & Harrington, R. S. 1978, Astronomical Journal, vol. 83, Aug. 1978, p. 1005, 1007, 1008., 83, 1005

Ćuk, M., Ragozzine, D., & Nesvorný, D. 2013, The Astronomical Journal, 146, 89

Dunham, E., Desch, S., & Probst, L. 2019, The Astrophysical Journal, 877, 41

Elliot, J. L., Person, M. J., Zuluaga, C., et al. 2010, Nature, 465, 897

Foreman-Mackey, D., Hogg, D. W., Lang, D., & Goodman, J. 2013, Publications of the Astronomical Society of the Pacific, 125, 306

Foreman-Mackey, D., et al. 2016, J. Open Source Softw., 1, 24

Foreman-Mackey, D., Farr, W. M., Sinha, M., et al. 2019, arXiv preprint arXiv:1911.07688

Gladman, B., & Volk, K. 2021, Annual Review of Astronomy and Astrophysics, 59, 203

Gourgeot, F., Carry, B., Dumas, C., et al. 2016, Astronomy & Astrophysics, 593, A19

Grundy, W., Porter, S., Benecchi, S., et al. 2015, Icarus, 257, 130

Hastings, D. M., Ragozzine, D., Fabrycky, D. C., et al. 2016, The Astronomical Journal, 152, 195

Hogg, D. W., Bovy, J., & Lang, D. 2010, arXiv preprint arXiv:1008.4686

Johnson, T., & McGetchin, T. 1973, Icarus, 18, 612

Kiss, C., Marton, G., Farkas-Takács, A., et al. 2017, The Astrophysical Journal Letters, 838, L1

Klavetter, J. J. 1989, Astronomical Journal (ISSN 0004-6256), vol. 97, Feb. 1989, p. 570-579., 97, 570

Konopacky, Q., Ghez, A., Barman, T., et al. 2010, The Astrophysical Journal, 711, 1087

Lacerda, P. 2009, The Astronomical Journal, 137, 3404

Laskar, J. 1997, A&A, 317, L75

Leinhardt, Z. M., Marcus, R. A., & Stewart, S. T. 2010, The Astrophysical Journal, 714, 1789

Marzari, F. 2020, Astronomy & Astrophysics, 643, A67

McKinnon, W. B., Prialnik, D., Stern, S. A., & Coradini, A. 2008, The solar system beyond Neptune, 1, 213

Morgado, B., Sicardy, B., Braga-Ribas, F., et al. 2023, Nature, 614, 239

Nesvornỳ, D. 2015, The Astronomical Journal, 150, 68

Nesvorný, D. 2018, Annual Review of Astronomy and Astrophysics, 56, 137

Noll, K. S., Grundy, W. M., Chiang, E. I., Margot, J.-L., & Kern, S. D. 2007, arXiv preprint astro-ph/0703134

Noviello, J. L., Desch, S. J., Neveu, M., Proudfoot, B. C., & Sonnett, S. 2022, The Planetary Science Journal, 3, 225

Ortiz, J., Thirouin, A., Campo Bagatin, A., et al. 2012, Monthly Notices of the Royal Astronomical Society, 419, 2315

Ortiz, J. L., Santos-Sanz, P., Sicardy, B., et al. 2017, Nature, 550, 219

Parker, A. H., Buie, M. W., Grundy, W. M., & Noll, K. S. 2016, The Astrophysical Journal Letters, 825, L9

Pereira, C., Sicardy, B., Morgado, B., et al. 2023, Astronomy & Astrophysics, 673, L4

Pike, R. E., Proudfoot, B. C. N., Ragozzine, D., et al. 2020, Nature Astronomy, 4, 89

Proudfoot, B., & Ragozzine, D. 2021in , 107–10

Proudfoot, B., & Ragozzine, D. 2022, Nature Communications, 13, 2262

Proudfoot, B. C., & Ragozzine, D. 2019, The Astronomical Journal, 157, 230

Quillen, A. C., Kueter-Young, A., Frouard, J., & Ragozzine, D. 2016, MNRAS, 463, 1543

Rabinowitz, D. L., Barkume, K., Brown, M. E., et al. 2006, The Astrophysical Journal, 639, 1238

Ragozzine, D., & Brown, M. E. 2009, AJ, 137, 4766

Ragozzine, D., & Wolf, A. S. 2009, The Astrophysical Journal, 698, 1778

Scheeres, D., Williams, B. G., & Miller, J. K. 2000, Journal of Guidance, Control, and Dynamics, 23, 466

Service, M., Lu, J., Campbell, R., et al. 2016, Publications of the Astronomical Society of the Pacific, 128, 095004

Vilenius, E., Kiss, C., Müller, T., et al. 2014, Astronomy & Astrophysics, 564, A35

Wisdom, J., Peale, S. J., & Mignard, F. 1984, Icarus, 58, 137

Wizinowich, P. L., Le Mignant, D., Bouchez, A. H., et al. 2006, PASP, 118, 297

Yelda, S., Lu, J. R., Ghez, A. M., et al. 2010, The Astrophysical Journal, 725, 331

Yoder, C. F. 1995, 1

Chapter 5

Beyond Point Masses V: Contact Binaries and Hierarchical Triples among the Cold Classicals

5.1 Introduction

The Cold Classical Kuiper belt (CCKB) is a population of dynamically 'cold' TNOs orbiting with semi-major axes ~42-47 au and inclinations $\lesssim 5°$. The CCKB is thought to be the least processed TNO population, with most objects believed to be primordial [8, 27, 86, 87]. Among the CCKB, binaries are common [40]. CCKB binary systems (CCKBBs) are generally nearer-equal size, more widely separated, and less masssive than binaries in other TNO populations [14]. Members of the CCKB have distinct colors when compared to other TNO populations [9–11, 86]. These aspects indicate that the planetesimal formation processes in the CCKB must be somewhat unique.

Over the past few years, a flurry of studies have been published showing that the Streaming Instability (SI) model of planetesimal formation is the dominant formation mechanism in the

outer solar system [8, 20, 33, 34]. The SI model is easily able to explain a variety of observations, including the size distribution of small TNOs [37, 38], the existence and abundance of binary systems [20, 33, 34, 39], the orbital orientation of binaries [20, 46], and many more (e.g., [83]). Formation by the SI, however, is obscured in most TNO subpopulations by additional collisional or accretional processes. Thus in contrast, the CCKB, as the least altered TNO population, is the perfect laboratory for understanding more about the formation of planetesimals by the SI.

As simulations of SI-triggered gravitational collapse have become higher-resolution, studies have consistently found that the SI model predicts the existence of many hierarchical system (i.e. systems with more than two gravitationally bound components) [33, 34, 39]. Current generation simulations lack the depth to fully explore these systems, especially at close separations, but initial estimates show that hierarchical systems could make up 10% (or more) of all binary systems formed via the SI [34]. Thus far, however, only one such system (Lempo) has been definitively identified [88].

The discovery of the Lempo triple system is particularly relevant to this work. Lempo was first identified as a binary system in 2001 [89], using medium resolution instruments on HST. However, subsequent observations in the following years showed a distinct elongation of the 'primary' component [90]. Upon imaging the system at the highest possible resolution (using HST's ACS/HRC), it was discovered that the primary was actually two individual components [88], which were orbited by the previously identified satellite. In Lempo's case, imaging was able to resolve the true system architecture, but Lempo is probably just the largest (and most resolvable) example of such systems. More typical hierarchical systems are likely to be much more compact, as shown in SI formation simultaions [34, 39].

Fortunately, non-Keplerian orbit fitting of known CCKBBs has the potential to surpass the resolution limit, allowing discovery of hierarchical systems at separations that are currently unresolvable. In Chapter 3, we conducted a large pilot study to determine whether non-Keplerian effects

Architecture		Nomenclature	Example
⬤	•	Planet-moon	Haumea
⬤	⬤	Near-equal binary	Sila-Nunam
⬤⬤	⬤	Contact hierarchical triple	Dinkinesh
⬤ ⬤	⬤	Hierarchical triple	Lempo

Figure 5.1 A schematic showing the nomenclature we use in this Chapter. Broadly, we refer to both hierarchical triples and contact hierarchical triples as 'hierarchical systems'. The examples given in the right column are well studied/imaged systems in either the TNO or asteroid populations. Of particular note is Dinkinesh, an asteroid where the smaller component is known to be a contact binary itself. Dinkinesh's binary/trinary nature was only recently discovered in November 2023 during a flyby of the system by the *Lucy* spacecraft.

were detectable in the orbits of TNBs. There, we identified several CCKBBs that had detectable non-Keplerian effects. The non-Keplerian motion in these systems was best explained by the presence of unresolved system components. In that same study, we also identified that Borasisi-Pabu is likely a hierarchical system (albeit a contact binary orbited by a third body). In this work, we continue the analysis started in Chapter 3, and focus on CCKBBs. Our goal is to determine if any of the currently known CCKBBs are actually hierarchical systems that have not yet been resolved.

As a note on nomenclature, in this Chapter we use various terms such as hierarchical triple, contact hierarchical triple, near-equal binary, and more. In Figure 5.1, we show a schematic describing system architectures we explore in this paper. When we use the term 'hierarchical system' we refer to both hierarchical triples and contact hierarchical triples. We also often use the

term unresolved system component. By this, we refer to the close-in component in a hierarchical system, not undiscovered components at wide separation from the rest of the known system.

5.2 Methods

In this work, our sample consists of 16 of the 28 CCKBBs with known orbit solutions. This sample selection was based on availability of data, ease of interpretation, and quality of orbit fit. Each CCKBB in our sample has, at minimum, six publicly available, high-resolution relative astrometric measurements, ensuring that our model fitting problem is well-posed (i.e., not underconstrained). We also remove from our sample all CCKBBs with a mirror ambiguous orbit. This sample of CCKBBs is made up of a variety of different morphologies, spanning a wide range in mass, separation, and orbital characteristics. Although we make every attempt to make our sample as unbiased as possible, there are still strong biases in our sample from a variety of sources. For example, brighter CCKBBs are easier to observe, and so will naturally be overrepresented in our analysis. Likewise, ultra-wide binary systems, which are easier to observe due to their large separation, will have far more data than systems with smaller component separations. While this complicates population-level interpretation of our analysis, trends and discoveries at the sample/ensemble level are still informative.

In addition to the sample of new non-Keplerian orbit fits we complete here, we also use completed non-Keplerian orbits for (66652) Borasisi-Pabu and (148780) Altjira that were completed in other work (Proudfoot et al., submitted [Chapter 3], and Nelsen et al., in prep.). Results from those fits are presented, with the fits we complete here, in Section 5.3.

For our orbit fitting, we draw astrometry from the Orbit Status of Known Binary TNOs database (http://www2.lowell.edu/users/grundy/tnbs/status.html). We also use new, unpublished observations of many of our targets. For brevity, we do not explicitly list all of the data, but rather point the

reader to the Orbit Status database. New observations used in this work will be available there after the publication of this work.

New observations of several of our targets were acquired at the W.M. Keck Observatory on Mauna Kea. These observations used the laser guide star adaptive optics system (LGS AO) with the near-infrared (NIR) NIRC2 camera. Observations used nearby appulse stars for the necessary tip-tilt corrections. All observations were taken in the NIR H filter, covering wavelengths from $\sim$1.48-1.77 μm. Between exposures, the telescope was dithered to enable sky subtraction and to minimize localized detector effects (e.g., bad/hot pixels). Relative astrometry from each sequence of observations was extracted using Gaussian PSF fitting techniques, using a mean plate scale of 9.952 milliarcseconds/pixel and an orientation offset of $0.252°$ [91–93]. Both the observational set-up and method for extracting astrometry have been extremely well-characterized and validated over many years and are considered the gold-standard of ground-based binary observations.

5.2.1 MultiMoon

To perform our non-Keplerian orbit analysis, we use `MultiMoon`, an advanced non-Keplerian orbit fitter built on a Bayesian framework. `MultiMoon` uses a powerful spin-orbit integrator which can numerically integrate the orbital motion of an arbitrary number of bodies with quadrupole shapes. `MultiMoon` performs Bayesian parameter inference using the popular `emcee` package [94, 95].

For our orbit fits, we use `MultiMoon`'s default χ^2 likelihood function. The likelihood evaluation relies on a simple non-Keplerian orbit model which models a CCKBBs mutual orbit and the system primary's shape and spin pole. To characterize the system primary's shape, we use include the J_2 gravitational harmonic, which describes the oblateness of the body. This is generally adequate to describe the body's rotationally averaged gravitational field. Although the connection between shape, gravitational harmonics, and non-Keplerian motion is more complex for hierarchical systems,

the concepts are generally applicable. For more details on how hierarchical systems can be modeled, see the introduction to Chapter 3.

Our model is thus defined by 11 individual free parameters: primary mass (M_1), secondary mass (M_2), semi-major axis (a), eccentricity (e), inclination (i), argument of periapse (ω), longitude of the ascending node (Ω), mean anomaly at epoch ($\mathcal{M}$), primary zonal gravitational harmonic (J_2), primary rotation axis obliquity (i_{sp}), and primary rotation axis precession (Ω_{sp}). In addition to these free parameters, the rotation rate of the primary (in radians per second) is provided to `MultiMoon` as a fixed parameter. For our targets, light curve periods are used as a proxy for primary rotation period under the assumption that the light curve is dominated by the primary's rotation. For systems without a known light curve period, we use a default value of 10 hours. Our testing clearly shows that the input rotation rate has virtually no effect on the orbit fitting process, justifying these assumptions.

As `MultiMoon` uses a Bayesian framework, priors need to be specified during the fitting process. For all of our systems, we use flat, uninformative priors that only constrain our systems to physically possible values (e.g., positive mass, bound orbits, etc.). Since mass and primary J_2 are degenerate (since precession is proportional to $M \times J_2$), we enforce a prior where $M_1 > M_2$, to simplify exploration of the parameter space, consistent with past successful `MultiMoon` analyses. Like previous studies (see Chapter 3), we also restrict our exploration to prograde solutions of the primary's rotation axis (i.e., rotation axis and orbit pole are $< 90°$ apart). Retrograde solutions exist and are exact mirrors to the prograde solutions, but their inclusion complicates exploration of the posterior distribution as they create a strongly multi-modal posterior.

When performing our `MultiMoon` orbit fits, we used 980 walkers (selected to match our computational hardware) to analyze each system. Initial walker positions were chosen to cluster around the best fits from preliminary fits. We initialized walkers with a 10,000 step burn-in, after which poorly performing walkers were pruned and replaced. After another 5000 step burn-in was

completed, we then ran the ensemble for, at minimum, 15000 steps. Some systems converged more slowly than average, so more steps were used in some cases. Convergence was assessed by visual inspection of walker trace plots and parameter likelihood plots. The fitting process was repeated many times with different walker starting positions to ensure that the global minimum was found by our fits.

5.3   Non-Keplerian Orbit Fits

Out of the 16 CCKBBs we attempted to fit with non-Keplerian orbits, 13 systems had usable non-Keplerian orbits. Out of those 13, four had statistically significant detections of non-Keplerian motion, while the rest had upper limits on J_2. Combined with the two detections from Borasisi-Pabu and Altjira, we have a total of six detections of non-Keplerian motion ((66652) Borasisi-Pabu, (88611) Teharonhiawako-Sawiskera, (148780) Altjira, (525462) 2005 EO$_{304}$, 1999 RT$_{214}$, and 2006 BR$_{284}$). These detections can roughly be broken into two separate groups based on mutual orbit period: those with orbit periods of $\sim$100 days, and those with orbit periods of $\gtrsim$1000 days. For the rest of this Chapter, we call these the 'wide' binaries and the 'ultra-wide' binaries, respectively.

The results of our non-Keplerian orbit fits are shown below. For CCKBBs with significant detection of non-Keplerian motion, we show the full orbit solutions. These are in Table 5.3 for the wide binaries, and in Table 5.3 for the ultra-wide binaries. We also display the corner plot of one wide TNB (1999 RT$_{214}$) and one ultra-wide TNB (2005 EO$_{304}$) in Figures 5.2 and 5.3, respectively. A corner plot displays the marginal posterior for each parameter along the top of each column, as well as 2-dimensional joint posteriors for every combination of parameters in 2-dimensional histograms. For TNBs where only upper limits can be placed our results are shown in Table 5.3. There we show the mass posterior as well as the J_2R^2 upper limits (characterized as 1 and 3σ limits).

Table 5.1. Non-Keplerian Orbit Solutions for the wide Binary Detections

Parameter		1999 RT$_{214}$	Altjira	Borasisi
Mass, Primary (10^{18} kg)	M_1	$0.142^{+0.037}_{-0.031}$	$2.728^{+0.794}_{-0.521}$	$2.293^{+0.667}_{-0.416}$
Mass, Secondary (10^{18} kg)	M_2	$0.057^{+0.03}_{-0.037}$	$1.317^{+0.521}_{-0.794}$	$1.159^{+0.416}_{-0.668}$
Semi-major axis (km)	a	3426^{+71}_{-67}	9985^{+30}_{-30}	4538^{+13}_{-13}
Eccentricity	e	$0.2924^{+0.0234}_{-0.0230}$	$0.3511^{+0.0025}_{-0.0024}$	$0.4690^{+0.0018}_{-0.0018}$
Inclination (°)	i	$24.45^{+1.40}_{-1.31}$	$25.11^{+0.21}_{-0.21}$	$51.28^{+1.92}_{-1.28}$
Argument of periapse (°)	ω	$76.2^{+9.6}_{-7.4}$	$191.69^{+0.46}_{-0.45}$	$139.31^{+1.03}_{-1.32}$
Longitude of the ascending node (°)	Ω	$77.9^{+4.4}_{-4.4}$	$274.21^{+0.31}_{-0.31}$	$86.02^{+1.17}_{-1.20}$
Mean anomaly at epoch (°)	$\mathcal{M}$	$326.2^{+7.6}_{-12.0}$	$124.26^{+0.40}_{-0.41}$	$336.24^{+0.98}_{-0.85}$
Zonal harmonic strength (km^2)	J_2R^2	9489^{+8389}_{-4846}	17690^{+8620}_{-6916}	7706^{+4400}_{-3016}
Rotation axis obliquity (°)	i_{sp}	$40.2^{+37.5}_{-25.6}$	$19.4^{+5.7}_{-5.6}$	$84.8^{+11.3}_{-11.7}$
Rotation axis precession (°)	Ω_{sp}	$44.1^{+265.1}_{-28.4}$	$245.1^{+18.7}_{-36.4}$	$117.6^{+15.8}_{-25.8}$
System mass (10^{18} kg)	M_{sys}	$0.199^{+0.013}_{-0.011}$	$4.046^{+0.036}_{-0.036}$	$3.451^{+0.029}_{-0.029}$
Primary obliquity (°)	ϕ	$33.2^{+31.8}_{-16.9}$	$14.0^{+11.0}_{-6.1}$	$45.0^{+6.6}_{-4.7}$

Note. — All fitted angles are relative to the J2000 ecliptic plane. All system parameters are defined at the following epochs: 2014 December 8 12:00 UT (1999 RT$_{214}$), 2007 July 18 12:00 UT (Altjira), and 2000 December 21 12:00 UT (Borasisi). The fits for Altjira and Borasisi are taken from Nelsen et al. (in prep) and Proudfoot et al. (submitted).

Table 5.2.   Non-Keplerian Orbit Solutions for the Ultra-wide Binary Detections

Parameter		Teharonhiawako	2005 EO$_{304}$	2006 BR$_{284}$
Mass, Primary (10^{18} kg)	M_1	$1.721^{+0.462}_{-0.365}$	$1.495^{+0.385}_{-0.315}$	$0.409^{+0.106}_{-0.088}$
Mass, Secondary (10^{18} kg)	M_2	$0.714^{+0.365}_{-0.462}$	$0.602^{+0.315}_{-0.385}$	$0.163^{+0.088}_{-0.106}$
Semi-major axis (km)	a	27589^{+121}_{-126}	69433^{+317}_{-377}	25256^{+160}_{-169}
Eccentricity	e	$0.2487^{+0.0020}_{-0.0020}$	$0.2147^{+0.0021}_{-0.0018}$	$0.278^{+0.0053}_{-0.0042}$
Inclination (°)	i	$127.02^{+0.58}_{-0.65}$	$12.54^{+0.33}_{-0.37}$	$55.35^{+0.67}_{-0.66}$
Argument of periapse (°)	ω	$302.64^{+1.51}_{-1.20}$	$209.33^{+2.44}_{-2.40}$	$13.78^{+0.58}_{-0.57}$
Longitude of the ascending node (°)	Ω	$36.25^{+0.73}_{-0.80}$	$258.61^{+1.11}_{-1.13}$	$41.60^{+0.68}_{-0.76}$
Mean anomaly at epoch (°)	$\mathcal{M}$	$275.55^{+0.85}_{-1.04}$	$276.42^{+1.52}_{-1.62}$	$182.21^{+0.70}_{-0.71}$
Zonal harmonic strength (10^6 km^2)	J_2R^2	$1.98^{+1.73}_{-1.15}$	$24.90^{+14.34}_{-9.24}$	$3.46^{+2.43}_{-1.65}$
Rotation axis obliquity (°)	i_{sp}	$126.7^{+19.3}_{-30.8}$	$59.2^{+16.0}_{-20.4}$	$96.4^{+24.7}_{-18.6}$
Rotation axis precession (°)	Ω_{sp}	$298.8^{+34.2}_{-59.5}$	$166.4^{+24.0}_{-27.1}$	$119.4^{+223.1}_{-95.1}$
System mass (10^{18} kg)	M_{sys}	$2.434^{+0.028}_{-0.028}$	$2.096^{+0.030}_{-0.029}$	$0.572^{+0.008}_{-0.008}$
Primary obliquity (°)	ϕ	$71.2^{+10.6}_{-18.8}$	$61.1^{+15.0}_{-20.4}$	$71.8^{+13.2}_{-21.4}$

Note. — All fitted angles are relative to the J2000 ecliptic plane. All system parameters are defined at the following epochs: 2001 March 31 12:00 UT (Teharonhiawako-Sawiskera), 2005 January 29 12:00 UT (2005 EO$_{304}$), and 2009 June 17 12:00 UT (2006 BR$_{284}$).
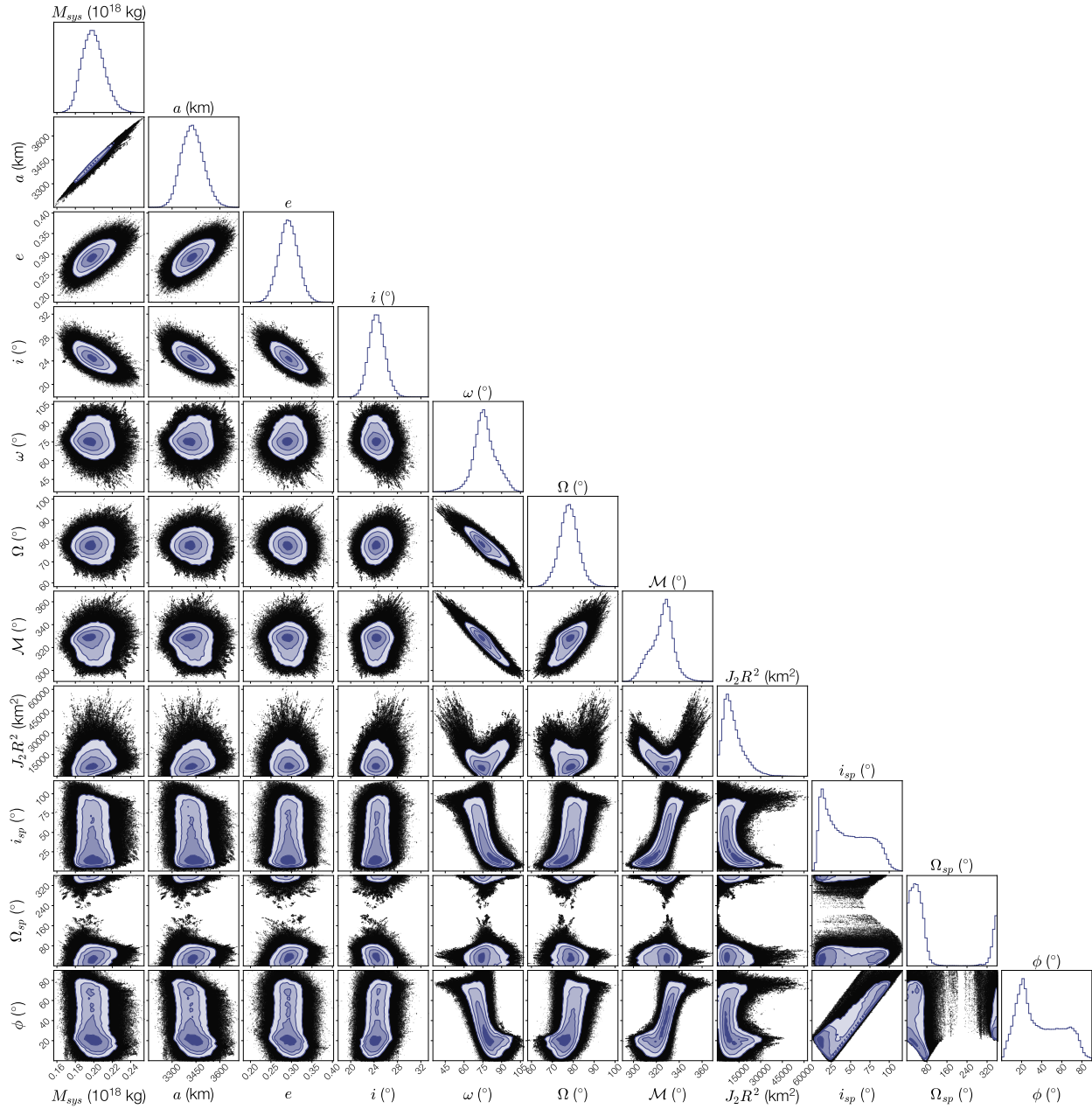
Figure 5.2 Corner plot for the 1999 RT$_{214}$ non-Keplerian orbit fit. The best fit in the `MultiMoon` non-Keplerian fit corresponded to a χ^2 of $\sim$9.5 a significant improvement over the Keplerian model ($\chi^2 \sim$18). The system mass (M_{sys}) is plotted–instead of individual masses–to better show parameter correlations. Parameters correspond to those shown in Table 5.3, with the final parameter (ϕ) corresponding to the primary obliquity with respect to the mutual orbit.

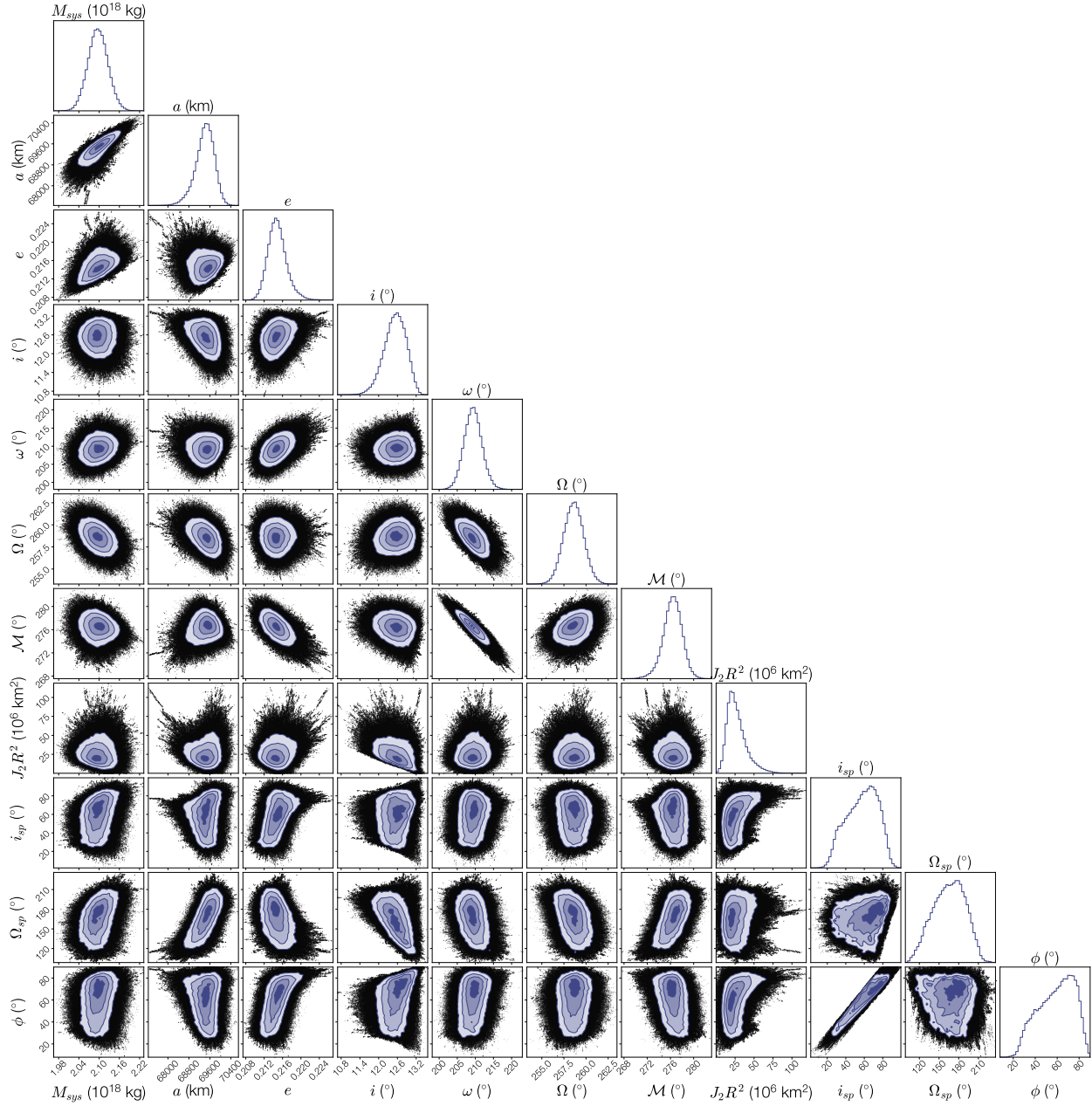Figure 5.3 Corner plot for the 2005 EO$_{304}$ non-Keplerian orbit fit in the style of Figure 5.2. The best fit in the `MultiMoon` non-Keplerian fit corresponded to a χ^2 of $\sim$105 a significant improvement over the Keplerian model ($\chi^2 \sim$118).

Table 5.3.   Upper Limits on Non-Keplerian Motion

Name/Designation	Mass	J_2R^2 1σ upper limit	J_2R^2 3σ upper limit
	(kg)	(km^2)	(km^2)
Logos-Zoe	$0.444^{+0.011}_{-0.011}$	91453	322373
‡Ką́gára-!Hãunu	$2.172^{+0.134}_{-0.120}$	42290	134986
2000 CQ114	$0.545^{+0.009}_{-0.008}$	165230	642992
2001 XR254	$4.052^{+0.087}_{-0.077}$	67124	221786
1999 OJ4	$0.407^{+0.008}_{-0.008}$	7538	19482
2001 QW322	$2.037^{+0.031}_{-0.030}$	64431523	184399508
2003 QY90	$0.517^{+0.028}_{-0.029}$	90188	243183
2003 UN284	$1.266^{+0.091}_{-0.085}$	11522684	37626839
2006 CH69	$1.208^{+0.112}_{-0.115}$	55258	171614

Note. — Mass and J_2R^2 upper limits are taken from our non-Keplerian orbit fits. 1σ and 3σ upper limits are defined as the 84th and 99th percentiles in the MCMC chains.
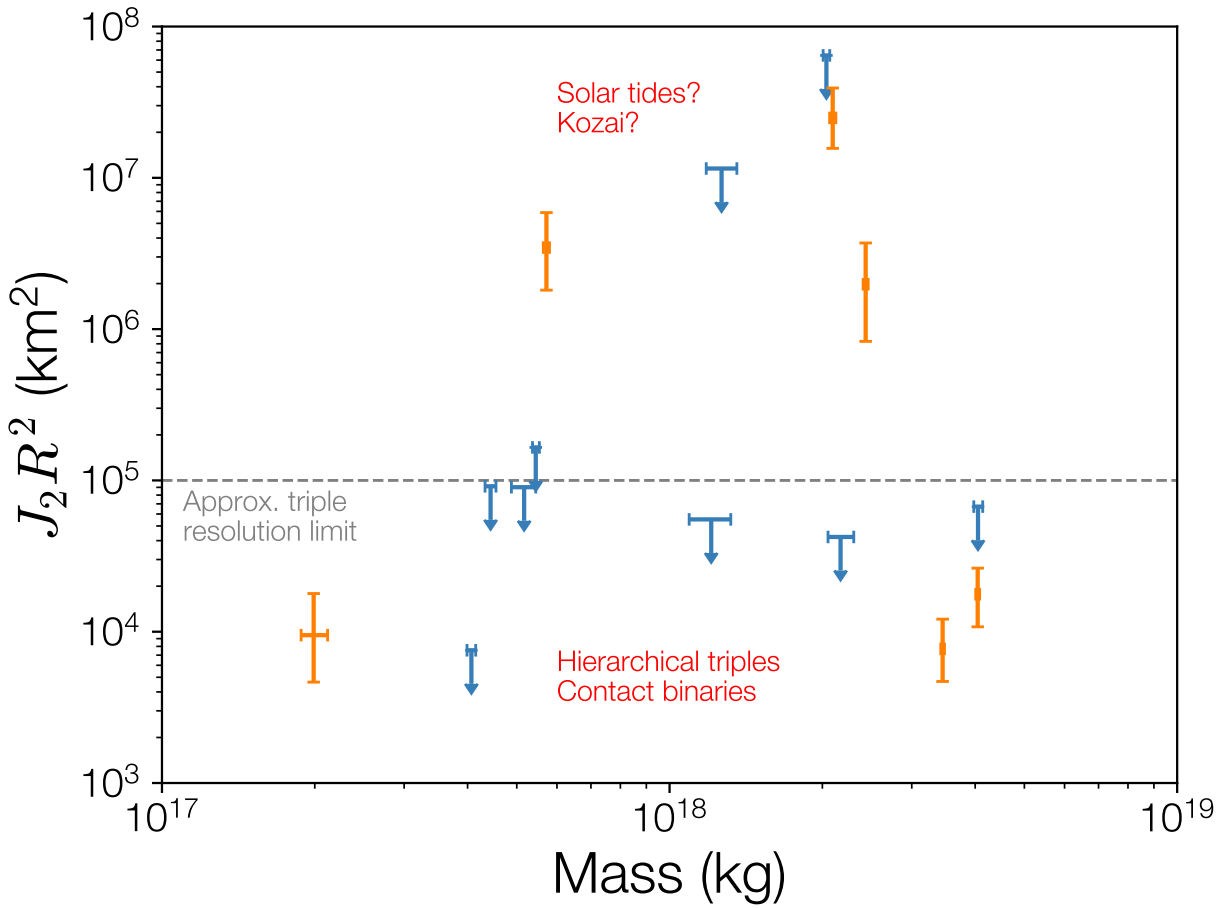
Figure 5.4 A summary of our non-Keplerian detections (in orange) and upper limits (in blue). Error bars and upper limits are 1σ bounds. The gray dashed line shows the approximate resolution limit of hierarchical triple systems with current telescopes ($\sim$1000 km).

Finally, we combine all our results in Figure 5.4, showing the J_2R^2 detections or upper limits as a function of mass.

Typically in non-Keplerian orbit fitting literature, results are shown as only J_2 (rather than J_2R^2). While this is extremely useful for quick and intuitive understanding of shape/gravitational field, it requires a definition for R. Across the literature, R is defined in a variety of ways including volumetric radius, equatorial radius, and more. Crucially, however, any definition implicitly assumes a shape model. Unfortunately, very little is known about the exact shapes of TNOs, as opposed to many fairly well-characterized asteroids. To remain agnostic to any shape models, and facilitate the exploration of arbitrary shapes, we present our results in terms of J_2R^2.

In addition to our 13 usable non-Keplerian fits, we also completed fits that were not generally usable. One main concern in these fits was the presence of multiple distinct orbit solutions. The ftting algorithm used by `MultiMoon` is extremely inefficient at exploring multimodal solutions, and interpreting the outputs is scientifically difficult. The presence of multiple orbital solutions is due to a degeneracy between J_2 and mass. Since J_2, in addition to causing precession, alters the mean motion of the system, multiple orbit solutions can emerge. Similarly, another issue was the complete lack of distinct orbital solutions. This occurs for the same reason, but is much more severe. Any fit in which we identified systematic issues has been removed from our analysis below. In the future, new observations of these systems will ameliorate these issues.

5.4   Shape Modeling

To inform our interpretation of the J_2R^2 measurements made, we have developed an analytical shape modeling tool that can simultaneously calculate the mass, J_2R^2, effective diameter, and surface area, of any shape, given a density. This allows us to explore possible interpretations of our non-Keplerian fits using a variety of shape models. To simplify our exploration, however, we focus on two simple

shape models representing the system as either a hierarchical triple or a contact hierarchical triple. While both system components can certainly contribute to the non-Keplerian motion in a system, we only model the primary. As discussed in Chapter 3, this is a justifiable assumption for most systems.

We also neglect to model the system primaries as single monolithic objects (i.e. not hierarchical systems). This decision is based on the high J_2R^2 values we find. A typical nonspherical monolithic object in the size range we are examining will have a $J_2R^2 \sim 1000$. Given our minimum J_2R^2 measurement of ~ 7500, we skip modeling of monolithic objects and move straight to hierarchical systems.

In this analysis, we represent a contact hierarchical triple by modeling the system primary as a contact binary. We do this using a geometrical figure called a Cassinoid, which looks like a dumbbell [96]. For reference, we display a Cassinoid in Figure 5.5. A Cassinoid is defined by just two values, *a* and *e*, which define the overall size (*a*) and the width of the central 'bridge' (*e*). A Cassinoid is a close approximation to the dumbbell equilibrium figure of a rapidy rotating strengthless body. Dumbbell equilibrium figures are well-known to describe the shapes of a variety of astrophysical systems including contact binary stars [97], and, importantly, contact binary asteroids [**?**, 96, 98, 99]. While a Cassinoid is not the perfect shape to match the morphology of a contact binary (see, for example, Arrokoth), we view it as a good starting point for analysis. Its simple algebraic definition and two governing parameters make it extremely amenable to simple shape modeling.

To model a hierarchical triple, we simply approximate the primary as two spheres with radius *r* and separation *a*. Although this neglects deformation of the two components from either their intrinsic shapes of tidally-induced bulges, the majority of the effective J_2R^2 of a compact binary is due to the components' separation. For an initial analysis, such as this, we find this simple model to be completely adequate.

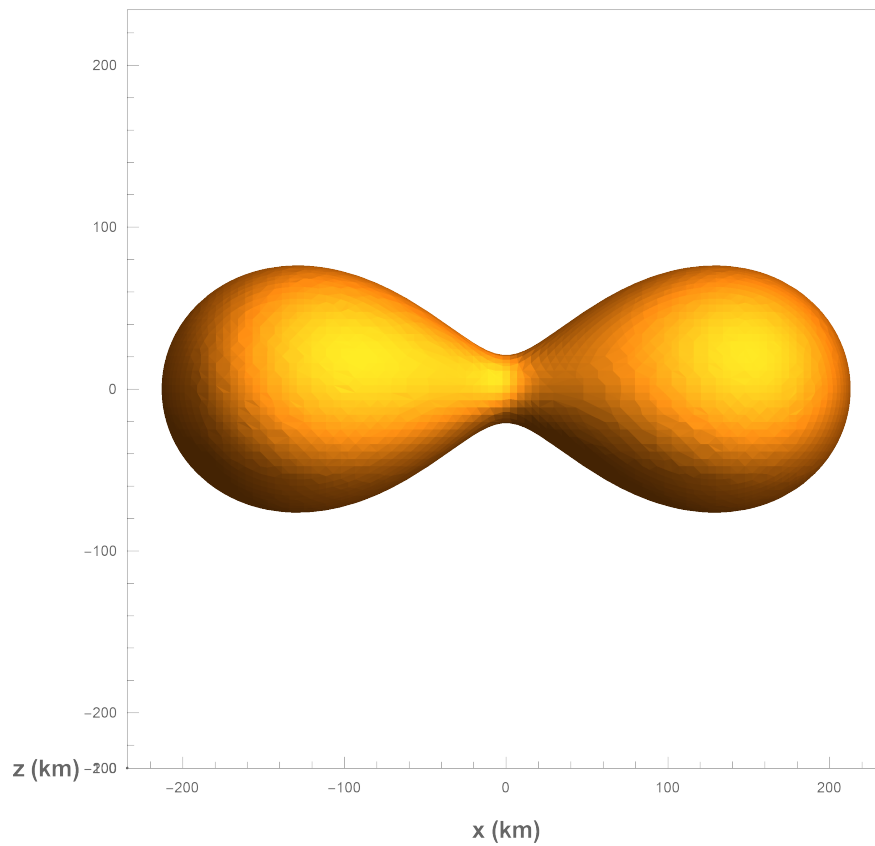Figure 5.5 A Cassinoid of size $a = 150$km and neck width parameter $e = 1.01$. Altering a changes the overall size, but does not alter the fundamental shape. Altering e changes the width of the neck, where $e = 1.0$ marks the transition from a single object to two separated object. A Cassinoid closely matches the dumbbell sequence of equilibrium shape models that describe a rapidly rotating strengthless body [96].

Our shape modeling tool relies on the popular software, Mathematica. Given a defined shape model, the tool calculates the total volume and surface area using numerical integration. This allows for a calculation of mass (given a density), effective diameter, and surface area (or radius of the surface area equivalent sphere). J_2R^2 is then found by calculating the moments of inertia of the body, again using numerical integration. By using this tool, along with a non-Keplerian orbit fit, plausible shape models can be generated and explored. Our process relies on first finding plausible shapes that can match the measured J_2R^2. Since the J_2R^2 of a shape does not depend on density, we can then constrain the density that shape would need to match the measured mass. If that density is implausibly low, we can rule out that shape model.

Using this technique, we can model the system architecture of our sample of wide CCKBBs. First, we start by modeling 1999 RT$_{214}$ as a contact hierarchical triple. Using the Cassinoid shape model with $e = 1.01$ (see Figure 5.5 for illustration of the shape), we find a minimum size a of $\sim$120 km based on the lower bound of the J_2R^2 measurement. Given the size of this Cassinoid and the mass measurement in Table 5.3, we find the maximum density of all compatible Cassinoids is $\sim$100 kg m^{-3}. Although uncertainties in the non-Keplerian fitting are relatively large, propagating them through our analysis does not change the minimum density of the Cassinoid significantly. In fact, since we already start our analysis using the lower bound on J_2R^2, the densities of most other compatible sizes are substantially lower. Given this tiny density, we find the Cassinoid shape model (i.e. the contact hierarchical architecture) to be inconsistent with our measurements. As an alternative, we can model the system as a hierarchical triple. The mass and J_2R^2 constraints are consistent with a central binary composed of two objects $\sim$30 km in radius, separated by 200-400 km, when assuming a density of 500 kg m^{-3}. For 1000 kg m^{-3}, the radii are $\sim$25 km.

Given these two shape models, the hierarchical triple model is far more realistic. Indeed, the only known hierarchical triple Lempo, has a very similar separation (as measured in primary radii) [88]. The compact binary (at the center of the hierarchical triple) is also very similar to other close

binaries discovered by occultations [100] and imaging from the *New Horizons* spacecraft. Given our modeling, as well as the knowledge that similar systems are currently known in the transneptunian region, we believe our analysis indicates that 1999 RT$_{214}$ is a hierarchical triple. Our analysis shows that the system is well within the undetectable regime of current telescopes.

Repeating a similar process for Altjira, when assuming a contact hierarchical triple architecture, we find a minimum size (*a*) of ~180 km, given the Cassinoid shape model. This yields a maximum density of 500 kg m^{-3}. While this sounds more reasonable than the previous case, most of the probability mass (in the J_2R^2 and mass posteriors) would impute a far lower density. Given the median value of J_2R^2, the density for this model would be closer to 200 kg m^{-3}. Assuming a hierarchical triple model, the primary would consist of a compact binary with separation of 300-450 km. For a density of 500 kg m^{-3} (1000 kg m^{-3}), the two components would be ~85 km (~70 km) in radius.

Selecting between these models is more difficult than the previous case. The presumed densities of the contact hierarchical triple solution are quite low, but are not completely unrealistic. Indeed, comets are known to have similarly low densities [101, 102]. In contrast, however, typical TNOs in a similar size range tend to have somewhat higher densities of 500-1000 kg m^{-3} [103]. As most of the probability mass implies quite low densities, we slightly prefer a hierarchical triple model of the system, but acknowledge that a contact triple is possible. In Nelsen et al. (in prep), `MultiMoon` was used to explore the hierarchical triple interpretation in more detail. They used a three-body model of the system in an attempt to fit the astrometry of the third, outer body. Excitingly, they found that a three-body model produced an excellent overall orbit fit, similar in quality to the non-Keplerian fit we reference in Table 5.3. They also found that viable system architectures were typically stable over the course of ~20 years. Stability may be a concern with the system we describe here, as the two components are only separated by a few primary radii. When compared with 1999 RT$_{214}$, Altjira is dynamically tighter as, although it is more widely separated in absolute terms, the relative

separation is less. Future work should examine the long-term stability of these hierarchical triples as their stability is quite poorly understood [104]. Insight from binary star literature may also prove helpful in understanding these systems' stability (e.g., [105]).

Lastly, we use our shape modeling tools on Borasisi. Under the contact triple model, and using the same Cassinoid shape, we find that even for the smallest overall size ($a \approx 115$km), we find a reasonable maximum density of >1000 kg m^{-3}. For the median value of J_2R^2, we find that a Cassinoid with overall size $a = 140$km yields a density of 800 kg m^{-3}. Further exploration of this shape model is possible, like exploring the Cassinoid neck width parameter, but we leave this to future work. Although it seems like a contact hierarchical triple is an adequate fit, we also explore the hierarchical triple model. The J_2R^2 posterior suggests a separation of 200-300 km, while the mass posterior suggests radii of 65 km or 80 km based on densities of 1000 kg m^{-3} or 500 kg m^{-3}, respectively. While this shape model can also explain the J_2R^2 measurement, it is unclear if a separation of <5 primary radii could be stable, especially given the presence of the perturbing Pabu. Selecting between these models will require further observation of the system.

A variety of techniques could be used to confirm the results we present for these three binaries. The most promising of which is observation of a multi-chord stellar occultation. A stellar occultation occurs when a TNO (or binary component) passes in front of a background star, momentarily dimming its light, in a manner akin to a solar eclipse. Simultaneously capturing these events from multiple observing locations can place strong constraints on the size and shape of objects. Observing an occultation of one of these binaries may reveal its system architecture in great detail. In fact, one of the tightest known TNBs was discovered by observing both components with a multi-chord occultation [100]. Another path to confirm these results may come from high-precision light curve observations and modeling. A recent study proposed that Manwe-Thorondor, a resonant TNB, is actually a contact hierarchical triple system based on detailed observations of its light curve [5]. Completing such an analysis of the systems we discuss here would be particularly informative.

Interpreting our detections of non-Keplerian motion for our three ultra-wide binaries is much simpler. Using a contact hierarchical triple model is completely unwarranted given the extremely large J_2R^2. For example, for Teharonhiawako the modeled Cassinoid would have a size of $\sim$2500km, about the size of the planet Mercury. The density would then have to be $<$1 kg m^{-3}, less dense than air. Clearly, a hierarchical triple is more warranted. Again, modeling Teharonhiawako, we find that the minimum separation of an equal-mass unresolved component would be $\sim$2000 km, well above the limit for detecting this component. Unfortunately, no such undetected component has been found, despite several observations with high-resolution ground and space based observatories (Keck and HST/WFC3). All four observations could have been unlucky, with the undetected component being at or near its minimum projected separation, but this is unlikely. We find it more likely that the detection of non-Keplerian motion is caused by systematic errors or is induced by the Sun's influence. We discuss the Sun's influence in Section 5.5. The other ultra-wide binaries have even larger measured values for J_2R^2, implying even greater separations for a putative undetected component. As with Teharonhiawako, these systems has also been surveyed with high-resolution observatories with no detection of additional components. 2005 EO$_{304}$ and 2006 BR$_{284}$ were even specifically surveyed for additional components in an effort to find triple systems. As such, we draw the same conclusion for these system.

5.5 Discussion

Recent studies have shown that hierarchical systems should be relatively common outcomes of planetesimal formation by the SI [33, 34, 39]. Indeed, one study found that hierarchical systems may make up a significant fraction of CCKBB systems ($\gtrsim$10%), after accounting for the limited resolution of their simulations [34]. While simulations of SI-triggered gravitational collapse are still

in their infancy, forthcoming work using high resolution simulations points towards the increased importance of hierarchical systems [106].

On the observational side, recent work has continually pointed toward the prevalence of close or contact binaries. Surveys of TNO light curves across a wide variety of populations have revealed that close and contact binaries are common [48–52]. Likewise, analysis from doublet cratering seen on Pluto and Charon by *New Horizons* imagery predicts that there is likely to be a very large popultation of compact binaries [107]. Additional surveys completed from within the CCKB by *New Horizons* has identified two close binaries [108]. Although not hierarchical systems, the existence of close and contact binaries is closely linked to hierarchical systems. For example, one possible formation pathway for lone contact (or compact) binaries is the ejection of the loosely bound component of a triple system. This may be especially relevant for dynamically unstable hierarchical triples where complex N-body interactions lead to ejection of the loosely bound component. Likewise, encounters between hierarchical systems and other TNOs (or even binaries) may play a large role in the creation of contact (and compact) binaries. Future work should closely examine the dynamics of the hierarchical systems produced in SI simulations to understand how they are linked to the known contact and compact binaries.

The work we have done here confirms, and extends, these results. Using our three detections of hierarchical systems, we calculate a lower bound on the fraction of triples among the CCKBBs of 11% (3 out of 28 CCKBBs with determined orbits). Although this number is extremely uncertain and subject to various biases, it is roughly in line with predictions from SI simulations [34].

Given the 3 detections here, our results can hardly place constraints on the SI model. But, in the future, with more detections of hierarchical systems, it may be possible that the observations of these systems will lead to better understanding of the SI model itself. For example, if the solid-to-gas ratio in the disk undergoing the SI has a distinct impact on the fraction of hierarchical systems produced, observations of these systems may play a key role in understanding the gas-to-solid ratio

of the Sun's protoplanetary disk. In a similar vein, the fraction of surviving hierarchical systems may inform the dynamical environment of the solar system after planetesimal formation.

Although we put upper limits on the non-Keplerian motion of many CCKBBs, almost none of the limits usefully constrain the system architecture, with the exception of 1999 OJ_4. For this system, the 1σ upper limit requires that the system be a compact hierarchical triple, with separation of the central binary $\lesssim 10$ primary radii. Although, since this was an upper limit, a contact binary, or simply a nearly spherical object are viable system architectures. Future observations of all CCKBBs should further decrease these upper limits, potentially allowing for scientifically useful limits to be placed on CCKBBs. These future observations will also enable more detections of non-Keplerian motion.

In addition to upper limits and the detections in the wide binaries, we also detected non-Keplerian motion in 3 ultra-wide binaries. Given the extraordinarily high values of J_2R^2, we interpret the non-Keplerian motion not as the result of the shape of a system component, but rather as the possible result of the binary being influenced by the Sun's gravity. For the widest TNBs, the difference in the Sun's gravitational acceleration between the two components can meaningfully contribute to non-Keplerian motion. The precession rate associated with the Sun's influence is:

$$\dot{\omega} = \frac{3\pi}{2}\frac{P_b}{P_h^2} \tag{5.1}$$

where P_b and P_h and the binary and heliocentric orbital periods, respectively. Using this equation, we find that 2005 EO_{304} has likely precessed about $0.5°$ since it was first observed. Since the uncertainty on the known orbit angles are $\sim 0.2°$, solar tides could certainly be detectable. This conclusion hold for both the other detections in the ultra-wides.

Another possible explanation for these unusual detections is the presence of uncharacterized systematic errors. All three of these systems have extensive datasets of ground-based observations from low-resolution observatories. It may be possible that this introduce unwanted systematics

into the fitting process. Future work should be dedicated to better understanding the orbits of these systems, and what role systematic effects might take in the orbit fitting process.

5.6   Ongoing Observations

The possible discovery of hierarchical systems with non-Keplerian orbit fitting is an exciting result. If proven correct, these systems could provide significant evidence for the SI model of planetesimal formation. As such, we have proposed–and been awarded–a program on the HST to observe four CCKBB systems. Three of the CCKBBs discussed here, 1999 RT_{214}, Altjira, and Borasisi-Pabu, are targets of this program. Currently, observations of Altjira have been completed and will inform the analysis of Nelsen et al. (in prep). The fit we used for Altjira incorporates this new data. Figure 1.1 shows the most recent observation of the Altjira system. In the next month, three more orbits will be dedicated to observing 1999 RT_{214} and Borasisi. Associated with this HST program, we plan on updating our non-Keplerian fits with the new observations.

5.7   Conclusions

The CCKB is one of the most unaltered populations of planetesimals in the solar system, making it the ideal laboratory to study the details of planetesimal formation. In particular, much recent work has shown that the SI paradigm is a very promising candidate to understand the formation of TNOs in general. In a few recent works, simulations of SI-triggered gravitational collapse have shown that hierarchical systems may be common, although only one such example is currently known.

Given the current resolution of ground and space-based telescope, resolving hierarchical systems is nearly impossible. At the distance of the CCKB ($\sim$45 AU), current telescopes are limited to $\sim$1000 km resolution, a level not adequate to detect unresolved system components. Non-Keplerian orbit fitting, however, can surpass this. The strongly nonspherical gravitational field of the hierarchical

component of one of these systems should be easily detectable in the orbit of the third, more widely separated component. In this work, we survey 16 of the 28 well-characterized CCKBBs and find that six systems have detectable non-Keplerian motion. In addition to our six detections, we also place upper limits on the existence of non-Keplerian effects in nine other systems. These upper limits are generally uninformative, but future observations may continue to lower these limits.

Using a simple shape model of a hierarchical system, we explore the possible system architectures of these six systems. The modeling reveals that three systems are consistent with hierarchical systems (1 contact hierarchical triple and 2 'regular' triples). The other three systems are consistent with having their orbits altered by the Sun's gravitational influence. Future studies should characterize the dynamics, formation, and long-term stability of all our studied systems to further understand whether these results are realistic. Likewise, observations, particularly stellar occultations, will enable confirmation (or rejection) of these results.

We interpret the existence of these three hierarchical systems as evidence for the SI model of planetesimal formation. In the future, detections like these may enable further understanding of the details of the SI model or the environment of the early solar system.

Bibliography

[1] W. Grundy, K. Noll, J. Virtanen, K. Muinonen, S. Kern, D. Stephens, J. Stansberry, H. Levison, and J. Spencer, "(42355) Typhon–Echidna: Scheduling observations for binary orbit determination," Icarus **197,** 260–268 (2008).

[2] S. B. Porter and W. M. Grundy, "KCTF evolution of trans-neptunian binaries: Connecting formation to observation," Icarus **220,** 947–957 (2012).

[3] D. L. Rabinowitz, S. D. Benecchi, W. M. Grundy, and A. J. Verbiscer, "The rotational light curve of (79360) Sila–Nunam, an eclipsing binary in the Kuiper Belt," Icarus **236,** 72–82 (2014).

[4] J. L. Ortiz *et al.*, "The size, shape, density and ring of the dwarf planet Haumea from a stellar occultation," Nature **550,** 219–223 (2017).

[5] D. L. Rabinowitz, S. D. Benecchi, W. M. Grundy, A. J. Verbiscer, and A. Thirouin, "The Complex Rotational Light Curve of (385446) Manwë–Thorondor, a Multicomponent Eclipsing System in the Kuiper Belt," The Astronomical Journal **159,** 27 (2019).

[6] K. Batygin, M. E. Brown, and W. C. Fraser, "Retention of a primordial cold classical Kuiper belt in an instability-driven model of solar system formation," The Astrophysical Journal **738,** 13 (2011).

[7] A. H. Parker and J. Kavelaars, "Destruction of binary minor planets during Neptune scattering," The Astrophysical Journal Letters **722,** L204 (2010).

[8] A. Morbidelli and D. Nesvornỳ, "Kuiper belt: formation and evolution," The trans-neptunian solar system pp. 25–59 (2020).

[9] N. Peixinho, P. Lacerda, and D. Jewitt, "Color–inclination relation of the Classical Kuiper belt objects," The Astronomical Journal **136,** 1837 (2008).

[10] W. C. Fraser and M. E. Brown, "The hubble wide field camera 3 test of surfaces in the outer solar system: the compositional classes of the Kuiper Belt," The Astrophysical Journal **749,** 33 (2012).

[11] W. C. Fraser *et al.*, "Col-OSSOS: the two types of Kuiper Belt surfaces," The Planetary Science Journal **4,** 80 (2023).

[12] K. S. Noll, W. M. Grundy, D. C. Stephens, H. F. Levison, and S. D. Kern, "Evidence for two populations of classical transneptunian objects: The strong inclination dependence of classical binaries," Icarus **194,** 758–768 (2008).

[13] W. Grundy, K. Noll, F. Nimmo, H. Roe, M. Buie, S. Porter, S. Benecchi, D. Stephens, H. Levison, and J. Stansberry, "Five new and three improved mutual orbits of transneptunian binaries," Icarus **213,** 678–692 (2011).

[14] W. Grundy, "Orbit Status of Known Binary TNOs," http://www2.lowell.edu/users/grundy/tnbs/status.html (Accessed November 14, 2023).

[15] H. F. Levison and S. A. Stern, "On the size dependence of the inclination distribution of the main Kuiper belt," The Astronomical Journal **121,** 1730 (2001).

[16] J. M. Hahn and R. Malhotra, "Neptune's migration into a stirred-up Kuiper belt: A detailed comparison of simulations to observations," The Astronomical Journal **130,** 2392 (2005).

[17] R. S. Gomes, "The origin of the Kuiper Belt high–inclination population," Icarus **161,** 404–418 (2003).

[18] R. S. Gomes, "The origin of TNO 2004 XR190 as a primordial scattered object," Icarus **215,** 661–668 (2011).

[19] D. Nesvornỳ, "Evidence for slow migration of Neptune from the inclination distribution of Kuiper belt objects," The Astronomical Journal **150,** 73 (2015).

[20] D. Nesvornỳ and D. Vokrouhlickỳ, "Binary survival in the outer solar system," Icarus **331,** 49–61 (2019).

[21] M. E. Brown *et al.*, "Satellites of the largest Kuiper belt objects," The Astrophysical Journal **639,** L43 (2006).

[22] A. H. Parker, M. W. Buie, W. M. Grundy, and K. S. Noll, "Discovery of a Makemakean moon," The Astrophysical Journal Letters **825,** L9 (2016).

[23] W. C. Fraser and M. E. Brown, "Quaoar: A rock in the Kuiper belt," The Astrophysical Journal **714,** 1547 (2010).

[24] J. Stansberry, W. Grundy, M. Mueller, S. Benecchi, G. Rieke, K. Noll, M. Buie, H. Levison, S. Porter, and H. Roe, "Physical properties of trans-neptunian binaries (120347) Salacia–Actaea and (42355) Typhon–Echidna," Icarus **219,** 676–688 (2012).

[25] M. E. Brown, "The density of mid-sized Kuiper belt object 2002 UX25 and the formation of the dwarf planets," The Astrophysical Journal Letters **778,** L34 (2013).

[26] R. S. Gomes, T. Gallardo, J. A. Fernández, and A. Brunini, "On the origin of the high-perihelion scattered disk: The role of the Kozai mechanism and mean motion resonances," Celestial Mechanics and Dynamical Astronomy **91,** 109–129 (2005).

[27] D. Nesvornỳ, "Dynamical evolution of the early Solar System," Annual Review of Astronomy and Astrophysics **56,** 137–174 (2018).

[28] M. S. Tiscareno and R. Malhotra, "The dynamics of known Centaurs," The Astronomical Journal **126,** 3122 (2003).

[29] W. Grundy, J. Stansberry, K. Noll, D. Stephens, D. Trilling, S. Kern, J. Spencer, D. Cruikshank, and H. Levison, "The orbit, mass, size, albedo, and density of (65489) Ceto/Phorcys: A tidally-evolved binary Centaur," Icarus **191,** 286–297 (2007).

[30] B. Gladman *et al.*, "The resonant trans-Neptunian populations," The Astronomical Journal **144,** 23 (2012).

[31] B. Crompvoets *et al.*, "OSSOS XXV: Large Populations and Scattering–Sticking in the Distant Trans-Neptunian Resonances," The Planetary Science Journal **3,** 113 (2022).

[32] A. N. Youdin and J. Goodman, "Streaming instabilities in protoplanetary disks," The Astrophysical Journal **620,** 459 (2005).

[33] D. Nesvornỳ, A. N. Youdin, and D. C. Richardson, "Formation of Kuiper belt binaries by gravitational collapse," The Astronomical Journal **140,** 785 (2010).

[34] D. Nesvornỳ, R. Li, J. B. Simon, A. N. Youdin, D. C. Richardson, R. Marschall, and W. M. Grundy, "Binary planetesimal formation from gravitationally collapsing pebble clouds," The Planetary Science Journal **2,** 27 (2021).

[35] A. Johansen, M.-M. M. Low, P. Lacerda, and M. Bizzarro, "Growth of asteroids, planetary embryos, and Kuiper belt objects by chondrule accretion," Science Advances **1,** e1500109 (2015).

[36] J. B. Simon, P. J. Armitage, R. Li, and A. N. Youdin, "The mass and size distribution of planetesimals formed by the streaming instability. I. The role of self-gravity," The Astrophysical Journal **822,** 55 (2016).

[37] J. Kavelaars, J.-M. Petit, B. Gladman, M. T. Bannister, M. Alexandersen, Y.-T. Chen, S. D. Gwyn, and K. Volk, "OSSOS finds an Exponential Cutoff in the Size Distribution of the Cold Classical Kuiper belt," The Astrophysical journal letters **920,** L28 (2021).

[38] J.-M. Petit, B. Gladman, J. Kavelaars, M. T. Bannister, M. Alexandersen, K. Volk, and Y.-T. Chen, "The Hot Main Kuiper Belt Size Distribution from OSSOS," The Astrophysical Journal Letters **947,** L4 (2023).

[39] J. E. Robinson, W. C. Fraser, A. Fitzsimmons, and P. Lacerda, "Investigating gravitational collapse of a pebble cloud to form transneptunian binaries," Astronomy & Astrophysics **643,** A55 (2020).

[40] W. C. Fraser *et al.*, "All planetesimals born near the Kuiper belt formed as binaries," Nature Astronomy **1,** 0088 (2017).

[41] S. Benecchi, K. Noll, W. Grundy, M. Buie, D. Stephens, and H. Levison, "The correlated colors of transneptunian binaries," Icarus **200,** 292–303 (2009).

[42] D. Nesvornỳ, R. Li, A. N. Youdin, J. B. Simon, and W. M. Grundy, "Trans-Neptunian binaries as evidence for planetesimal formation by the streaming instability," Nature Astronomy **3,** 808–812 (2019).

[43] P. Goldreich, Y. Lithwick, and R. Sari, "Formation of Kuiper-belt binaries by dynamical friction and three-body encounters," Nature **420,** 643–646 (2002).

[44] H. E. Schlichting and R. Sari, "Formation of Kuiper belt binaries," The Astrophysical Journal **673,** 1218 (2008).

[45] H. E. Schlichting and R. Sari, "The ratio of retrograde to prograde orbits: A test for Kuiper belt binary formation theories," The Astrophysical Journal **686,** 741 (2008).

[46] W. Grundy *et al.*, "Mutual orbit orientations of transneptunian binaries," Icarus **334,** 62–78 (2019).

[47] W. McKinnon *et al.*, "The solar nebula origin of (486958) Arrokoth, a primordial contact binary in the Kuiper Belt," Science **367,** eaay6620 (2020).

[48] A. Thirouin, S. S. Sheppard, and K. S. Noll, "2004 TT357: A potential contact binary in the Trans-Neptunian belt," The Astrophysical Journal **844,** 135 (2017).

[49] A. Thirouin and S. S. Sheppard, "A possible dynamically cold classical contact binary:(126719) 2002 CC249," The Astronomical Journal **154,** 241 (2017).

[50] A. Thirouin and S. S. Sheppard, "The Plutino population: An abundance of contact binaries," The Astronomical Journal **155,** 248 (2018).

[51] M. R. Showalter *et al.*, "A statistical review of light curves and the prevalence of contact binaries in the Kuiper Belt," Icarus **356,** 114098 (2021).

[52] R. Strauss *et al.*, "The DECam Ecliptic Exploration Project (DEEP) IV: Constraints on the shape distribution of bright TNOs," arXiv preprint arXiv:2309.04034 (2023).

[53] S. Stern *et al.*, "Initial results from the New Horizons exploration of 2014 MU69, a small Kuiper Belt object," Science **364,** eaaw9771 (2019).

[54] S. J. Kenyon, B. C. Bromley, D. P. O'Brien, and D. R. Davis, "Formation and collisional evolution of Kuiper belt objects," The solar system beyond Neptune 293 (2008).

[55] M. Lambrechts and A. Morbidelli, "Reconstructing the size distribution of the small body population in the Solar System," In *AAS/Division for Planetary Sciences Meeting Abstracts# 48*, **48,** 105–08 (2016).

[56] A. Johansen and M. Lambrechts, "Forming Planets via Pebble Accretion," Annual Review of Earth and Planetary Sciences **45,** 359–387 (2017).

[57] A. G. Cameron and W. R. Ward, "The origin of the Moon," In *Abstracts of the Lunar and Planetary Science Conference, volume 7, page 120,(1976)*, 7 (1976).

[58] M. E. Brown, "The largest Kuiper belt objects," The Solar System Beyond Neptune 335 (2008).

[59] A. C. Barr and M. E. Schwamb, "Interpreting the densities of the Kuiper belt's dwarf planets," Monthly Notices of the Royal Astronomical Society **460,** 1542–1548 (2016).

[60] S. Arakawa, R. Hyodo, and H. Genda, "Early formation of moons around large trans-Neptunian objects via giant impacts," Nature Astronomy **3,** 802–807 (2019).

[61] J. W. Christy and R. S. Harrington, "The satellite of Pluto," Astronomical Journal, vol. 83, Aug. 1978, p. 1005, 1007, 1008. **83,** 1005 (1978).

[62] H. Weaver, S. Stern, M. Mutchler, A. Steffl, M. Buie, W. Merline, J. Spencer, E. Young, and L. Young, "Discovery of two new satellites of Pluto," Nature **439,** 943–945 (2006).

[63] M. E. Brown and E. L. Schaller, "The mass of dwarf planet Eris," Science **316,** 1585–1585 (2007).

[64] C. Kiss, G. Marton, A. Farkas-Takács, J. Stansberry, T. Müller, J. Vinkó, Z. Balog, J.-L. Ortiz, and A. Pál, "Discovery of a satellite of the large trans-Neptunian object (225088) 2007 OR10," The Astrophysical Journal Letters **838,** L1 (2017).

[65] M. Brown, D. Ragozzine, J. Stansberry, and W. Fraser, "The size, density, and formation of the Orcus–Vanth system in the Kuiper belt," The Astronomical Journal **139,** 2700 (2010).

[66] R. M. Canup, "A giant impact origin of Pluto-Charon," Science **307,** 546–550 (2005).

[67] R. M. Canup, "On a giant impact origin of Charon, Nix, and Hydra," The Astronomical Journal **141,** 35 (2010).

[68] Z. M. Leinhardt, R. A. Marcus, and S. T. Stewart, "The formation of the collisional family around the dwarf planet Haumea," The Astrophysical Journal **714,** 1789 (2010).

[69] R. M. Canup, K. M. Kratter, and M. Neveu, "On the origin of the Pluto system," The Pluto System After New Horizons pp. 475–506 (2021).

[70] M. E. Brown, K. M. Barkume, D. Ragozzine, and E. L. Schaller, "Discovery of an Icy Collisional Family in the Kuiper Belt," , submitted (2007).

[71] D. Ragozzine and M. E. Brown, "Candidate Members and Age Estimate of the Family of Kuiper Belt Object 2003 EL61," **134,** 2160–2167 (2007).

[72] B. C. Proudfoot and D. Ragozzine, "Modeling the formation of the family of the dwarf planet Haumea," The Astronomical Journal **157,** 230 (2019).

[73] D. Ragozzine and M. E. Brown, "Orbits and Masses of the Satellites of the Dwarf Planet Haumea (2003 EL61)," **137,** 4766–4776 (2009).

[74] B. Proudfoot and D. Ragozzine, "The formation of Haumea and its family via binary merging," Nature Communications **13,** 2262 (2022).

[75] R. Malhotra, "The origin of Pluto's peculiar orbit," Nature **365,** 819–821 (1993).

[76] K. Tsiganis, R. Gomes, A. Morbidelli, and H. F. Levison, "Origin of the orbital architecture of the giant planets of the Solar System," Nature **435,** 459–461 (2005).

[77] H. F. Levison, A. Morbidelli, C. VanLaerhoven, R. Gomes, and K. Tsiganis, "Origin of the structure of the Kuiper belt during a dynamical instability in the orbits of Uranus and Neptune," Icarus **196,** 258–273 (2008).

[78] D. A. Minton and R. Malhotra, "A record of planet migration in the main asteroid belt," Nature **457,** 1109–1111 (2009).

[79] J. M. Hahn and R. Malhotra, "Orbital evolution of planets embedded in a planetesimal disk," The Astronomical Journal **117,** 3041 (1999).

[80] W. Kley and R. Nelson, "Planet-disk interaction and orbital evolution," Annual Review of Astronomy and Astrophysics **50,** 211–249 (2012).

[81] R. Malhotra, "The Origin of Pluto's Orbit: Implications for the Solar System Beyond Neptune," The Astronomical Journal **110,** 420 (1995).

[82] D. Nesvornỳ and D. Vokrouhlickỳ, "Neptune's orbital migration was grainy, not smooth," The Astrophysical Journal **825,** 94 (2016).

[83] L. E. Buchanan *et al.*, "Col-OSSOS: Probing Ice Line/Color Transitions within the Kuiper Belt's Progenitor Populations," The Planetary Science Journal **3,** 9 (2022).

[84] D. Nesvornỳ and A. Morbidelli, "Statistical study of the early solar system's instability with four, five, and six giant planets," The Astronomical Journal **144,** 117 (2012).

[85] D. Nesvornỳ, "Jumping Neptune can explain the Kuiper belt kernel," The Astronomical Journal **150,** 68 (2015).

[86] S. Tegler, W. Romanishin, and S. GJ Consolmagno, "Color patterns in the Kuiper belt: A possible primordial origin," The Astrophysical Journal **599,** L49 (2003).

[87] A. Y. Abedin *et al.*, "OSSOS. XXI. Collision Probabilities in the Edgeworth–Kuiper Belt," The Astronomical Journal **161,** 195 (2021).

[88] S. D. Benecchi, K. Noll, W. Grundy, and H. Levison, "(47171) 1999 TC36, A transneptunian triple," Icarus **207,** 978–991 (2010).

[89] C. A. Trujillo and M. E. Brown, "1999 TC_36," **7787,** 1 (2002).

[90] S. Jacobson and J. L. Margot, "Colors of TNO Binaries and Evidence for a Triple System from HST Observations," In *AAS/Division for Planetary Sciences Meeting Abstracts #39*, AAS/Division for Planetary Sciences Meeting Abstracts **39,** 52.11 (2007).

[91] Q. Konopacky, A. Ghez, T. Barman, E. Rice, J. Bailey, R. White, I. McLean, and G. Duchêne, "High-precision dynamical masses of very low mass binaries," The Astrophysical Journal **711,** 1087 (2010).

[92] S. Yelda, J. R. Lu, A. M. Ghez, W. Clarkson, J. Anderson, T. Do, and K. Matthews, "Improving galactic center astrometry by reducing the effects of geometric distortion," The Astrophysical Journal **725,** 331 (2010).

[93] M. Service *et al.*, "A new distortion solution for NIRC2 on the Keck II telescope," Publications of the Astronomical Society of the Pacific **128,** 095004 (2016).

[94] D. Foreman-Mackey, D. W. Hogg, D. Lang, and J. Goodman, "emcee: the MCMC hammer," Publications of the Astronomical Society of the Pacific **125,** 306 (2013).

[95] D. Foreman-Mackey *et al.*, "emcee v3: A Python ensemble sampling toolkit for affine-invariant MCMC," arXiv preprint arXiv:1911.07688 (2019).

[96] P. Descamps, "Dumb-bell-shaped equilibrium figures for fiducial contact-binary asteroids and EKBOs," Icarus **245,** 64–79 (2015).

[97] E. F. Guinan and D. H. Bradstreet, "Kinematic clues to the origin and evolution of low mass contact binaries," in *Formation and Evolution of Low Mass Stars* (Springer, 1988), pp. 345–375.

[98] S. Weidenschilling, "Hektor: Nature and origin of a binary asteroid," Icarus **44,** 807–809 (1980).

[99] P. Descamps, "Roche figures of doubly synchronous asteroids," Planetary and Space Science **56,** 1839–1846 (2008).

[100] R. Leiva *et al.*, "Stellar Occultation by the Resonant Trans-Neptunian Object (523764) 2014 WC510 Reveals a Close Binary TNO," The Planetary Science Journal **1,** 48 (2020).

[101] P. Thomas *et al.*, "Shape, density, and geology of the nucleus of Comet 103P/Hartley 2," Icarus **222,** 550–558 (2013).

[102] L. Jorda *et al.*, "The global shape, density and rotation of Comet 67P/Churyumov-Gerasimenko from preperihelion Rosetta/OSIRIS observations," Icarus **277,** 257–278 (2016).

[103] W. Grundy, K. Noll, M. Buie, S. Benecchi, D. Ragozzine, and H. Roe, "The mutual orbit, mass, and density of transneptunian binary Gkún'hòmdímà (229762 2007 UK126)," Icarus **334,** 30–38 (2019).

[104] A. C. Correia, "Chaotic dynamics in the (47171) Lempo triple system," Icarus **305,** 250–261 (2018).

[105] S. Toonen, A. Hamers, and S. Portegies Zwart, "The evolution of hierarchical triple star-systems," Computational Astrophysics and Cosmology **3,** 1–36 (2016).

[106] J. Barnes, L. Ludden, S. Schwartz, and S. Jacobson, "The Effects of Particle Contact Physics on the Gravitational Collapse Process," In , 54 (2022), https://baas.aas.org/pub/2022n8i506p05.

[107] S. A. Stern, *The Pluto System After New Horizons* (University of Arizona Press, 2021).

[108] H. Weaver *et al.*, "High-resolution Search for Kuiper Belt Object Binaries from New Horizons," The Planetary Science Journal **3,** 46 (2022).